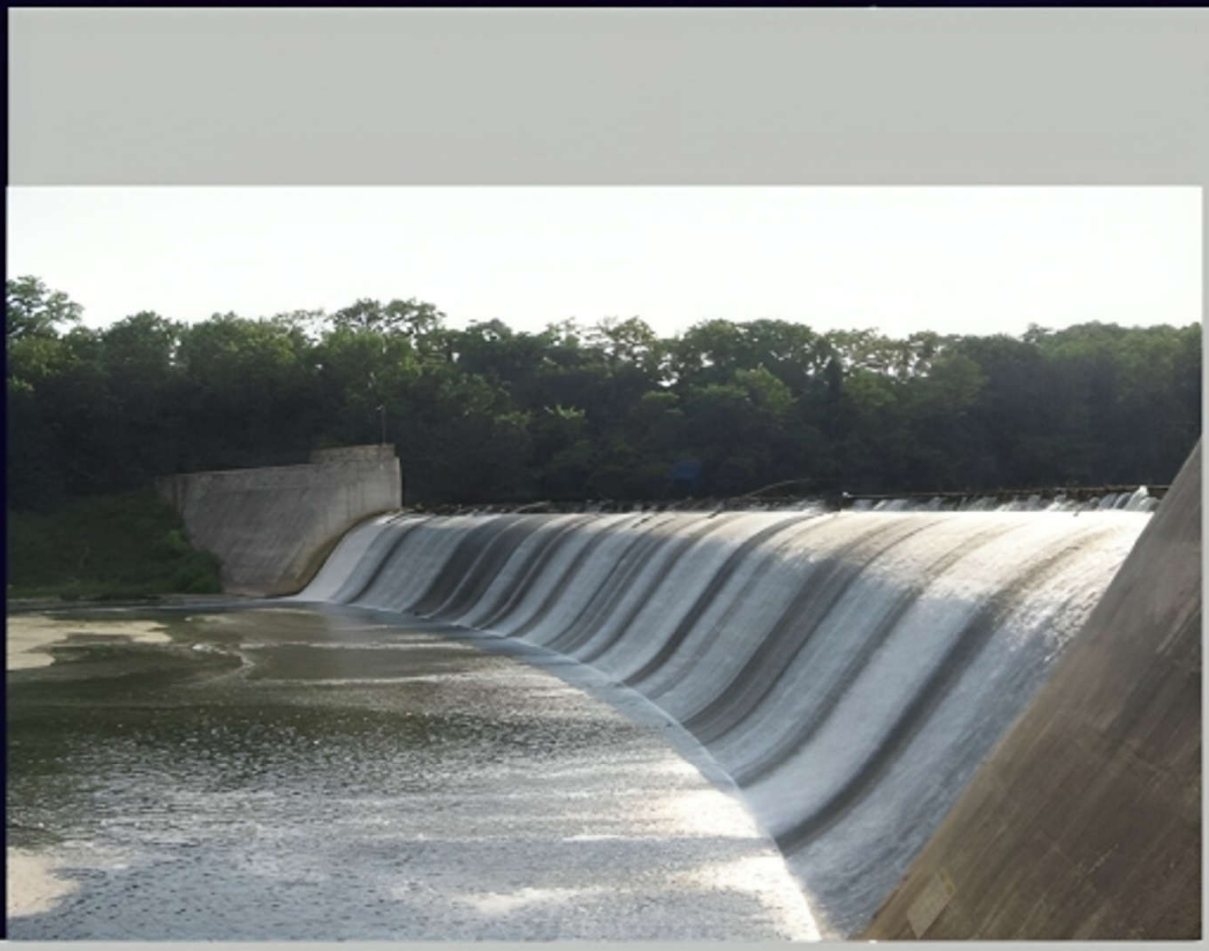
Iranian Hydraulic Association

Shahid Chamran University of Ahvaz

Journal of Hydraulic Structures

Scientific Professional Journal



July 2026
Volume 12, Issue 3

ISSN (Online): 2345-4156
https://jhs.scu.ac.ir/

Aims and Scope

Journal of Hydraulic Structures is an interdisciplinary journal which publishes high-quality peer-reviewed articles addressing the latest developments and applied methods in analysis and design, construction, maintenance, management, and operation policy of Hydraulic Structures.

The Journal aims at providing an efficient route to fast-track publication, within 10-12 weeks after manuscript submission.

The general areas covered by the Journal include:

- Advances in numerical and analytical methods applicable to hydraulic structures
- Hydro informatics and soft computing
- Hydraulic aspects of hydraulic structures
- Applied surface and subsurface hydrology and hydrometeorology
- Forecasting approaches in water resources engineering
- Economic and social aspects of hydraulic structures
- Uncertainty analysis and risk management in hydraulics and water resources engineering
- Application of Nanotechnology in hydraulic structures
- Geotechnics of hydraulic structures
- Damage detection techniques
- Technical and methodological advances in application, design/selection, production, construction materials of hydraulic structures.
- Application of Artificial Intelligence techniques in all aspects of hydraulic structures.

General Information:

Title: Journal of Hydraulic Structures

Publisher: Shahid Chamran University of Ahvaz

ISSN (Print): 2345-413X

ISSN (Online): 2345-4156

Website: jhs.scu.ac.ir

Address: Faculty of Civil Engineering and Architecture, Shahid Chamran University of Ahvaz, Ahvaz, Iran

Email: jhs@scu.ac.ir

Journal of Hydraulic Structures

Department of Civil Engineering

Shahid Chamran University of Ahvaz

Journal of

Hydraulic Structures

Shahid Chamran University of Ahvaz

Director-in-Charge: Prof. Ali Haghighi

Editor-in-Chief: Prof. Hamid R. Ghafouri

Managing Editor: Dr. Amir H. Shafiee

Contents:

01

Buckling of elliptical cylindrical shell with variable circumferential thickness under fluid lateral pressure

Davood Poorveis; Amin Khajehdezfuly; Masoud Oulapour; Hakim Tamimi

19

Uncertainty analysis for stability and cracking in a gravity dam using fuzzy set theory (Case study of Pine Flat Dam)

Zahra Ashrafi; Mehdi Komasi; Nazila Kardan

41

Investigation of the Effect of Time-Dependent Viscosity on the Penetration of Cement Grout in Rock Fractures Using a Numerical Modeling Approach

Alireza Sadooghi; Ali Aalianvari; Hamidreza Shahbazian

55

Machine Learning and Statistical Analysis of Measured Velocities by ADV of Free Surface Vortices at Intakes

Hamid Ahani; Saeed Reza Khodashenas; Hamed Sarkardeh

72

Development of an Efficient Multi-Reach Partitioning Approach with Linear Muskingum Method and Weighted Mean of Vectors Algorithm for Inverse Flood Routing

Maziar Rastegarfar; Ali Raeisi Isa-Abadi; Hamed R. Zarif Sanayei

94

Adverse Effects of Repeated Deep Drawdown and Re-impounding Cycles on the Clay Core of Earth Dams; a case study of the Karkheh Dam

Masoud Oulapour; Arash Adib; Sepideh Joulanejad

Buckling of elliptical cylindrical shell with variable circumferential thickness under fluid lateral pressure

Davood Poorveis [*,1], Amin Khajehdezfuly [1],Masoud Oulapour [1], Hakim Tamimi [1]

1. Department of Civil Engineering, Faculty of Civil Engineering and Architecture, Shahid Chamran University of Ahvaz, Ahvaz, Iran.

***Corresponding Author:**
Davood Poorveis,

Email: dpoorveis@scu.ac.ir
Received: 2025.08.10
Accepted: 2025.09.21
J. Hydraul. Struct., 2025; 12(3):1-18
DOI: 10.22055/jhs.2025.50371.1361

ABSTRACT

A review of the literature indicates that, due to the uniform curvature of circular cross-sections, the buckling load of elliptical cylindrical shells subjected to fluid lateral pressure is significantly lower than that of their circular counterparts. In many cases, fluid pressure is treated as follower pressure, meaning that the direction of the pressure exerted on an object changes in accordance with its deformation. In this study, to enhance the buckling capacity of elliptical shells, the shell thickness is varied along the circumferential direction, with greater thickness assigned to regions of lower curvature. Three thickness variation patterns (including power-law, exponential, and logarithmic) were considered in this study. A finite strip model of the shell was developed, and the buckling load was determined using the eigenvalue method. The accuracy of the developed model was validated by comparison with results obtained from finite element analysis. A comprehensive parametric study was conducted to assess the effect of geometric parameters and thickness variation patterns on the buckling of elliptical shells with circumferentially variable thickness. The results demonstrated that employing exponential, power-law, and logarithmic thickness variation can increase the buckling load by approximately 70, 60, and 20 percent, respectively. Furthermore, it was shown that for shells with a length-to-radius ratio greater than 16, the difference in buckling load under follower versus non-follower lateral pressure exceeds 30% in the most cases.

KEYWORDS

Elliptical cylindrical shell, Variable circumferential thickness, fluid pressure, follower lateral pressure, buckling.

1. Introduction

Cylindrical shells have been widely used in marine structures, the aerospace and missile industries, and pressure vessels [1]. A review of the literature indicates that assessing the buckling and stability of shells under lateral pressures and axial compressive loads is one of the most critical design criteria for these structures [2-3]. Accordingly, the buckling and stability of the shell structures have been assessed in numerous numerical and experimental previous works. Prior research has proposed various methods to enhance the buckling load of shells, including the replacement of isotropic materials with anisotropic ones (such as composite materials and Functionally Graded Materials (FGMs)) and the use of longitudinal and circumferential stiffeners [4-6].

However, these approaches often lead to a significant increase in construction costs due to the use of larger volumes of material (stiffeners) or higher-quality materials (composites and FGMs).
Alternatively, varying the shell thickness along the longitudinal or circumferential direction is another effective method for improving stability and increasing the buckling load. Although this method requires specific manufacturing technologies, it does not involve the use of special materials (such as composites or FGMs) or additional materials (like stiffeners) to enhance the shell's load-bearing capacity. A review of previous studies reveals that extensive research has focused on the effect of longitudinal thickness variations on the buckling and stability of cylindrical shells. For example, Aksogan and Sofiyev [7] employed Galerkin's method and a Ritz-type approach to investigate the dynamic buckling of elastic cylindrical shell with longitudinally varying thickness under uniform external pressure. In their study, the shell thickness was varied according to linear, parabolic, and exponential patterns. Jabbari et al., [8] applied higher-order shear deformation theory (HSDT) and a multilayer approach to develop a semi-analytical solution for the thermoelastic analysis of Functionally Graded (FG) cylindrical pressure vessels with variable longitudinal thickness subjected to non-uniform internal pressure. Three thickness profiles, linear, concave and convex, were considered in their analysis. Fan et al., [9] employed Sachenkov–Baktieva method and Fourier series expansion to study the dynamic buckling of cylindrical shells having arbitrary axisymmetric thickness variations in the longitudinal direction under time-dependent axial pressure. Ghareghani et al., [10] analyzed the bending and buckling behavior of clamped–clamped FGM cylindrical shells with longitudinally varying thickness using modified couple stress theory. Bacciocchi et al., [11] performed a free vibration analysis of plates and shells with longitudinal thickness variations using the generalized differential quadrature method.
Aghajari et al., [12] conducted experimental and numerical investigations on the buckling and post-buckling behavior of thin-walled cylindrical steel shells with variable longitudinal thickness under uniform external pressure. Chen et al., [13] examined the buckling of cylindrical shells under axial compression with small arbitrary thickness variations along the axial direction. Their study considered three types of thickness variation: stepwise, local and axisymmetric patterns. Selahi et al., [14] proposed a hybrid approach, comprising layer-wise theory, the Fourier series expansion and differential quadrature approach, for transient analysis of FG truncated conical longitudinally variable-thickness shells subjected to asymmetric dynamic pressure. Sofiyev [15] used Galerkin and Ritz methods to study the buckling of truncated conical composite thickness-variable shells under uniform pressure. Ghannad et al., [16] utilized a perturbation-based approach to investigate the buckling of a fixed-fixed thick FGM cylindrical shells with longitudinal thickness variation under internal pressure. Fazlalipour and Showkati [17] investigated the buckling behavior of variable-thickness steel cylindrical shells under combined loading. They employed a stepwise thickness variation along the longitudinal direction. Bakulin and Nedbai [18] applied the Bubnov–Galerkin method to assess the stability of a composite cylindrical variable-thickness shell subjected to axial and external pulsing pressures. Mahboubi Nasrekani and Eipakchi [19] examined the buckling of axisymmetric cylindrical shells with inhomogeneous longitudinal thickness under axial compression based on first-order shear deformation theory. Finally, Ghasemi and Hajmohammad [20] evaluated the buckling and post-buckling of variable-thickness cylindrical shells under external hydrostatic pressure.

On the other hand, comparatively few studies have explored the effect of

circumferential thickness variations on shell buckling and stability. Khalifa Ahmed [21] investigated the buckling of a variable-thickness cylindrical shell (varying thickness through circumferential direction) subjected to inhomogeneous circumferentially compressive pressures. Khalifa Ahmed [22] studied the vibration of an elastic oval cylindrical shell with varying circumferential thickness. In the study conducted by Khalifa Ahmed [22], the thickness change was such that the smaller the curvature, the greater the thickness. Gusic et al., [23] evaluated the buckling of harmonically-thickness-variable thin cylindrical shell subjected to external pressure via finite element analysis. Yang et al., [24] developed a theoretical approach for investigating the buckling of cylindrical shells having non-axisymmetric thickness variations along with longitudinal and circumferential directions under lateral pressure. Feng et al., [25] and Yang [26] investigated the buckling of cylindrical shells with arbitrary circumferential thickness variations (as an imperfection) under external pressure. Although these works provide useful insights, they remain largely descriptive and focused on specific loading or geometry cases. A clear synthesis indicates that circumferential thickness variation has not been systematically examined as a deliberate design strategy but rather as an imperfection or secondary parameter. More importantly, while some attention has been given to circular shells, the situation for elliptical shells remains understudied.

A review of the literature indicates that the buckling load of an elliptical shell is significantly lower than that of a circular shell [27]. In regions of the oval cross-section where the curvature is lower, the bending stiffness is reduced, making those areas more susceptible to local buckling under applied loads. Furthermore, no studies to date have investigated the use of circumferential thickness variation as a means of enhancing the buckling load of elliptical shells. This demonstrates a critical knowledge gap: although elliptical shells are more vulnerable to buckling, no studies to date have investigated whether circumferential thickness variation can be used to counteract this weakness and enhance their load-bearing capacity. In this study, while the total material volume of the shell structure is kept constant, the shell thickness at each point along the oval cross-section is defined as a function of the curvature. Specifically, points with greater curvature are assigned smaller thickness values. Accordingly, three Thickness Variation Patterns (TVPs) including power, logarithmic, and exponential, were considered in the circumferential direction. An elliptical cylindrical shell model with variable thickness was developed using the finite strip method. The model's results were validated by comparing them with data from the literature. A parametric study was then conducted to evaluate the effect of circumferential thickness variation on the buckling lateral pressure of the elliptical shell.

2. Development of model

Figure 1 shows the oval cross section with variable thickness in circumferential direction simulated in this study. The maximum and minimum diameters of the oval section are a and b, respectively. According to figure 1, as the curvature decreases, the thickness of the shell increases. So, the minimum thickness (hmin) is considered at the highest curvature of the oval section. Z-Y and n-θ stand for vertical-horizontal and normal-tangential coordinate systems, respectively. As shown in figure 1, the angle and radius of curvature of an arbitrary point located at the mid-plane of the ellipse are θ and $R(\theta)$, respectively. The thickness of the ellipse at this point is considered as $h(\theta)$. Equation 1 provides the relationship between the radius of curvature and other geometric variables of the elliptical cross-section (including a, b and θ) [28].

$$R(\theta) = \frac{a^2 b^2}{(a^2 \cos^2(\theta) + b^2 \sin^2(\theta))^{3/2}} \quad (1)$$

In equation 1, b and a stand for the minimum and maximum radii of the oval section (Figure 1). Moreover, θ and $R(\theta)$ were defined earlier. Figure 2 shows a 3D view of a variable-thickness elliptical cylindrical shell subjected to fluid lateral pressure. The shell's cross-section is depicted in Figure 1. In this study, the shell was discretized into several finite strip elements. To achieve this, a strip element with variable thickness in the transverse direction was developed, as illustrated in Figure 3. Additionally, Figure 4 shows the placement of the curved strip element on the positive quarter of the elliptical cross-section.

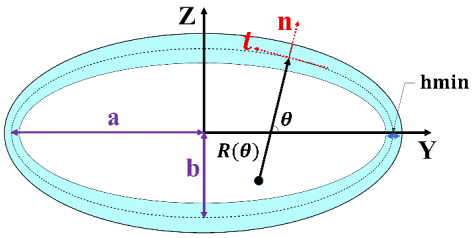


Figure 1. Oval cross section with variable thickness in circumferential direction

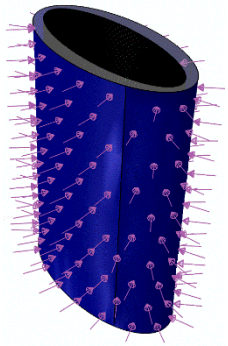


Figure 2. Variable-thickness elliptical cylindrical shell under fluid lateral pressure

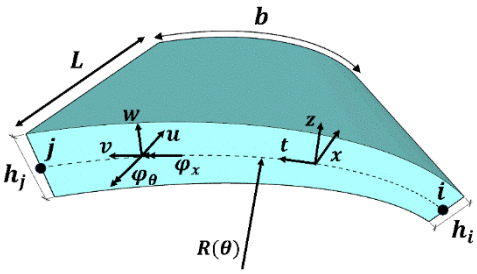


Figure 3. 3D view of finite strip element developed in this study

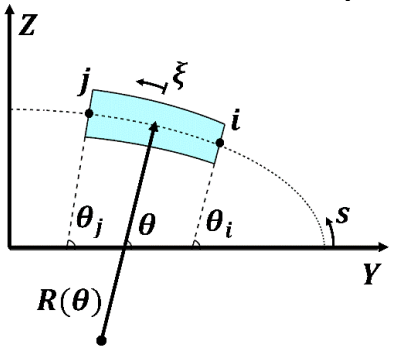


Figure 4. Curved strip element position on positive quarter of ellipse cross-section

Figure 3 shows 3D view of a strip element with length of L, width of b, variable thickness ($h(\theta)$) and variable radius of curvature ($R(\theta)$). As presented in figures 3, two nodes (i and j) were considered to develop Lagrangian shape functions in the transverse direction. The thickness of the element in nodes i and j is h_i and h_j , respectively. Figure 4 shows a two-noded strip element with variable thickness along with the global and local coordinates (s, ξ). As illustrated in figure 4, local coordinate of ξ is zero at the middle of the strip width and changes from -1 to +1. The radius of curvature at i and j nodes of the strip element were calculated based on θ_i and θ_i and via Equation 1. Also, the shape functions in elliptical cross-section are extracted using equation 2 [29].

$$\begin{aligned} \mathrm{N}_1(\xi) &= \frac{1-\xi}{2} \\ \mathrm{N}_2(\xi) &= \frac{1+\xi}{2} \end{aligned} \tag{2}$$

In equation 2, $\mathrm{N}_1(\xi)$ and $\mathrm{N}_2(\xi)$ are shape functions of nodes i and j, respectively, at ξ *coordinate*. Accordingly, the value of each variable at coordinate of ξ (f(ξ)) is calculated using equation 3 [29].

$$\mathrm{f}(\xi) = \mathrm{N}_1(\xi)\mathrm{f_i} + \mathrm{N}_2(\xi)\mathrm{f}_j \tag{3}$$

In equation 3, f_i and f_j are the value of the variable at nodes i and j, respectively. Accordingly, equation 4 was used to calculate the arc length of a point in ξ local coordinate ($s(\xi)$) based on arc lengths of points i and j (s_i and s_j) [29]. Following sub-sections present the details of the finite strip model developed in this study.

$$s(\xi) = s_i N_1(\xi) + s_j N_2(\xi) \quad (4)$$

2.1. Thickness variation in strip element

In this study, the change in shell thickness in the circumferential direction is considered in such a way that the volume of material used in the shell does not change compared to a shell with a constant thickness. This hypothesis has become the basis for considering logical patterns for thickness variation, such that in areas with lower curvature, the shell thickness is increased in order to reduce stress, and in contrast, in areas with higher curvature, the shell thickness is decreased to balance the bending stiffness across the entire cross section. In this study, three distinct patterns were considered for variation of the thickness along with the circumferential direction (including power, exponential and logarithmic). It is important to note that the power value of power TVP includes various thickness distributions, including linear and quadratic.

2.1.1. Power thickness variation

Equation 5 shows the power variation in thickness of strip element based on the change in the curvature.

$$\Delta h = \alpha \left(\frac{R(\theta)}{R_{min}}\right)^n + \beta \quad (5)$$

In Equation 5, Δh represents the difference between the thickness at a point with curvature radius $R(\theta)$ and the minimum thickness of the elliptical section (which is hmin as shown in Figure 1). Moreover, R_{min} denotes the curvature radius of the point with the minimum thickness (hmin) and n is the power value and can take positive real values. Accordingly, the coefficients α and β were determined such that Δh=0 when $R(\theta) = R_{min}$. The coefficient α was also calculated under the assumption that the volume of the cylinder material remains constant. In this study, the perimeter of the ellipse is considered constant. Due to the symmetry of the elliptical shell with respect to both the major and minor axes, calculations were performed for only one-fourth of the elliptical cross-section. Accordingly, the thickness at the point with curvature radius of $R(\theta)$ is expressed as follows:

$$h(\theta) = hmin + \alpha \left[\left(\frac{R(\theta)}{R_{min}}\right)^n - 1\right] \quad (6)$$

In equation 6, $h(\theta)$ is thickness at curvature angle of θ. By assuming an equivalent circular section with constant thickness h_0 and equivalent radius R_0, the following constraint is obtained:

$$\int_0^{\frac{\pi}{2}} h(\theta) R(\theta)\, d\theta = \frac{\pi R_0 h_0}{2} \quad (7)$$

In this research, the values of R_0 and h_0 are 100 and 1, respectively. Equation 7 is expanded as follows:

$$-\alpha \int_0^{\frac{\pi}{2}} R(\theta)\, d\theta + \alpha \left(\frac{1}{R_{min}}\right)^n \times \int_0^{\frac{\pi}{2}} R_{(\theta)}^{n+1}\, d\theta + \frac{\pi R_0 hmin}{2} = \frac{\pi R_0 h_0}{2} \quad (8)$$

Accordingly, α is obtained as A_1/A_2, where A_1 and A_2 are obtained using equation 9.

$$A_1 = \frac{\pi R_0}{2}(h_0 - hmin)$$
$$A_2 = \left(\frac{1}{R_{min}}\right)^n \times \int_0^{\frac{\pi}{2}} R(\theta)^{n+1}\, d\theta - \frac{\pi R_0}{2} \quad (9)$$

2.1.2. Exponential thickness variation

Equation 10 presents the variation of shell thickness through an exponential pattern.

$$\Delta h = \alpha e^{\left(\frac{R(\theta)-R_{min}}{R_{min}}\right)} + \beta \tag{10}$$

Accordingly, the thickness at any arbitrary point on the circumference of the ellipse with the radius of curvature of $R(\theta)$ is obtained using Equation 11.

$$h(\theta) = hmin + \alpha\left[e^{\left(\frac{R(\theta)-R_{min}}{R_{min}}\right)} - 1\right] \tag{11}$$

Considering the assumption that the cross-sectional area of the ellipse is constant, the coefficient α is obtained as B_1/B_2 where B_1 and B_2 are obtained from Equation 12.

$$\begin{aligned} B_1 &= \frac{\pi R_0 h_0}{2} - \frac{\pi R_0 hmin}{2} = \frac{\pi R_0}{2}(h_0 - hmin) \\ B_2 &= \int_0^{\frac{\pi}{2}} R(\theta)\left[e^{\left(\frac{R(\theta)-R_{min}}{R_{min}}\right)} - 1\right] d\theta \end{aligned} \tag{12}$$

2.1.3. Logarithmic thickness variation

In the case of logarithmic thickness variation, the amount of thickness increase is considered as a logarithmic distribution of the radius of curvature of the ellipse (Equation 13).

$$\Delta h = \alpha\, log\left(\frac{R(\theta)}{R_{min}}\right) + \beta \tag{13}$$

As in the previous cases, the thickness of the ellipse at any arbitrary point is obtained using Equation 14.

$$h(\theta) = hmin + \alpha\, log\left(\frac{R(\theta)}{R_{min}}\right) \tag{14}$$

Accordingly, α is obtained as C_1/C_2 where C_1 and C_2 are obtained from Equation 15.

$$\begin{aligned} C_1 &= \frac{\pi R_0 h_0}{2} - \frac{\pi R_0 hmin}{2} \\ &= \frac{\pi R_0}{2}(h_0 - hmin) \\ C_2 &= \int_0^{\frac{\pi}{2}} R(\theta)\, log\left(\frac{R(\theta)}{R_{min}}\right) d\theta \end{aligned} \tag{15}$$

2.2. Strip element formulation

In this research, five independent degrees of freedom, including three displacements (u, v and w) and two rotations (φ_θ and φ_x), were considered at each point of the shell (Figure 3). u is axial displacement in the longitudinal direction of the cylinder, v stands for displacement along the circumference of the cylinder, w represents displacement in the radial direction of the cylinder, φ_θ is rotation about the axial axis of the cylinder and φ_x represents rotation about the circumferential direction of the cylinder. Fourier series expansions and harmonic functions were employed to approximate the displacement functions in the longitudinal and transverse directions, respectively (Equation 16) [29-30].

$$\begin{aligned} u &= \sum_{p=1}^{M}\sum_{q=1}^{2} u_{pq}\,.\,cos(a_p x)\,.\,N_q(\eta) \\ &\quad + \sum_{q=1}^{2} u_{0q}\,.\,N_q(\eta).\left(\frac{1}{2} - \frac{x}{L}\right) \\ v &= \sum_{p=1}^{M}\sum_{q=1}^{2} v_{pq}.sin(\alpha_p.x).N_q(\eta) \\ w &= \sum_{p=1}^{M}\sum_{q=1}^{2} w_{pq}.sin(\alpha_p.x).N_q(\eta) \\ \varphi_x &= \sum_{p=1}^{M}\sum_{q=1}^{2} \varphi_{x_{pq}}.cos(\alpha_p.x).N_q(\eta) \\ \varphi_\theta &= \sum_{p=1}^{M}\sum_{q=1}^{2} \varphi_{\theta_{pq}}.sin(\alpha_p.x).N_q(\eta) \end{aligned} \tag{16}$$

In Equation 16, p and q stand for the harmonic number in the longitudinal direction and node number in the circumferential direction, respectively. In addition, M is the total number of harmonics and α_p is $p\pi/L$. It should be noted that the additional term considered for the u-component, relative to the other

displacements and rotations, is included in the pre-buckling analysis to accelerate convergence, but it is disregarded in the eigenvalue buckling analysis. It should be noted that, the displacement at any arbitrary point on the shell ($\overline{u}$, $\overline{v}$ and $\overline{w}$) was calculated using the first-order shear deformation theory, as expressed in Equation 17. All parameters used in Equation 17 were defined earlier [29-30].

$$\begin{aligned}\overline{u}(x.\theta.z) &= u(x.\theta) + z,\varphi_x(x.\theta)\\ \overline{v}(x.\theta.z) &= v(x.\theta) + z,\varphi_\theta(x.\theta)\\ \overline{w}(x.\theta.z) &= w(x.\theta)\end{aligned} \quad (17)$$

It should be noted that a closed, simply supported cylindrical shell is considered in this study. Accordingly, the equations corresponding to different harmonics are decoupled, thereby reducing the number of degrees of freedom in each step of the analysis. In contrast, for other boundary conditions such as fixed or free edges, the harmonics become coupled, which increases the number of degrees of freedom and consequently raises the computational cost of the model. The generalized strain and stress vectors ($\{\varepsilon\}$ and $\{\sigma\}$) are provided in Equations 18 and 19, respectively.

$$\begin{aligned}\{\varepsilon\}^T &= \{\varepsilon \quad k \quad \gamma\}\\ &= \{\varepsilon_{xx} \quad \varepsilon_{\theta\theta}\ \gamma_{x\theta}\ k_{xx} \quad k_{\theta\theta} \quad k_{x\theta} \quad \gamma_{xz} \quad \gamma_{\theta z}\}\end{aligned} \quad (18)$$

$$\begin{aligned}\{\sigma\}^T &= \{N \quad M \quad Q\}\\ &= \{N_{xx}\ N_{\theta\theta}\ N_{x\theta}\ M_{xx}\ M_{\theta\theta}\ M_{x\theta}\ Q_{xz}\ Q_{\theta z}\}\end{aligned} \quad (19)$$

In Equation 18, ε_{xx} and $\varepsilon_{\theta\theta}$ stand for the normal strains of the middle plane in the x and θ directions, respectively; $\gamma_{x\theta}$ is the shear strain in the $x\theta$ plane, k_{xx} and $k_{\theta\theta}$ are the bending curvatures about the x and θ directions, respectively; $k_{x\theta}$ represents the torsional curvature in the $x\theta$ plane, γ_{xz} and $\gamma_{\theta z}$ denote the shear strains in the xz and $x\theta$ planes in the shell thickness direction, respectively. In Equation 19, N_{xx}, $N_{\theta\theta}$ and $N_{x\theta}$ stand for the normal membrane force per unit length in the x direction, the normal membrane force per unit length in the θ direction, and the in-plane shear force in the xθ plane, respectively. In addition, M_{xx} and $M_{\theta\theta}$ represent the bending moment per unit length about the θ and x directions, respectively; $M_{x\theta}$ is the torsional moment per unit length in the xθ plane. Furthermore, Q_{xz} and $Q_{\theta z}$ stand for the out-of-plane shear forces per unit length in the xz and θz planes, respectively. The linear and nonlinear components of the strain vector were derived based on Sanders' theory and are available in the previous studies [31-32]. Sanders' theory provides sufficient accuracy for moderate thickness while accounting for transverse shear effects, which are neglected in classical thin shell theory. This makes it suitable for this study where shell thickness varies circumferentially and may reach moderate values in some regions. The generalized stress-strain relationship considered in this study is presented in Equation 20 [30].

$$\begin{Bmatrix} N \\ M \\ Q \end{Bmatrix} = \begin{bmatrix} A_{ij} & B_{ij} & 0 \\ B_{ij} & D_{ij} & 0 \\ 0 & 0 & H_{ij} \end{bmatrix} \begin{Bmatrix} \varepsilon \\ k \\ \gamma \end{Bmatrix} \quad (20)$$

In Equation 20, A_{ij} , , B_{ij} , D_{ij} and H_{ij} stand for the (i, j) components of the axial rigidity, axial-flexural coupling rigidity, flexural rigidity, and shear rigidity matrices, respectively. The mentioned rigidity matrices are determined using Equation 21 [30].

$$\begin{aligned}&\left(A_{ij}.B_{ij}.D_{ij}\right) = \int_h (1.z.z^2)\bar{Q}_{ij}(z)dz \quad i.j = 1.2.6\\ &H_{ij} = K_s \int_h \bar{Q}_{ij}(z)dz \quad i.j = 4.5\end{aligned} \quad (21)$$

In Equation 21, K_s represents the shear correction factor and was considered as $5/6$. Moreover, $\bar{Q}_{ij}(z)$ is ith and jth component of reduced stiffness matrix and is obtained using Equation 22 [30].

$$\begin{aligned}\bar{Q}_{11} &= \bar{Q}_{22} = \frac{E}{1-\nu^2}\\ \bar{Q}_{12} &= \bar{Q}_{21} = \frac{\nu E}{1-\nu^2}\\ \bar{Q}_{44} &= \bar{Q}_{55} = \bar{Q}_{66} = \frac{E}{2(1+\nu)}\end{aligned} \quad (22)$$

In Equation 22, E and v represent the modulus of elasticity and Poisson's ratio of the material, respectively. As isotropic material is utilized in this study, B_{ij} and H_{45} components are zero. The internal virtual work done by linear strains and their corresponding stresses ($\delta W_{internal}^{linear}$) was written to determine the elastic stiffness matrix of the strip element (Equation 23). Accordingly, the elastic stiffness matrix for j-th strip element and the shell ($[K_E]_j$ and $[K_E]$) were obtained from Equation 24 [29].

$$\begin{aligned}\delta W_{internal}^{linear} = \int_x \int_\theta (&N_{xx}\delta\varepsilon_{xx} + N_{\theta\theta}\delta\varepsilon_{\theta\theta} \\ &+ N_{x\theta}\delta\gamma_{x\theta} + M_{xx}\delta k_{xx} \\ &+ M_{\theta\theta}\delta k_{\theta\theta} \\ &+ M_{x\theta}\delta k_{x\theta} + Q_{xz}\delta\gamma_{xz} \\ &+ Q_{\theta z}\delta\gamma_{\theta z})R(\theta)d\theta dx\end{aligned} \quad (23)$$

$$\begin{aligned}\delta W_{internal}^{linear} &= \sum_{j=1}^{nstrip} (\delta\Delta_j)^T [K_E]_j \Delta_j \\ &= (\delta\Delta)^T K_E \Delta\end{aligned} \quad (24)$$

In Equation 24, Δ_j and Δ are displacement/rotation vectors of j-th strip element and shell, respectively. Moreover, $\delta\Delta_j$ and $\delta\Delta$ represent virtual displacement/rotation vectors of j-th element and shell, respectively. Moreover, $nstrip$ is total number of strip elements. The internal virtual work done by initial membrane forces and the nonlinear terms of membrane strains ($\delta W_{internal}^{nonlinear}$) was written to determine the geometric stiffness matrix of the strip element (Equation 25) [29, 31-32].

$$\begin{aligned}&\delta W_{internal}^{nonlinear} \\ &= \int_x \int_\theta (N_{xx}^0 \delta\varepsilon_{xx}^{nl} + N_{\theta\theta}^0 \delta\varepsilon_{\theta\theta}^{nl} \\ &+ N_{x\theta}^0 \delta\gamma_{x\theta}^{nl})R(\theta)d\theta dx\end{aligned} \quad (25)$$

The initial membrane forces (N_{xx}^0, $N_{\theta\theta}^0$, $N_{x\theta}^0$) were obtained from a pre-buckling analysis (Khayat et al., 2017). Accordingly, the geometric stiffness matrix for j-th strip element and the shell ($[K_G]_j$ and $[K_G]$) were obtained from Equation 26 [29, 31-32].

$$\begin{aligned}\delta W_{internal}^{nonlinear} &= \sum_{j=1}^{nstrip} (\delta\Delta_j)^T [K_G]_j \Delta_j \\ &= (\delta\Delta)^T K_G \Delta\end{aligned} \quad (26)$$

On other hand, the external virtual work done by the follower lateral pressure ($\delta W_{external}^{\bar{q}^l}$) was written to determine the load vector and the part of the stiffness matrix dependent on the follower lateral pressure (Equation 27) [29, 31-32].

$$\begin{aligned}\delta W_{external}^{\bar{q}^l} &= \delta W_{external}^{\bar{q}} + \\ &\delta W_{sym.}^{domain} + \delta W_{skew}^{load} + \delta W_{skew}^{bound}\end{aligned} \quad (27)$$

In Equation 27, $\bar{q}^l$ is follower lateral pressure and $\bar{q}$ represents non-follower part of the lateral pressure. As presented in Equation 27, $\delta W_{external}^{\bar{q}^l}$ involves four parts including $\delta W_{external}^{\bar{q}}$, $\delta W_{sym.}^{domain}$, δW_{skew}^{load} and δW_{skew}^{bound} which are obtained from Equations 28 to 31, respectively [29, 31-32]. The force vector of the model is obtained using the external work done by non-follower part of the lateral pressure ($\delta W_{external}^{\bar{q}}$). On other hand, $\delta W_{sym.}^{domain}$, δW_{skew}^{load} and δW_{skew}^{bound} depend on follower part of the lateral pressure [29, 31-32].

$$\delta W_{external}^{\bar{q}} = -\int_0^{2\pi}\int_0^{L} \bar{q}(x.\theta)\,\delta w\, R(\theta) dx\, d\theta \quad (28)$$

$$\delta W_{sym,}^{domain} = -\delta \iint_A \frac{1}{2}\bar{q}^l(x.\theta)(v^2 + w^2 + w\,R(\theta)\frac{\partial u}{\partial x} - R(\theta)\,u\frac{\partial w}{\partial x} + w\frac{\partial v}{\partial \theta} - v\frac{\partial w}{\partial \theta})\, dx\, d\theta \quad (29)$$

$$\delta W_{skew}^{load} = -\iint_A (-w\delta v\frac{\partial \bar{q}^l}{\partial \theta} + v\,\delta w\frac{\partial \bar{q}^l}{\partial \theta} - R(\theta)w\,\delta u\frac{\partial \bar{q}^l}{\partial x} + R(\theta)\,u\,\delta w\,\frac{\partial \bar{q}^l}{\partial x})\, dx\, d\theta \quad (30)$$

$$\delta W_{skew}^{bound} = \frac{1}{2}\int_0^{2\pi}(R(\theta)w\,\delta u\,\bar{q}^l - R(\theta)u\,\delta w\,\bar{q}^l)\Big|_0^L d\theta + \frac{1}{2}\int_0^{L}(w\,\delta v\,\bar{q}^l - v\,\delta w\bar{q}^l)\Big|_0^{2\pi} dx \quad (31)$$

Generally, the pressure exerted by the water on a structure wall varies in the circumferential and longitudinal directions. So, in Equations 27 and 29, δW_{skew}^{load} depends on variation of follower lateral pressure in θ and x directions. As in this study, $\bar{q}^l$ was constant along with θ and x directions, δW_{skew}^{load} is zero. Moreover, δW_{skew}^{bound} in Equations 27 and 31 depend on boundary conditions of the shell and as a closed simply supported cylindrical shell was considered in this study, δW_{skew}^{bound} is zero [29, 31-32]. In this study, $\delta W_{sym.}^{domain}$ is the only non-zero term of external virtual work done by follower lateral pressure and has a quadratic form. Accordingly, the load stiffness matrices of j-strip element and shell ($[K_P]_j$ and $[K_P]$) were obtained using $\delta W_{sym.}^{domain}$ (Equation 32) [29, 31-32].

$$\delta W_{sym.}^{domain} = \sum_{j=1}^{nstrip}(\delta\Delta_j)^T[K_P]_j\Delta_j = (\delta\Delta)^T K_P\Delta \quad (32)$$

Equation 33 were utilized to calculated the mode shapes (ϕ) of the shell based on the eigenvalue problem [29, 31-32].

$$(K_E - \lambda(K_G + K_P))\phi = 0 \quad (33)$$

In Equation 33, K_E, K_G and K_p are elastic, geometrical and follower pressure-dependent of stiffness matrices of the shell, respectively. It should be noted that K_p stiffness matrix in the follower and non-follower pressure states is non-zero and zero, respectively. It should be noted that the Gauss numerical integration method (Gaussian quadrature) was adopted in this research.

3. Model convergence and validation

In this section, the convergence as well as the accuracy of the results obtained from the model developed in this research are examined.

3.1. Model convergence

An isotropic elliptical cylindrical shell with b/a ratios of 0.5, 0.7, and 0.9 was considered to evaluate the convergence of the model developed in this study. The shell has a variable thickness following an exponential pattern and is subjected to a follower lateral pressure. The Young's modulus of the shell material is 2000 kN/mm², and the Poisson's ratio is 0.3. Moreover, hmin was considered as 0.48. Figure 5 illustrates the convergence of the model results as the total number of nodes increases from 48 to 120. The relative error was calculated based on the buckling load obtained for the 120-node case. As shown in Figure 5, increasing the number of nodes reduces the difference between results to below 0.1%. Moreover, the figure indicates that as the b/a ratio decreases, the model requires a larger number of nodes to achieve

good convergence. Consequently, for all b/a values, the model with 120 nodes provides sufficiently converged results.

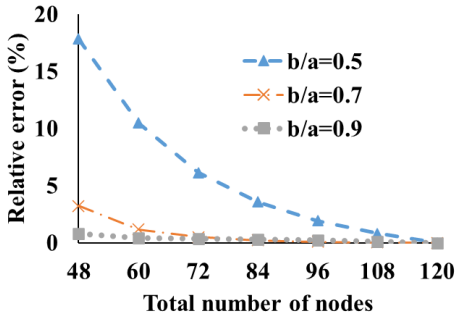
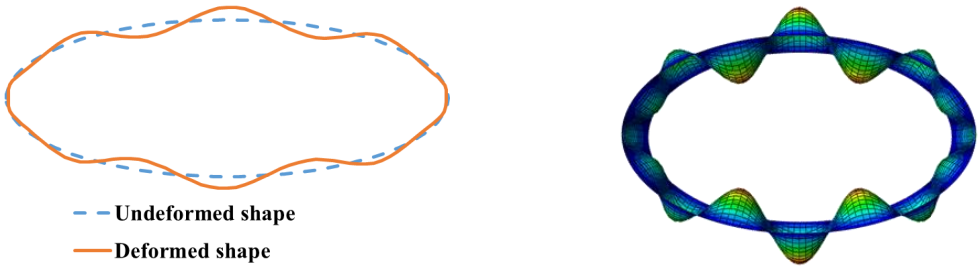


Figure 5. Convergence of model developed in this study

3.2. Model validation

A comparison was made between results obtained from the model developed in this study and those of finite element model implemented in ABAQUS to validate the developed model. In this regard, an elliptical cylindrical shell with a power-law thickness variation (power = 0.5), subjected to follower lateral pressure and made of isotropic material (as described in the previous sub-section), was analyzed using both the developed model and the well-known finite element software ABAQUS. The ratio of cylinder length to equivalent radius (L/R_0), minimum thickness (hmin), and b/a were set to 1, 0.48, and 0.5, respectively. The buckling loads obtained from the developed model and ABAQUS were 0.012587 and 0.012027, respectively, indicating a small difference of 4.6%. Furthermore, as shown in Figure 6, the buckling mode shapes obtained from the developed model closely match those predicted by ABAQUS. This indicates the acceptable accuracy of the results obtained from the numerical model developed in this study.



(a) (b)

Figure 6. Mode shapes of shell obtained from (a) model developed in this study (b) ABAQUS

4. Parametric study

A parametric study was conducted to investigate the effects of various parameters on the buckling load of the shell, including the TVP, minimum thickness (hmin), shell geometric characteristics, properties of the functionally graded material, and loading type (follower and non-follower lateral pressures). Based on this study, the ratio of shell length to equivalent radius (L/R_0) was considered as 0.5, 1, 2, 4, 8, 16, and 32. The shell thickness was varied between 0.35 and 1, and the ratio of the minimum to maximum diameters of the oval section (b/a) ranged from 0.4 to 1. It

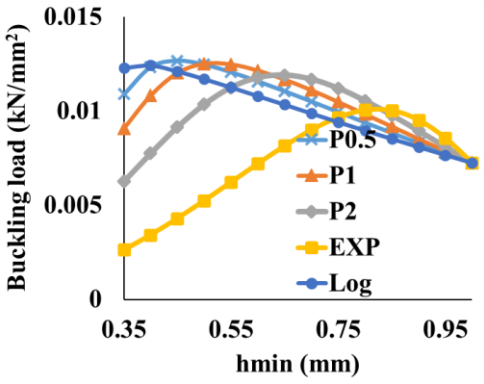
should be noted that logarithmic, exponential, and power variation-thickness patterns are represented by the parameters "Log", "EXP", and "P", respectively. Also, for the power thickness-variation pattern, the power value appears in front of the "P". In the analyses, the shell structure was discretized into 120 curved two-node strip elements, all of which were identical. The results of the parametric study are presented in the following sub-sections.

4.1. Minimum thickness

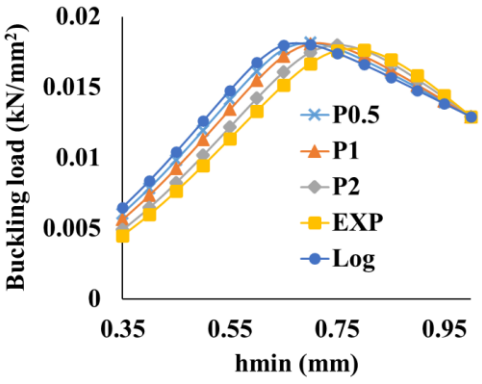
The effect of minimum thickness (hmin) on the buckling load of the shell under follower lateral pressure, considering different TVPs, was investigated. In this section, hmin was varied between 0.35 and 1 mm and L/R_0 is assumed to be equal to 1. Figure 7 shows the effect of variation of minimum thickness (hmin) on the buckling load of a variable- thickness shell with different values of b/a under follower and non-follower lateral pressures. The value of b/a in figures 7(a) to 7(c) is 0.5, 0.7, and 0.9, respectively.

As shown in Figure 7, in all cases, increasing hmin from 0.35 to a certain value (hereinafter referred to as the optimum value) leads to a maximum buckling load. When hmin exceeds this optimum value, the buckling load of the shell decreases in all cases. According to figure 7, the optimum value of hmin depends on two factors: b/a ratio and the TVP. Based on the results shown in Figures 7, as the b/a ratio increases (from 0.5 to 0.9), the influence of TVP on both the optimum value of hmin and the buckling load of the shell decreases significantly. For example, in the case of an ellipse with a b/a ratio of 0.9 (Figure 7(c)), there is only a slight difference between the results obtained for all TVPs, whereas for a b/a ratio of 0.5 (Figure 7(a)), this difference is quite substantial. Figure 7 indicates that the power-law TVP with a power of 0.5 yields the highest buckling load across all b/a ratios. This is followed by the power-law TVP with a power of 1 and the logarithmic TVP, which also produce relatively high buckling loads. It should be noted that the optimum hmin varies depending on the selected TVP and b/a ratio.

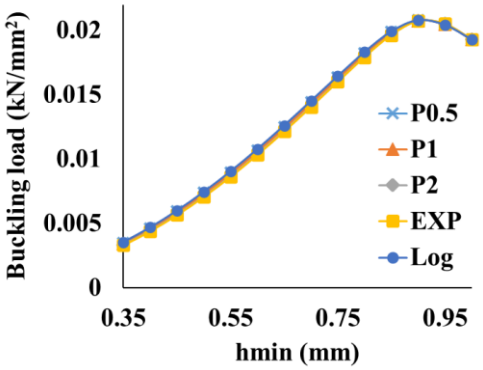
To gain a deeper understanding of how minimum thickness variation influences the buckling behavior of a variable-thickness shell under follower lateral pressure, the first mode shape of an elliptical shell with a b/a ratio of 0.5, a power-law TVP (with a power of 1), and different minimum thickness values is shown in Figure 8. As illustrated in this figure, when hmin reaches its optimum value (i.e., 0.51), general buckling occurs, meaning the entire shell wall deforms during buckling. In contrast, for other minimum thickness values, only regions of the shell wall with lower bending stiffness (i.e., those with a larger radius of curvature) undergo local deformation during buckling.



(a)



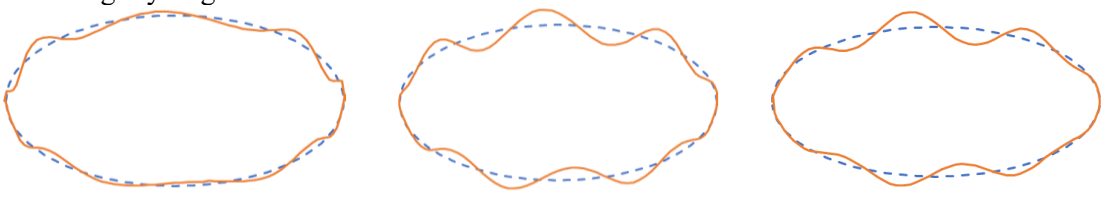
(b)



(c)

Figure 7. Effect of variation of minimum thickness on buckling load of thickness-variable shell with different values of b/a under follower lateral pressure (a) b/a=0.5 (b) b/a=0.7, (c) b/a=0.9

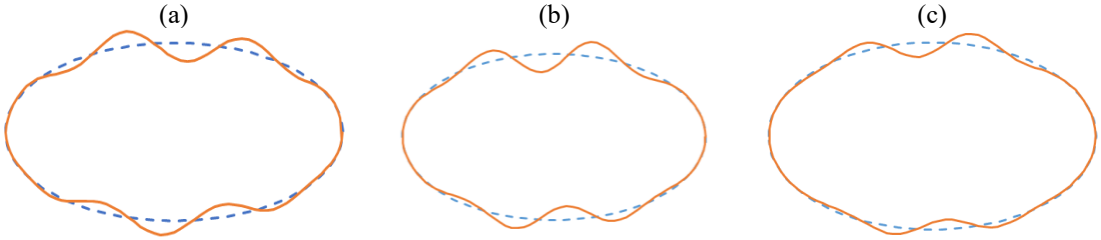
This indicates that when hmin reaches its optimum value, the continuous thickness variation around the elliptical shell circumference results in a more uniform distribution of bending stiffness. As a result, the entire elliptical shell wall buckles simultaneously (occurrence of general buckling). However, in an elliptical shell with constant thickness, the bending stiffness is lower in regions with a larger radius of curvature, leading to localized buckling in those areas. Although the buckling loads obtained from the Power (P), EXP, and Log TVPs are close, the power one consistently yields slightly higher critical loads. This improvement can be attributed to the smoother circumferential thickness distribution in the power pattern, which provides better alignment between thickness variation and curvature changes. As a result, the shell's bending stiffness is enhanced and localized stress concentrations are reduced in the power case. These observations indicate that an optimum power exponent may exist that maximizes the buckling load for a given shell configuration. Exploring this optimum value and its influence on shell stability represents a promising direction for future research.



Buckling load = 0.0113 kN/mm²
(a)

Buckling load = 0. 0126 kN/mm²
(b)

Buckling load = 0. 0118 kN/mm²
(c)



Buckling load = 0. 0108 kN/mm²
(d)

Buckling load = 0. 0093 kN/mm²
(e)

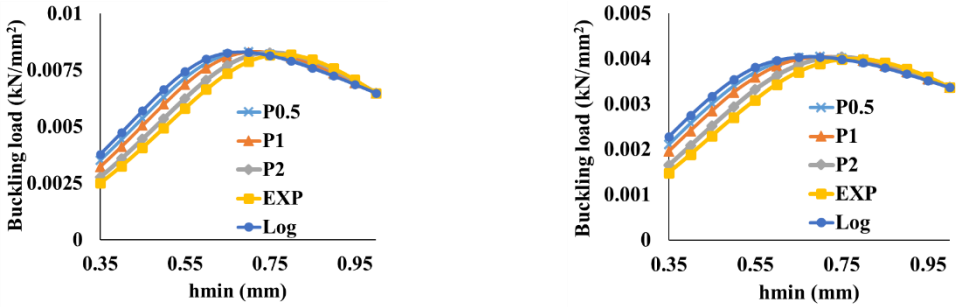
Buckling load = 0. 0081 kN/mm²
(f)

Figure 8. Effect of hmin on first mode shape of elliptical shell with b/a of 0.5 and power-law TVP (a) hmin = 0.4, (b) hmin = 0.51, (c) hmin = 0.6, (d) hmin = 0.7, (e) hmin = 0.8, (f) hmin = 0.9

It should be noted that eigenvalue buckling analyses were performed for different harmonic numbers to calculate the longitudinal half-wave associated with buckling under lateral pressure. The harmonic number corresponding to the minimum buckling pressure was designated as the longitudinal buckling mode. In this study, all longitudinal buckling modes for different geometries and material properties consisted of a single half-wave.

4.2. Ratio of shell length to equivalent radius (L/R_0)

Figure 9 shows the effect of the length to equivalent radius ratio (L/R_0) of 2 and 4, respectively, on the influence of minimum thickness on the buckling load of isotropic thickness-variable shell with b/a of 0.7 under follower lateral pressure. The trend of the results shown in Figure 9 is the same as the results presented in the previous sub-section. Moreover, according to Figure 9, although increasing L/R_0 does not significantly change the optimum value of hmin, it causes a significant reduction in the buckling load of the shell.



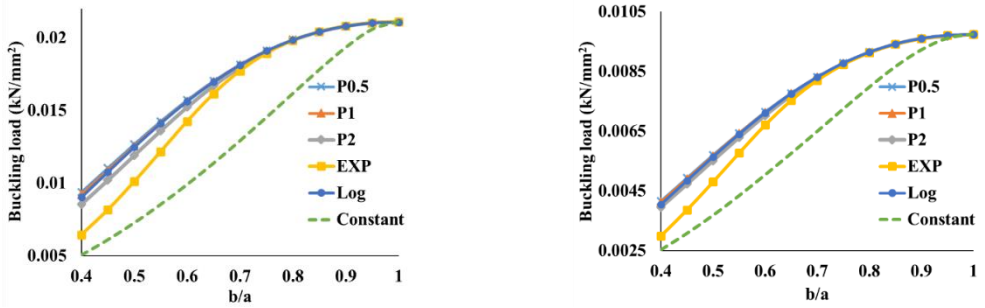
(a) (b)

Figure 9. Effect of variation of minimum thickness on buckling load of thickness-variable shell with b/a of 0.7 and different values of L/R_0 under follower lateral pressure (a) $L/R_0 = 2$ (b) $L/R_0 = 4$

As shown in Figure 9, for all cases, when hmin reaches its optimum value, the buckling load of the shell reaches its maximum value. In cases having optimum hmin, the shell undergoes general buckling, whereas in other cases, local deformations occur in limited regions of the shell.

4.3. Minimum to maximum diameters ratio of oval section (b/a)

The effect of the minimum-to-maximum diameter ratio of the oval section (b/a) on the buckling load of thickness-variable shells with optimum hmin and different values of L/R_0 ratio (2 and 4) under follower lateral pressure is shown in Figure 10.



(a) (b)

Figure 10. Effect of variation of b/a on buckling load of thickness-variable shell with optimum hmin and different L/R_0 values under follower lateral pressure (a) $L/R_0 = 2$ (b) $L/R_0 = 4$

The results indicate that applying a TVP in the elliptical shells can significantly increase the buckling load compared to shells with constant thickness, especially at lower b/a ratios. As the b/a ratio increases, the differences in buckling loads among various TVPs decrease, and the buckling load converge toward similar values. It indicates that applying a proper TVP on the circumferential direction is a suitable approach for enhancing the buckling load of elliptical cylindrical shells.

An index presenting the percentage Improvement in the Buckling Load (IBL) obtained for the shells having TVP compared to the constant thickness cases was defined to gain a deeper understanding of the effect of TVP on enhancement of buckling load of the elliptical shell under lateral follower pressure (Equation 34).

$$IBL = \frac{P_{Variable\ thickness} - P_{constant\ thickness}}{P_{constant\ thickness}} \times 100 \quad (34)$$

In Equation 34, $P_{Variable-thickness}$ and $P_{\text{constant thickness}}$ stand for the buckling loads of the thickness-variable and thickness-constant shells under lateral follower pressure. Figure 11 shows the effect of TVP on enhancement of buckling load of elliptical shell with different b/a values. In this figure, the ratio of L/R_0 is considered as 2 and 4. According to Figure 11, as L/R_0 ratio increases from 2 to 4, the effect of TVP on enhancement of buckling load decreases for all cases of b/a and TVP. For instance, the maximum IBL for L/R_0 ratios of 2 and 4 is about 36 and 65 percent, respectively. As depicted in Figure 11, the power-law TVP with power of 0.5 stands for the best TVP for enhancing the buckling load of elliptical shell.

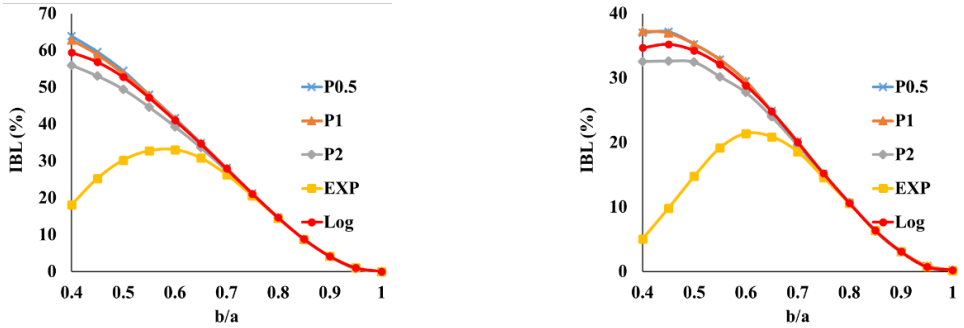


Figure 11. Effect of TVP on enhancement of buckling of elliptical shell with different b/a values under follower lateral pressure (a) $L/R_0 = 2$ (b) $L/R_0 = 4$

4.5. Lateral pressure type (follower or non-follower)

In this section, the effect of lateral pressure type (follower or non-follower) on the buckling behavior of a thickness-variable shell with the optimal hmin is evaluated. To reach a deep understanding of the influence of TVP on the difference between buckling loads of the shell under follower and non-follower pressures, firstly, the effect of b/a ratio on the difference between the buckling loads of a constant-thickness shell under follower and non-follower loads (considering L/R_0 of 8) is shown in Figure 12. The results presented in Figure 12 show that in the case of a shell with constant thickness, there is a significant difference between the buckling loads obtained for the shell under follower and non-follower pressures. This difference increases significantly with increasing b/a ratio. In order to investigate the effect of TVPs on this difference, the index defined in Equation 35 is calculated.

$$BLRD\% = \left|\frac{P_{follower\ pressure} - P_{non-follower\ pressure}}{P_{follower\ pressure}}\right| \times 100 \quad (35)$$

In Equation 35, BLRD stands for Buckling Load Relative Difference, $P_{follower\ pressure}$ is buckling load of the shell under follower pressure and $P_{non-follower\ pressure}$ represents the buckling load of the shell under non-follower pressure. The BLRD indicates the percentage difference between the buckling loads of the shell under the follower and non-follower pressures.

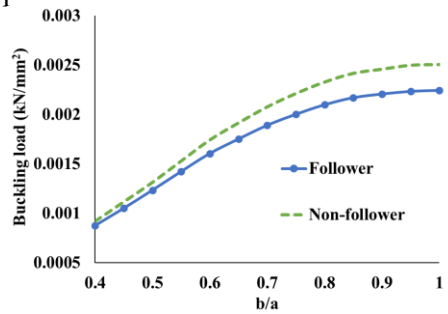


Figure 12. Effect of b/a ratio on the difference between the buckling loads of a constant-thickness shell under follower and non-follower loads (L/R_0 of 8)

Table 1 the effects of L/R_0, b/a and TVP on BLRE. As presented in this table, the BLRD increases for constant-thickness case and all TVPs and b/a ratios, as L/R_0 ratio increases. The rate of change in BLRD depends on the value of L/R_0; it is significantly higher when L/R_0 is between 8 and 16, compared to when it is less than 8 or greater than 16. Consequently, the maximum BLRD, approximately 35 percent, is observed at the highest values of both L/R_0 and b/a. According to Table 1, the lowest value of BLRD corresponds to the constant thickness pattern in all cases, while the highest BLRD, approximately 30%, is associated with the logarithmic TVP. Notably, the differences in BLRD among the various TVPs decrease significantly, as the b/a ratio increases. The BLRD values obtained for different TVPs show no significant differences at a b/a ratio of 0.9. This issue highlights the noticeable effect of TVPs on the buckling behavior of elliptical shells with smaller b/a ratios.

Table 1. Effects of L/R_0, b/a ratio and thickness variation pattern on BLRD

TVP	L/R \ b/a	0.4	0.5	0.6	0.7	0.8	0.9	1.0
Constant	1	0.11	0.19	0.27	0.41	0.55	0.73	0.91
	4	1.01	1.47	2.15	3.02	3.98	5.12	5.75
	8	2.51	3.68	5.42	7.30	9.35	10.99	11.65
	16	6.87	11.03	15.23	20.25	27.35	30.65	31.69
Power 0.5	1	0.53	0.67	0.75	0.85	0.87	0.90	0.91
	4	2.38	3.56	4.14	5.20	5.48	5.71	5.75
	8	3.87	6.36	8.20	9.98	10.83	11.95	11.65
	16	12.63	15.15	21.21	23.59	30.35	30.96	31.69
EXP	1	0.17	0.26	0.52	0.77	0.85	0.89	0.91
	4	1.17	2.21	3.64	4.72	5.42	5.62	5.75
	8	2.49	4.43	7.05	9.63	10.82	11.49	11.65
	16	7.19	10.97	15.80	22.24	29.04	31.45	31.69
Log	1	0.49	0.62	0.75	0.85	0.88	0.90	0.91
	4	2.42	3.63	4.46	5.13	5.50	5.64	5.75
	8	4.78	6.31	8.52	9.88	11	10.78	11.65
	16	14.84	16.81	20.64	28.13	28.57	31.17	31.69

5. Conclusions

A review of the previous studies shows that, the buckling load of elliptical cylindrical shells subjected to follower lateral pressure is significantly lower than that of the circular shell due to the uniform curvature of circular cross-sections. In this study, to enhance the buckling capacity of elliptical shells, the shell thickness is varied smoothly along the circumferential direction, with greater thickness assigned to regions of lower curvature. Three Thickness Variation Patterns (TVPs) (including power-law, exponential, and logarithmic) were considered in this study. A finite strip model of the shell was developed, and the buckling load was determined using the eigenvalue method. The accuracy of the developed model was validated by comparison with results obtained from finite element analysis. A comprehensive parametric study was conducted to assess the effect of geometric parameters and TVPs on the buckling of elliptical shells with circumferentially variable thickness. The main results obtained from the parametric study are summarized below:

- Despite keeping the material volume constant, the buckling load of thickness-variable elliptical shell is significantly higher than that of the constant thickness ones (up to 2 times).
- By increasing minimum to maximum diameters ratio of oval section (b/a) and length to equivalent radius ratio (L/R_0), the effect of TVP on enhancement of buckling load of the thickness-variable elliptical shell decreases.
- In all TVPs, the maximum buckling load was achieved when the minimum thickness of the elliptical shell (hmin) reaches an optimal value.
- As b/a ratio decreases, the optimal value of hmin decreases for all TVPs.

Funding Statement

This research was funded by Shahid Chamran University of Ahvaz, grant number SCU.C1403.530. The authors are grateful for the financial support provided.

Conflict of Interest

The authors declare that they have no conflict of interest.

AI Statement

The author(s) did not use AI tools for conducting this research.

Author Contributions

All authors contributed to the study conception, design, material preparation, analysis, writing first draft and final version of the manuscript.

References

1. Khajehdezfuly A, Poorveis D, Nazarinia S. Comparison between linear and nonlinear buckling loads of FGM cylindrical panel with cutout. Int J Non Linear Mech. 2023;150:104361.
2. Poorveis D, Khajehdezfuly A, Moradi S, Shirshekan E. A simple spline finite strip for buckling analysis of composite cylindrical panel with cutout. Lat Am J Solids Struct. 2019;16:e227.
3. Poorveis D, Khajehdezfuly A, Moradi S. Effects of position and shape of cutout on the axial buckling load of composite cylindrical panel. Amirkabir J Mech Eng. 2019;52(10):2879-98.
4. Tabish FNU, Mamaghani IHP. Buckling behavior and design optimization of stiffened-aluminum cylindrical shells under external pressure. J Struct Des Constr Pract. 2025;30(2):04025006.
5. Khan S, Kumar A. Buckling behaviour for advance cylindrical shells (COPV) subjected to extreme pressure conditions: A comprehensive review. Polym Compos. 2025.
6. Fazlalipour N, Ghanbari-Ghazijahani T, Showkati H. A review of buckling capacity of steel cylindrical shells under external pressure: reinforcements and imperfections (2005–Present). Thin-Walled Struct. 2025;113475.
7. Aksogan O, Sofiyev AH. Dynamic buckling of a cylindrical shell with variable thickness subject to a time-dependent external pressure varying as a power function of time. J Sound Vib. 2002;254(4):693-702.
8. Jabbari M, Nejad MZ, Ghannad M. Thermo-elastic analysis of axially functionally graded

rotating thick cylindrical pressure vessels with variable thickness under mechanical loading. Int J Eng Sci. 2015;96:1-18.
9. Fan H, Chen Z, Cheng J, Huang S, Feng W, Liu L. Analytical research on dynamic buckling of thin cylindrical shells with thickness variation under axial pressure. Thin-Walled Struct. 2016;101:213-21.
10. Ghareghani S, Loghman A, Mohammadimehr M. Analysis of FGM micro cylindrical shell with variable thickness using Cooper Naghdi model: bending and buckling solutions. Mech Res Commun. 2021;115:103739.
11. Bacciocchi M, Eisenberger M, Fantuzzi N, Tornabene F, Viola E. Vibration analysis of variable thickness plates and shells by the generalized differential quadrature method. Compos Struct. 2016;156:218-37.
12. Aghajari S, Abedi K, Showkati H. Buckling and post-buckling behavior of thin-walled cylindrical steel shells with varying thickness subjected to uniform external pressure. Thin-Walled Struct. 2006;44(8):904-9.
13. Chen Z, Yang L, Cao G, Guo W. Buckling of the axially compressed cylindrical shells with arbitrary axisymmetric thickness variation. Thin-Walled Struct. 2012;60:38-45.
14. Selahi E, Setoodeh AR, Tahani M. Three-dimensional transient analysis of functionally graded truncated conical shells with variable thickness subjected to an asymmetric dynamic pressure. Int J Press Vessel Pip. 2014;119:29-38.
15. Sofiyev AH. The buckling of an orthotropic composite truncated conical shell with continuously varying thickness subject to a time dependent external pressure. Compos Part B Eng. 2003;34(3):227-33.
16. Ghannad M, Rahimi GH, Nejad MZ. Elastic analysis of pressurized thick cylindrical shells with variable thickness made of functionally graded materials. Compos Part B Eng. 2013;45(1):388-96.
17. Fazlalipour N, Showkati H. Geometric properties and imperfections influence on buckling behavior of variable-thickness steel cylindrical shells subjected to combined loading: experimental and numerical study. Structures. 2023;55:834-52.
18. Bakulin VN, Nedbai AY. Dynamic stability of a composite cylindrical shell with linear-variable thickness under pulsed external pressure. J Eng Phys Thermophys. 2021;94(2):525-33.
19. Mahboubi Nasrekani F, Eipakchi H. Axisymmetric buckling of cylindrical shells with nonuniform thickness and initial imperfection. Int J Steel Struct. 2019;19:435-45.
20. Ghasemi AR, Hajmohammad MH. Evaluation of buckling and post buckling of variable thickness shell subjected to external hydrostatic pressure. J Solid Mech. 2017;9(2):239-48.
21. Khalifa Ahmed M. Elastic buckling behaviour of a four-lobed cross section cylindrical shell with variable thickness under non-uniform axial loads. Math Probl Eng. 2009;2009(1):829703.
22. Khalifa Ahmed M. A new vibration approach of an elastic oval cylindrical shell with varying circumferential thickness. J Vib Control. 2012;18(1):117-31.
23. Gusic G, Combescure A, Jullien JF. The influence of circumferential thickness variations on the buckling of cylindrical shells under external pressure. Comput Struct. 2000;74(4):461-77.
24. Yang L, Luo Y, Qiu T, Yang M, Zhou G, Xie G. An analytical method for the buckling analysis of cylindrical shells with non-axisymmetric thickness variations under external pressure. Thin-Walled Struct. 2014;85:431-40.
25. Feng WZ, Chen ZP, Jiao P, Zhou F, Fan HG. Buckling of cylindrical shells with arbitrary circumferential thickness variations under external pressure. J Mech. 2017;33(1):55-64.
26. Yang L. Analytical study on the buckling of cylindrical shells with circumferential thickness variation under varying external pressure. J Press Vessel Technol. 2024;146(4).
27. Birman V, Simitses GJ. Elliptical and circular cylindrical sandwich shells with different facings. J Sandwich Struct Mater. 2000;2(2):152-76.
28. Silvestre N. Buckling behaviour of elliptical cylindrical shells and tubes under compression. Int J Solids Struct. 2008;45(16):4427-47.
29. Moradi A, Poorveis D, Khajehdezfuly A. Buckling of FGM elliptical cylindrical shell under follower lateral pressure. Steel Compos Struct. 2022;175-91.
30. Poorveis D, Khajehdezfuly A, Sardari MR, Moradi S. An accurate approach for buckling analysis of stringer stiffened laminated composite cylindrical shells under axial

compression. Steel Compos Struct. 2024;51(5):545.
31. Khayat M, Poorveis D, Moradi S, Hemmati M. Buckling of thick deep laminated composite shell of revolution under follower forces. Struct Eng Mech. 2016;58(1):59-91.
32. Khayat M, Poorveis D, Moradi S. Buckling analysis of functionally graded truncated conical shells under external displacement-dependent pressure. Steel Compos Struct. 2017;23(1):1-16.



© 2025 by the authors. Licensee SCU, Ahvaz, Iran. This article is an open access article distributed under the terms and conditions of the Creative Commons Attribution 4.0 International (CC BY 4.0 license) (http://creativecommons.org/licenses/by/4.0/).

Uncertainty analysis for stability and cracking in a gravity dam using fuzzy theory (Case study of Pine Flat Dam)

Zahra Ashrafi [1], Mehdi Komasi [*,1] , Nazila Kardan [2]

1. Department of Civil Engineering, Faculty of Engineering, Ayatollah Boroujerdi University.
2. Department of Civil Engineering, Faculty of Engineering, Azarbaijan Shahid Madani University, Tabriz, Iran.

***Corresponding Author:**
Mehdi Komasi

Email: komasi@abru.ac.ir
Received: 2025.04.10
Accepted: 2025.07.09
J. Hydraul. Struct., 2025; 12(3):19-39
DOI: 10.22055/jhs.2025.49257.1344

ABSTRACT

This study employs fuzzy set theory and the α-cut method to quantify the uncertainty associated with the stability of the Pine Flat concrete gravity dam in California, using Cadam software. Triangular fuzzy numbers were assigned to key input parameters, including dam geometry and loading conditions. Three α-cuts (0, 0.5, and 1), representing 10%, 5%, and 0% uncertainty levels, were used to analyze the impact of input variability on output parameters. Results showed that crack length at the dam heel exhibited the highest sensitivity, with tensile stress at the same location identified as a critical output. A 10% input uncertainty led to a 270% increase in tensile stress uncertainty, highlighting the effectiveness of fuzzy analysis in capturing the nonlinear amplification of uncertainty. These findings underscore the value of fuzzy approaches in dam safety evaluations.

KEYWORDS

Cadam; Crack; Fuzzy; Graviy Dam; Uncertainty.

1. Introduction

Ensuring the safety and structural integrity of concrete dams is of paramount importance, given the potentially catastrophic consequences of dam failure for downstream populations [1]. Concrete dams are subject to various failure mechanisms, most notably sliding, overturning, and the development of tensile cracks or shear/compression-induced collapse [2]. These failure modes are influenced by multiple uncertainties, which can broadly be categorized as hydrological, hydraulic, economic, and structural [3].

Extensive research has been conducted to quantify and analyze these uncertainties. Notably, the application of the Monte Carlo method has been widely adopted in gravity dam analysis. Kostov et al. [4] assessed dam reliability by simulating various loading scenarios and illustrating outcomes using cumulative distribution function (CDF) diagrams. Yanmaz and Bézier [5] applied Monte Carlo simulation to evaluate the stability of Turkey's Porsuk Dam, identifying seven input variables and presenting the probability of failure based on safety factors. Similarly, Kittapcigil [6] examined the reliability of the Turkish Cinder Dam under diverse loading conditions. Altarajos et al. [7] analyzed sliding failure uncertainty using Monte Carlo simulation, showing graphical results of dam failure risk in relation to ten input variables.

Baghlani et al. [8] conducted a comprehensive uncertainty analysis on Bluestone Dam using Monte Carlo simulation integrated with Cadam software, presenting the outcomes through probability density functions. Ghafouri and Moradikia [3] investigated uncertainty and sensitivity at Pine Flat Dam using Cadam and Monte Carlo simulations, finding that a 10% variation in input parameters could lead to a 128% change in the dam's maximum tensile stress—emphasizing the significant influence of upstream water level over sediment pressure and seismic loading.

Further contributions to uncertainty modeling include the work of Ghorbani et al. [9], who used probabilistic analysis to assess how concrete strength variability affects scaled accelerograms in dynamic dam analysis. Mohammadi et al. [10] explored flood-related reservoir uncertainty using Monte Carlo simulation, revealing minimal variations in water levels of Dez, Karun, and Gotvand dams—0.037%, 0.107%, and 0.034%, respectively—caused by fluctuating inflow hydrographs.

In terms of cracking and failure mechanisms, several studies have investigated the physical behavior of dams under stress. Lin et al. [22] analyzed crack propagation in arch dams based on fracture toughness, using the Xiluodu Dam as a case study. Their findings established a correlation between field deformation monitoring data and crack propagation. Rebeiro and Leger [23] reviewed numerical modeling approaches and material models used to evaluate the safety of cracked concrete dams, applying Abaqus and the concrete damage plasticity model to simulate cracking behavior.

Liu et al. [24] examined seismic tensile cracking and its influence on slope stability in cemented sand and gravel (CSG) dams.

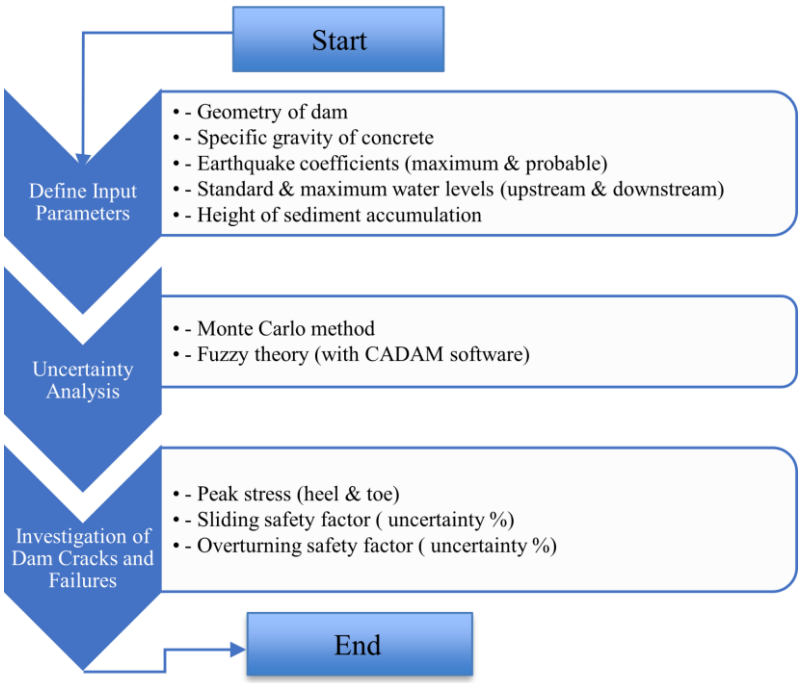


Figure. 1. Summary of the research conducted in this study.

Min et al. [25] showed that surface cracking in upstream zones may induce hydraulic fracturing, presenting a critical crack depth of 12.93 m and a width of 1.01 mm—2.53 times greater than the allowable limit. Zhou et al. [26] investigated the delayed failure of Brazil's Feijão Dam, proposing a mechanism involving progressive slip surface growth along weak layers. Xu et al. [27] proposed a three-dimensional branch-shaped failure mechanism and a finite element limit equilibrium method for analyzing rock dam stability, revealing that increased dam height and slope shift the critical slip surface to shallower regions.

In this context, the present study applies fuzzy set theory and the α-cut approach to evaluate the uncertainty in output parameters of the Pine Flat concrete gravity dam in California. Cadam software is used to model structural parameters and applied loads, with triangular fuzzy membership functions defining input uncertainty. Three α-cut levels (0, 0.5, and 1) are used to represent uncertainty levels of 10%, 5%, and 0%, respectively. The focus is on output parameters including safety factors against sliding and overturning, maximum tensile stresses at critical zones (heel and toe), and crack formation at the dam–foundation interface. The analysis particularly emphasizes tensile stress at the heel, which reduces the effective contact area and promotes crack initiation.

Overall, this research demonstrates how the fuzzy approach effectively captures nonlinear propagation of uncertainty in dam safety analysis, providing insights that complement and, in some respects, surpass traditional probabilistic methods [28].

2. Case Study

This research investigated the geometry and construction materials of the Pine Flat gravity concrete dam. Situated on the Kings River, approximately thirty miles east of Fresno, California, USA, the dam was primarily designed for flood control and to provide irrigation water for agriculture. The reservoir associated with the dam offers a diverse range of recreational facilities for both visitors and travelers. The dam's crest spans 560 m and consists of 37 blocks, each with a width of 15.2 m. The analysis included a detailed examination of the maximum block height, which measures 121.92 m. Fig.2, 3, and 4 show the cross-sectional view of the dam [3], the the structural view of the Pine Flat Dam, and the dam location map, respectively.

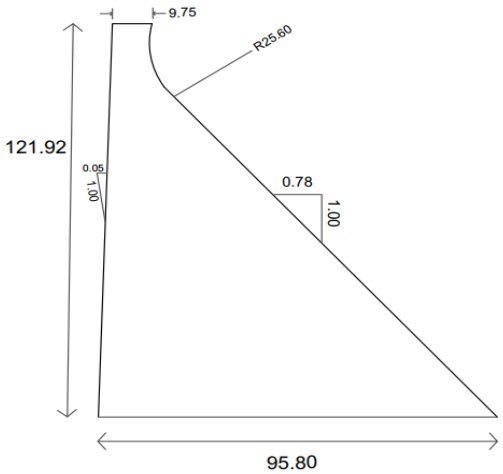


Figure 2. Geometry of Pine Flat Dam (m) [29].

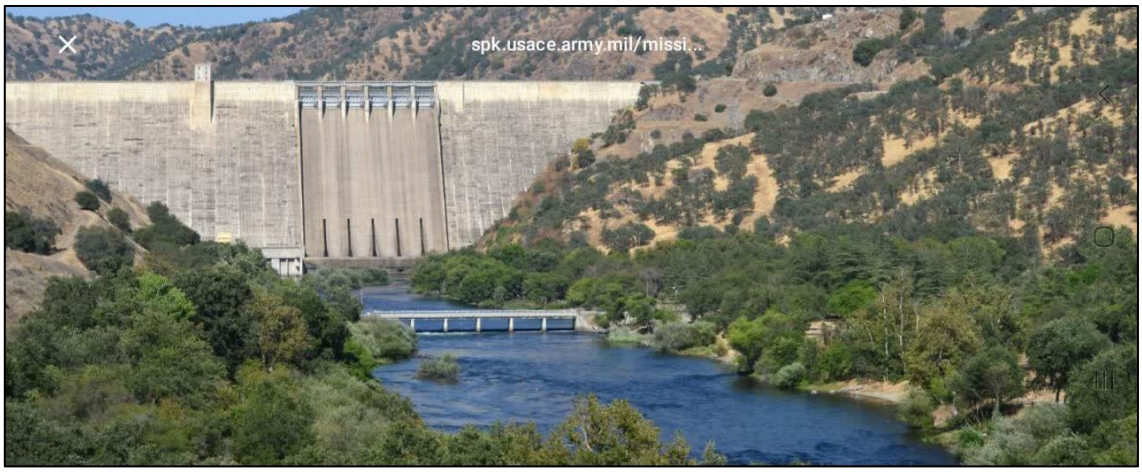


Figure 3. View of Pine Flat Dam Structure across Kings River.

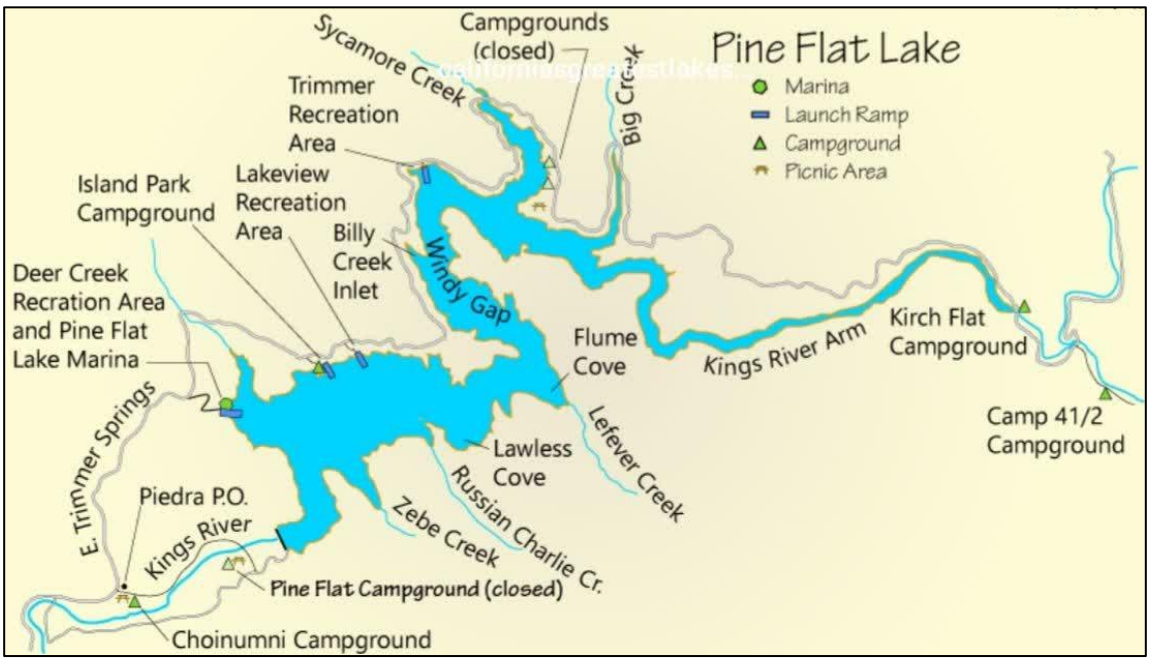


Figure 4. Map of Pine Flat Dam Location in California.

3. Material and Methods

The analysis of dam stability focuses exclusively on load combinations with a high likelihood of occurrence [2]. Table 1 outlines the standardized load combinations established by the United States Army Corps of Engineers (USACE), which include usual, unusual, and extreme load conditions.

Table 1. load conditions used for the stability analysis of gravity dams [31].

	Class	Earthquake	Headwater	Tail Water	Silt	Ice	Uplift
LC1	Unusual	-	-	-	-	-	-
LC2	Usual	-	Crest (top of gate)	Minimum	Yes	Yes	Yes
LC3	Unusual	-	SPF	Flood elevation	Yes	-	Yes
LC4	Extreme	OBE U.D.	-	-	-	-	-
LC5	Unusual	OBE D.D.	Usual pool level	Minimum	Yes	-	P.E.L.
LC6	Extreme	MCE D.D.	Usual pool level	Minimum	Yes	-	P.E.L.
LC7	Extreme	-	PMF	Flood elevation	Yes	-	Yes

Note: SPF (Standard Project Flood), PMF (Probable Maximum Flood), OBE (Operating Basis Earthquake), MCE (Maximum Credible Earthquake), U.D. (Upstream Direction), D.D. (Downstream Direction), P.E.L. (Pre-Earthquake Level), LC (Load Condition).

In Table 1, The load combinations (LC1 to LC7) include various classes of loading conditions categorized as Usual, Unusual, or Extreme, reflecting the severity and expected frequency of each scenario. Earthquake inputs include terms such as OBE (Operating Basis Earthquake) and MCE (Maximum Considered Earthquake), with directional indicators like U.D. (Upstream Direction) and D.D. (Downstream Direction) specifying the orientation of seismic forces. Headwater conditions are defined by levels such as the usual pool level, SPF (Standard Project Flood), PMF (Probable Maximum Flood), and crest elevation (top of gate). Tail water levels refer to either minimum downstream water elevation or flood elevation under extreme conditions. The presence of silt and ice loads on the upstream face of the dam are marked where applicable. Uplift pressures at the dam base are also considered, with some cases referring to P.E.L. (Potential Extreme Level), indicating uplift corresponding to critical high-water scenarios.

The gravity dam must adhere to specific criteria to resist both overturning and sliding. The following equations provide a method for calculating the safety factors against sliding and overturning. Eq. [1] defines the computation of the sliding safety factor for a horizontal surface under static conditions.

$$F_{sliding} = \frac{Total\ resistive\ forces\ along\ the\ slip\ plane}{Total\ driving\ forces\ along\ the\ slip\ plane} = \frac{\sum F_R}{\sum F_O} \quad (1)$$

Eq. [2] defines the computation of the overturning safety factor, which is determined by dividing the cumulative resisting moments by the total overturning moments relative to the toe or heel of the dam [2].

$$F_{overturning} = \frac{Total\ resistant\ moments}{Total\ driving\ moments} = \frac{\sum M_R}{\sum M_O} \quad (2)$$

The USACE has defined stability parameters for overturning and sliding, in addition to imposing constraints on critical internal stresses. Table 2 presents the safety factors for stability and sliding, as well as the stress criteria applicable to gravity dams under various loading conditions.

Table 2. USACE stability and stress criteria for gravity concrete dams [30].

Loading Condition	Sliding Safety Factor	Overturning Safety Factor	Compressive Stress	Tensile Stress
Usual	2	1.3	$0.5f'_c$	0
Unusual	1.7	1.2	$0.3f'_c$	$0.6f'^{\frac{2}{3}}_c$
Extreme	1.3	1.1	$0.9f'_c$	$1.5f'^{\frac{2}{3}}_c$

Note: f'_c is 1-year unconfined compressive strength of concrete.

3.1 Fuzzy Theory

A fuzzy set comprises elements that exhibit non-deterministic properties, each with a specific degree of membership. Unlike deterministic sets, where elements are strictly either members or non-members, fuzzy sets assign membership degrees based on specific criteria. Fuzzy sets can be better understood through a comparison with classical sets and the concept of membership degree. In classical sets, each element has a membership degree of one, while others have a membership degree of zero. An element is distinctly categorized as either a member or a non-member within classical sets. In contrast, fuzzy sets lack precise and clearly defined boundaries [19].

3.1.1 Fuzzy Analysis of Pine Flat Dam

The input parameters of the model in this study are defined as triangular fuzzy functions, incorporating the stresses applied to the dam and the material properties of the dam structure. The base value, which represents the unambiguous parameter value, is considered the most likely value with a membership degree of one in its fuzzy function. The number was recognized as an α-cut with a membership degree of one, along with another α-cut defining the 'abutment' interval as $[x_a, x_b]$, which corresponds to a membership degree of zero. Through the application of these two α-cuts, a triangular fuzzy function was formulated for each input parameter. To determine the minimum and maximum values of the "abutment" interval $[\boldsymbol{x_a}, \boldsymbol{x_b}]$, the desired input parameter was initially evaluated with certainty as the mean of the specified range. Subsequently, it was adjusted by increments and decrements of 10 percent to calculate the corresponding minimum and maximum values of the "abutment" interval. If a fuzzy number, denoted as N, is considered a subset of real numbers. Then every variable, like x, is assigned a membership degree within the interval [0,1] for $x \in N$, denoted as $\mu N(\epsilon)$, which reflects the degree of belonging to the fuzzy number. If x_c denotes the parameter value without uncertainty, it is shown in Eq. [3] and [4] [19].

$$x_{a.a} = x_c - \Delta x_\alpha \quad (3)$$

$$x_{b.a} = x_c + \Delta x_\alpha \quad (4)$$

According to Fig. 5, for the abutment interval [xc+Δx] and [xc-Δx] , Eq. [5] and [6] yield constant values.

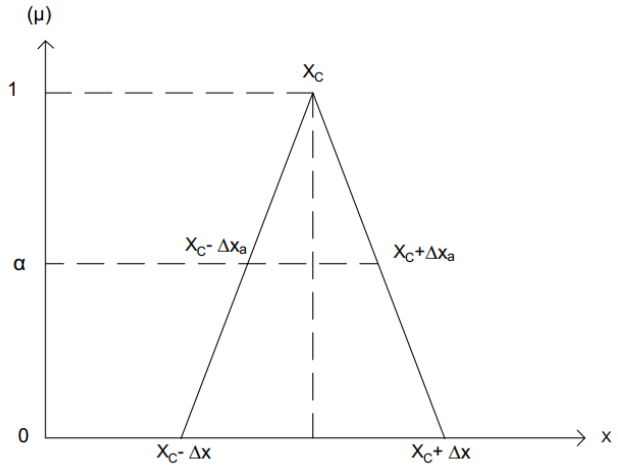


Figure 5. presents the input parameters in fuzzy format [10].

$\Delta x = 0.1x_c$ [5]

$\Delta x = 0.05x_c$ [6]

This entails identifying two α-cuts-one denoting the vertex of the fuzzy triangle set at one, and the other representing its base set at zero. A triangular fuzzy function was constructed for each specific input parameter. The values of xa, xb, and xc in the α-cut abutment, which is set at zero and signifies a 10% uncertainty in the desired input parameters, will be calculated [19]. At the outset, a fuzzy stability analysis and crack investigation of the Pine Flat concrete dam were conducted using deterministic values, devoid of uncertainty. An analysis of the maximum stresses within the dam structure, the stability coefficients related to sliding and overturning, and the extent of cracking at the dam heel-compared to the regulatory limits set by USACE- Table 3 shows that these values are comfortably below the specified thresholds. As a result, the dam is considered stable and compliant with the regulations.

Subsequent to an uncertainty-free assessment of dam stability, a fuzzy analysis was undertaken to account for uncertainty. Unlike conventional analytical methodologies, several geometric and technical parameters of the dam lack definitive and unambiguous values due to inherent uncertainties. Evaluating these uncertain values is imperative, considering the characteristics of the parameters, their significance, and the designer's perspective. Following a rigorous analysis of dam stability, a subsequent fuzzy analysis incorporating uncertainty was conducted. This study established triangular fuzzy functions for the dam material properties, foundation, and model input parameters, including variables such as water pressure on the upstream face of the dam, dam-specific gravity, and earthquake force

Table 3: The dam's stability factors were evaluated assuming no uncertainty.

Loading Condition	Sliding Safety Factor	Overturning Safety Factor	Compress Stress (KPA)	Tensile Stress (KPA)
Usual	2.01	1.82	-797	-1029
Unusual	1.75	1.47	-358	-2767
Extreme	1.35	1.34	-0.38	-2983

Note: fc' is 1-year unconfined compressive strength of concrete. In this case fc'=35MP

acceleration. The base value, defined as crisp value, was determined to be the most probable value with a membership degree of one in its fuzzy function. Tables 4 and 5 present the input parameters used in the Cadam software.

Table 4. Input parameters of the fuzzy model considering 5% uncertainty.

Parameter	Unit	Minimum value of the parameter x_a	Baselineparameter value x_c	Maximum value of the parameter x_b
Specific gravity of concrete	Kg/m^3	2357.9	2482	2606.1
Maximum earthquake coefficient	g	0.095	0.1	0.105
Probable earthquake coefficient	g	0.1425	0.15	0.1575
Standard water level on the upstream side	m	95	100	105
Standard water level on the downstream side	m	14.25	15	15.75
Maximum water elevation on the upstream side	m	104.5	110	115.5
Maximum water level on the downstream side	m	19	20	21
Height of sediment accumulation in the dam reservoir	m	19	25	21

Table 5. Input parameters of the fuzzy model considering 10% uncertainty.

Parameter	Unit	Minimum value of the parameter x_a	Baselineparameter value x_c	Maximum value of the parameter x_b
Specific gravity of concrete	Kg/m^3	2233.8	2482	2730.2
Maximum earthquake coefficient	g	0.09	0.1	0.11
Probable earthquake coefficient	g	0.135	0.15	0.165
Standard water level on the upstream side	m	90	100	110
Standard water level on the downstream side	m	13.5	15	16.5
Maximum water elevation on the upstream side	m	99	110	121
Maximum water level on the downstream side	m	18	20	22
Height of sediment accumulation in the dam reservoir	m	22.5	25	27.5

Fig. 6 demonstrates the need to obtain a corresponding α-cut in the output parameter fuzzy function for each α-cut in the input parameter fuzzy functions. Due to software limitations that accommodate only single values rather than numerical α-cuts, a methodology is required to extract the α-cut of the output fuzzy function without encompassing the entire range of values within the α-cut of the input parameter fuzzy functions. Treating the desired output parameter as a function of the designated fuzzy parameters, the scenario is formulated as an optimization problem. The constraints of this optimization problem are defined by the fuzzy input parameter range within the desired α-cut. To compute the α-cut of the output parameter, determining the maximum and minimum α-cuts from the optimization problem is sufficient.

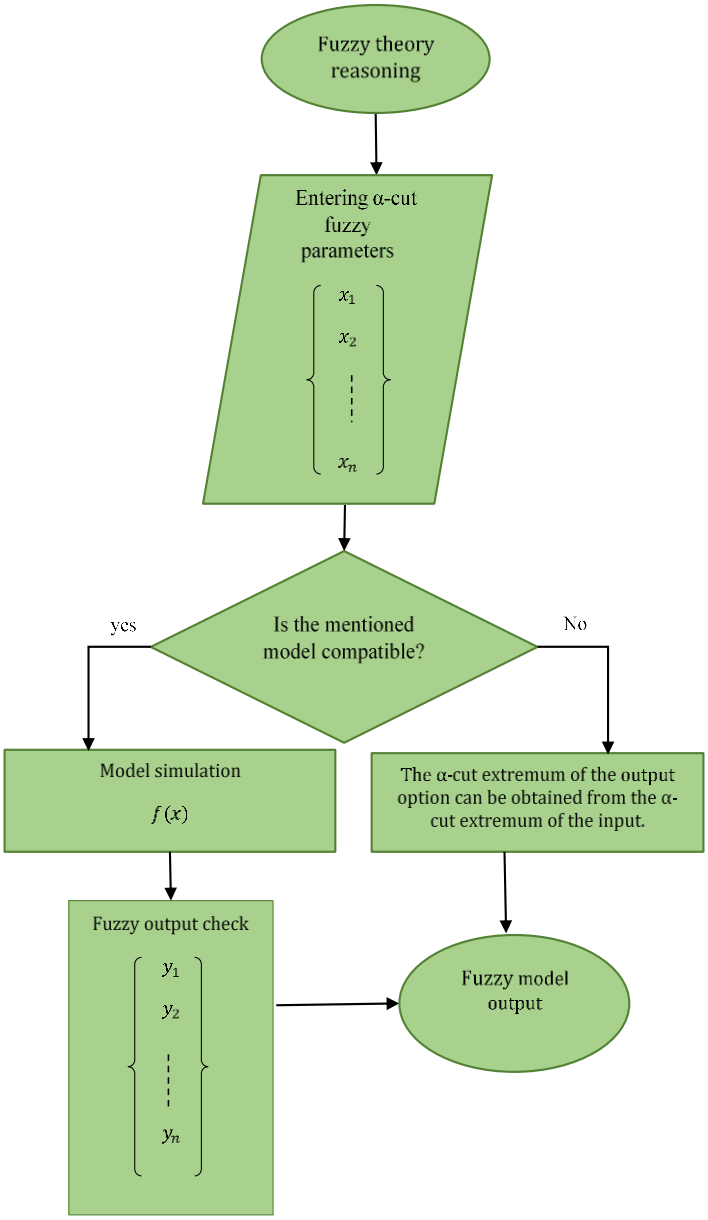


Figure 6. Consistency analysis of the fuzzy model in CADAM software.

In scenarios where the target output parameter exhibits non-monotonic behavior with respect to the parameters defined as fuzzy functions, an optimization strategy is essential to determine the minimum and maximum values of the output parameter's fuzzy function. Conversely, if the function is monotonic, an optimization procedure is unnecessary for determining these values. The minimum and maximum α-cuts of the input parameters play a crucial role in determining the corresponding α-cuts of the output parameter. The study by Ghafouri and Moradikia [3] highlights a novel issue in analyzing fuzzy input parameters for a concrete gravity dam model. Their research demonstrates that extracting the minimum and maximum α-cuts from the fuzzy functions of the input parameters is the primary method.

Consequently, the obtained α-cut serves as a means to define the fuzzy function of the desired output parameter. The decision to integrate the minimum and maximum α-cuts of an input parameter into the model hinges on the parameter's diminishing or augmenting impact on the desired output parameter. When the value of an input parameter rises proportionally with the desired output parameter, it is categorized as an augmenting factor. Similarly, a diminishing parameter can be characterized [31].

The Cadam software employs fuzzy analysis techniques to evaluate overturning and sliding stability coefficients in a concrete dam model. The structural model is created by inputting the dam's geometric dimensions, concrete's specific gravity, friction coefficient, and adhesion value at the dam-foundation interface.

Following this, dam modeling involves inputting the upstream and downstream water heights, specific gravity, sediment height, and gravitational acceleration coefficient to account for seismic forces.

The Cadam software can process various code loading combinations within a single model and present the results of specified parameters through a unified analysis, expediting result acquisition. This capability is particularly beneficial for research, including the current study, which requires extensive analysis. A detailed depiction of the research modeling process is provided in Fig. 7.

To establish the fuzzy functions of the output parameters, the diminishing and augmenting parameters outlined in Table 6 are first identified. After their classification as diminishing or augmenting, the minimum and maximum values for each α-cut of the fuzzy function corresponding to the specified coefficients are calculated.

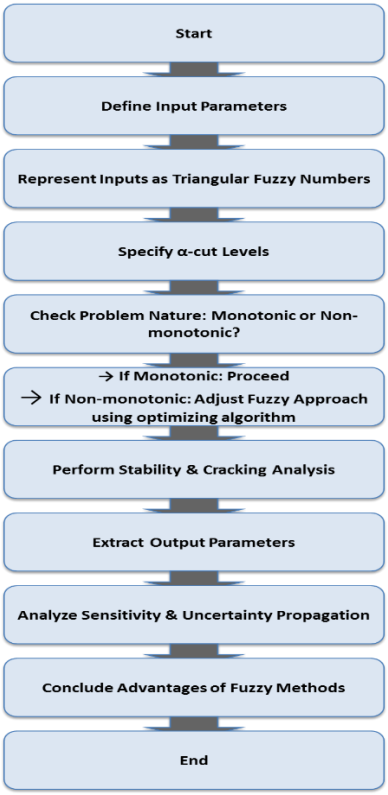


Figure 7. Comprehensive examination of the research methodology.

Table 6. Factors influencing the safety coefficients and stresses on the dam [21].

Input parameter	Safety factor for sliding stability	Safty factor for downstream overturning stability	Maximum tensile stress at the dam heel	Peak compressive stress at the dam toe	Number of safty factor at the dam toe
Water height upstream	Reduce	Reduce	Increase	Increase	Increase
Height of sediment accumulation behind the dam	Reduce	Reduce	Increase	Increase	Increase
Specific gravity of sediments	Reduce	Reduce	Increase	Increase	Increase
Specific gravity of concrete	Increase	Increase	Reduce	Reduce	Reduce
Seismic acceleration coefficient	Reduce	Reduce	Increase	Increase	Increase

Note: In load combination cases 1 and 4, as specified in Table 1, the impact of concrete specific gravity is the inverse of the values presented in Table 5.

4. Results and Discussion

4.1 The Analysis of Crack Values, Stresses, and Confidence Factors

To obtain the required fuzzy functions, three α-cuts (0, 0.5, and 1), representing 10%, 5%, and 0% uncertainty, respectively, were used. Subsequently, the Cadam program generated an output parameter consisting of five analytical models for each fuzzy function.

Tables 7 to 11 present the results of the models developed for all four output alternatives. The conclusions of this study align with the findings reported by Moradikia et al. in reference [21].

Table 7 shows that each variation in the input parameters results in a twofold variation in the output parameters. In summary, a 5% and 10% variability in the input leads to a 10% and 20% variability in the critical stresses. Moreover, in the absence of lateral forces such as seismic activity and hydrostatic pressure, the safety margins against overturning and sliding remain strong, eliminating the need for further investigation. The dam remains crack-free due to the absence of tensile stress. Regarding load combination 1, the sensitivity of the critical tensile and compressive stresses remains consistent.

Table 7. Outcomes for load combination 1.

Output parameter	In the absence of uncertainty	+5% uncertainty	-5% uncertainty	+10% uncertainty	-10% uncertainty
Peak stress at the dam heel(KPA)	-2767	-2906	-2629	-3044	-2490
Uncertainty percentage at the dam heel	-	10.0		20.0	
Peak stress at the dam toe(KPA)	-120	-126	-114	-132	-108
Uncertainty percentage at the dam toe	-	10.0		20.0	
Sliding safety factor	*	*	*	*	*
Percentage of uncertainty in the sliding coefficient of confidence	-	-		-	
Overturning safety factor	*	*	*	*	*
Percentage of uncertainty in the overturning safety factor	-	-		-	
Crack length as a percentage of the dam's length(M)	0	0	0	0	0
Percentage of uncertainty in crack length	0	0		0	

Note: The asterisk (*) in the table indicates an infinite value.

Table 8. out put for load combination 2.

Output parameter	Crisp	+5% uncertainty	-5% uncertainty	+10% uncertainty	-10% uncertainty
Peak stress at the dam heel (KPA)	-797	-1129	-455	-1306	-88
Uncertainty percentage at the dam heel	-	84.6		152.8	
Peak stress at the dam toe (KPA)	-1029	-856	-1187	-753	-1361
Uncertainty percentage at the dam toe	-	32.2		59.1	
Sliding safety factor	2.05	1.45	2.19	1.17	2.50
Percentage of uncertainty in the sliding coefficient of confidence	-	40.2		94.1	
Overturning safety factor	1.82	1.6	2.1	1.41	2.24
Percentage of uncertainty in the overturning confidence factor	-	27.5		45.6	
Crack length as a percentage of the dam's length	0	0	0	0	0
Percentage of uncertainty in crack length	0	0		0	

Table 8 indicates that the most notable sensitivity is associated with the critical tensile stress at the dam's heel, reaching 152%. This highlights the critical nature of tensile stress in load combination 2, as shown in Fig. 8, where the highest principal stress occurs at both the heel and toe of the dam. Furthermore, the results indicate the absence of structural cracks under this specific loading scenario, suggesting that the dam's stress levels remain stable in load combination 2, even with a 10% uncertainty.

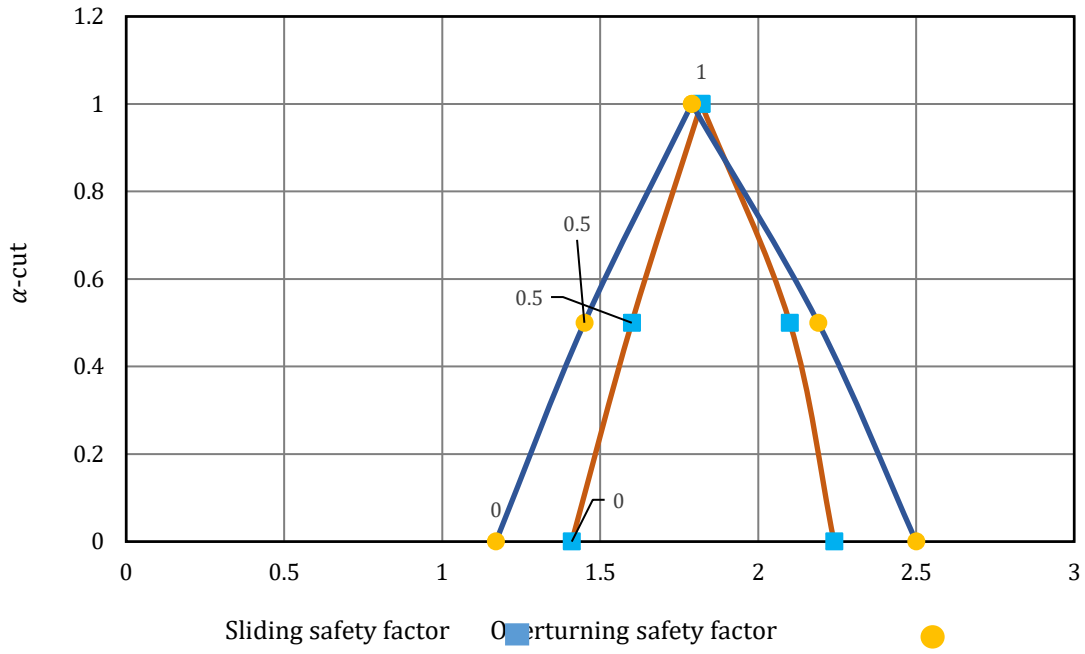


Figure. 8. Fuzzy function of the maximum principal stress at the dam's heel and toe under load combination 2.

Table. 9. Results for load combination 3.

Output parameter	In the absence of uncertainty	+5% uncertainty	-5% uncertainty	+10% uncertainty	-10% uncertainty
Peak stress at the dam heel	-358	-743	0.3	-970	0.38
Uncertainty percentage at the dam heel	-	207.6		270.8	
Peak stress at the dam toe	-1344	-1151	-1562	-974	-2059
Uncertainty percentage at the dam toe	-	30.5		80.7	
Sliding safety factor	1.75	1.06	1.73	0.89	1.98
Percentage of uncertainty in the sliding coefficient of confidence	-	47.7		76.9	
Overturning safety factor	1.54	1.31	1.76	0.89	1.98
Percentage of uncertainty in the overturning confidence factor	-	29.2		70.8	
Crack length as a percentage of the dam's length	0	0	8	0	36
Percentage of uncertainty in crack length	0	-		-	

Table 9 indicates that the tensile stress at the dam's base, with a variation of 270.8%, exhibits the highest degree of uncertainty regarding the stability of Pine Flat Dam, based on the assessment of cracks at the base in load combination 6. This is visually represented in Fig. 9, while Fig. 10 presents the safety factor values for both sliding and overturning. The results from this load combination suggest that, despite a 5% uncertainty in the dam's input parameters, a crack may form at the dam's base. However, this does not necessarily indicate imminent instability, as the modeling in this scenario assumes zero adhesion between the concrete and its foundation. Conversely, the regulatory framework for this load combination accounts for some tensile strength at the concrete-foundation interface, meaning that, in practice, crack formation may be prevented.

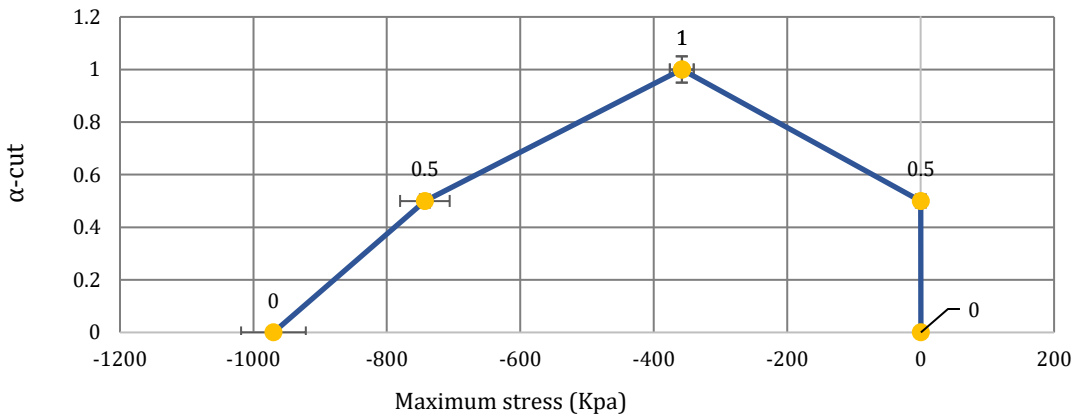


Figure 9. Fuzzy function of the maximum principal stress at the dam's base in load combination 3.

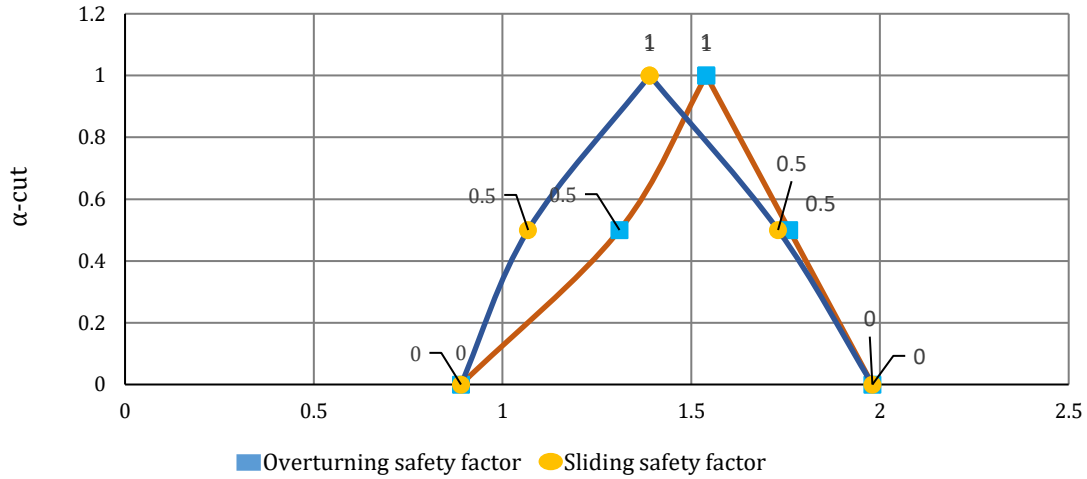


Figure 10. Fuzzy function of the safety factor against sliding and overturning in load combination 3.

Table 10. Results for load combination 4.

Output parameter	In the absence of uncertainty	+5% uncertainty	-5% uncertainty	+10% uncertainty	-10% uncertainty
Peak stress at the dam heel	-3388	-3597	-3020	-3811	-2983
Uncertainty percentage at the dam heel	-	17.0		24.4	
Peak stress at the dam toe	0.44	-1037	0.45	-1123	0.5
Uncertainty percentage at the dam toe	-	23578.1		255340.9	
Sliding safety factor	*	*	*	*	*
Percentage of uncertainty in the sliding coefficient of confidence	-	-		-	
Overturning safety factor	*	*	*	*	*
Percentage of uncertainty in the overturning confidence factor	-	-		-	
Crack length as a percentage of the dam's length	14.7	13.8	15.7	12	16.7
Percentage of uncertainty in crack length	-	12.9		31.9	

Note: The asterisk (*) in the table indicates an infinite value.

Table 10 demonstrates that there is a 5% uncertainty regarding the potential deformation at the dam's toe, which may subsequently lead to the development of cracks at the critical tensile stress point. A 10% discrepancy in the input parameters can introduce a 31.9% uncertainty in crack length. The minimal initial value of the dam's essential tensile stress gives rise to a substantial level of uncertainty, potentially creating a misleading perception.

Table 11. Results for load combination 5.

Output parameter	In the absence of uncertainty	+5% uncertainty	-5% uncertainty	+10% uncertainty	-10% uncertainty
Peak stress at the dam heel	-41	-554	0.41	-652	0.5
Uncertainty percentage at the dam heel	-	1350.2		1589.0	
Peak stress at the dam toe	-1786	-1011	-2082	-551	-3047
Uncertainty percentage at the dam toe	-	59.9		139.8	
Sliding safety factor	1.12	0.93	1.34	0.76	1.51
Percentage of uncertainty in the sliding coefficient of confidence	-	36.9		66.3	
Overturning safety factor	1.47	1.3	1.92	1.15	2.1
Percentage of uncertainty in the overturning confidence factor	-	42.2		64.6	
Crack length as a percentage of the dam's length	0	0	21	0	52.5
Percentage of uncertainty in crack length	-	-		-	

Table 11 demonstrates that a 5% deviation in the input parameters leads to a 21% increase in crack length, while a 10% uncertainty results in a 53% increase, compromising 53% of the dam base and rendering it unsafe. Consequently, load combination 5 poses a significant risk, especially due to the potential exacerbation by seismic forces. In contrast, the water pressure in other cases, such as load combinations 2 and 3, is insufficient to independently induce such a crack. Therefore, the combined effects of elevated water levels and seismic forces substantially increase the likelihood of additional cracks in the dam.

This unexpected result in Table 12 can be explained as follows: the initiation of a fracture at the dam heel causes the dam's base - which rests on the ground and serves to distribute force and generate stress on the foundation - to lift off the ground. The decrease in the foundation's cross-sectional area leads to an exponential increase in tensile stress. The results in Table 12 show an abnormal rise from 1,735 to 7,908, ultimately destabilizing the entire dam. This is illustrated in Fig. 11 for crack size and Fig. 12 for the safety factor against sliding and overturning.

Table 12. Results for load combination 6.

Output parameter	In the absence of uncertainty	+5% uncertainty	-5% uncertainty	+10% uncertainty	-10% uncertainty
Peak stress at the dam heel	0.5	-53	0.55	-324	0.65
Uncertainty percentage at the dam heel	-	10490.0		64670.0	
Peak stress at the dam toe	-2241	-1961	-3020	-1735	-7908
Uncertainty percentage at the dam toe	-	47.0		275.5	
Sliding safety factor	1.35	0.79	1.44	0.65	1.66
Percentage of uncertainty in the sliding coefficient of confidence	-	35.3		64.7	
Overturning safety factor	1.34	1.19	1.5	1.05	1.65
Percentage of uncertainty in the overturning confidence factor	-	23.1		44.8	
Crack length as a percentage of the dam's length	18.5	0	45	0	81
Percentage of uncertainty in crack length	-	243.2		437.8	

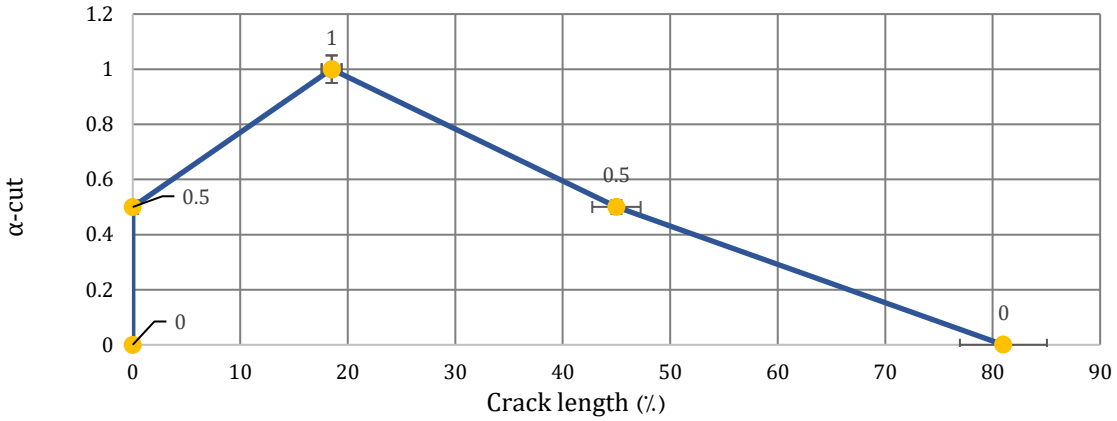


Figure 11. Fuzzy function of the crack amount for load combination 6.

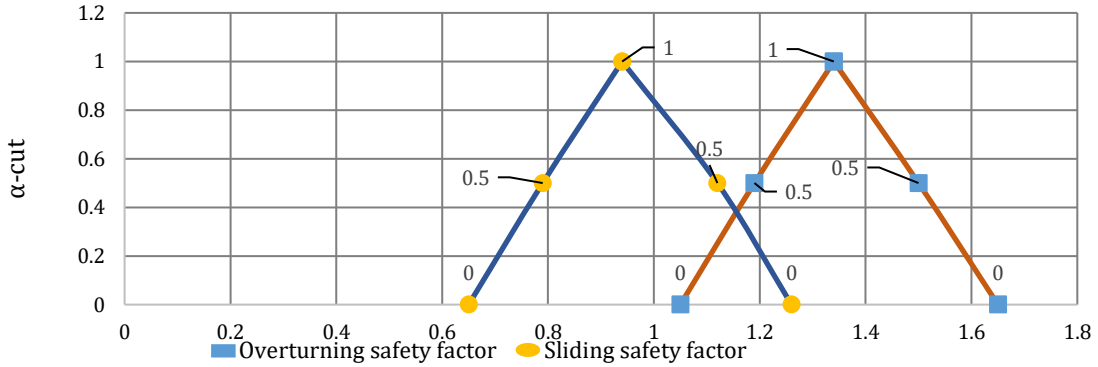


Figure 12. Fuzzy function of the safety factor against sliding and overturning for load combination 6.

5. Results and Discussion

This study presents an analysis of the stability of the Pine Flat gravity dam using fuzzy set theory and the α-cut method. To establish the necessary fuzzy functions, three α-cuts were used: 0, 0.5, and 1, corresponding to 10%, 5%, and 0% uncertainty, respectively. The α-cut at 0 is the most significant, as it represents a 10% uncertainty in the model's input parameters, resulting in the highest uncertainty in the output parameters. Therefore, the results of this α-cut are thoroughly examined. Nevertheless, the percentage uncertainties in the output parameters were excessively large, particularly in the maximum tensile stresses under loadings 5 and 6. This issue stemmed from the low base parameter values, set at half a kilopascal. Consequently, the percentage uncertainties calculated based on these values are unreliable. By representing model input parameters associated with uncertainty-such as dam material specifications and applied loads-as triangular fuzzy functions and incorporating them into the Cadam concrete dam analysis programs, the safety factors against sliding and overturning, as well as the principal stresses and fissures at the dam's base, were determined as fuzzy functions. An uncertainty analysis of the specified output parameters was then performed using the derived fuzzy functions. Given a consistent geometry for concrete gravity dams, the elastic modulus and specific gravity of the dam can be determined using fuzzy analysis by considering the applied loads and only the minimum and maximum input parameter values. Consequently, fuzzy values for output parameters, such as critical stresses, crack thresholds, and safety factors against sliding and overturning, can be identified without the need for an optimization algorithm.

1) The results of this study suggest that the model's fuzzy responses are more practical than its classical counterparts, providing enhanced insights into the dam's future performance.
2) Introducing minor inaccuracies in the input parameters of the weighted dam analysis leads to significant changes in the output parameters. A 10% deviation in the model's input parameters could result in a 270.8% variation in the maximum tensile stress at the dam toe.
3) The spectrum of cracking variations in concrete gravity dams ranges from minor surface damage to significant structural failure. A 10% variability in the input parameters results in a 437.8% variation in the output parameters associated with the dam's crack. This unforeseen outcome can be explained as follows: the initiation of a crack at the dam's heel leads to the uplifting of the dam's base, which serves as an abutment to distribute force and generate tension on the foundation. Consequently, the reduction in the foundation's cross-sectional area causes a significant rise in tensile stress, increasing from 1,735 to 7,908, as demonstrated in the results table, ultimately destabilizing the entire dam.The stability coefficients for overturning and sliding, along with the stresses and cracks observed in the dam under specific conditions, adhered to regulatory limits, indicating stability. Conversely, under uncertainty, these parameters exceeded regulatory thresholds, leading to the dam's destabilization.

Statements and Declarations

The authors declare that they have no conflict of interest.

Competing Interests

This research work is not supported by any funding agency.

Financial Disclosure Statement

The author(s) received no specific funding for this work.

Funding

This research did not receive any specific grant from funding agencies in the public, commercial, or not-for-profit sectors.

Authors' Contributions

All authors contributed to the study conception and design. Material preparation, data collection, and analysis were performed by Zahra Ashrafi, Mehdi Komasi, and Nazila Kardan. The first draft of the manuscript was written by Zahra Ashrafi and all authors commented on previous versions of the manuscript.

Data Availability

The data presented in this study are available on request from the corresponding author.

Consent for Publication

All the authors have read and agreed to the submitted version of the manuscript.

Acknowledgement

The authors would like to thank the editors and reviewers for their valuable comments and suggestions to improve the presentation of this paper.

Refrences

1. Lave, L. B., & Balvanyos, T. (1998). Risk analysis and management of dam safety. Risk Analysis, 18(4),455-462. https://doi.org/10.1111/j.1539-6924.1998.tb00360.x
2. Ghanbari, A. (2014). Principles of earth dam engineering. Kharazmi University.
3. Ghafouri, H. R., & Moradi Kia, F. (2016). Uncertainty analysis of gravity concrete dam using Monte Carlo simulation (Case study: Pine Flat Dam). Proceedings of the 1st National Conference on Engineering and Construction Management, Sharif University of Technology, Tehran, Iran.
4. Kostov, M., Boncheva, H., Stefanov, D., Varbanov, G., Kaneva, A., & Koleva, N. (1998). Seismic risk assessment of large concrete gravity dams. In Proceedings of the 11th European Conference on Earthquake Engineering.
5. Yanmaz, A. M., & Beşer, M. R. (2005). On the Reliability-Based Safety Analysis of the Porsuk Dam. Turkish Journal of Engineering & Environmental Sciences, 29(5).
6. Kitapcıgil, S. N. (2010). A study on the reliability-based safety analysis of hardfill dams (Master's thesis). Middle East Technical University.
7. Altarejos-García, L., Escuder-Bueno, I., Serrano-Lombillo, A., & de Membrillera-Ortuño, M. G. (2012). Methodology for estimating the probability of failure by sliding in concrete gravity dams in the context of risk analysis. Structural Safety, 36–37, 1–13. https://doi.org/10.1016/j.strusafe.2012.01.001
8. Baghlani, A., Satari, M., & Makiabadi, M. H. (2012). Reliability analysis of gravity concrete dams using Monte Carlo simulation. Proceedings of the 3rd National Conference on Earthquake and Structures.
9. Ghorbani, M. A., Jalali, M., & Pasbani Khiawi, M. (2021). Investigation of the uncertainty due to the effect of concrete strength in the seismic representation of a concrete roller dam by applying different scaled accelerograms using the Monte Carlo method. Proceedings of the First National Conference on Civil Engineering, Smart Development and Sustainable Systems.
10. Mohammadi, B., Radfar, M., Fathian, H., & Mirabassi Najafabadi, R. (2023). Uncertainty analysis of the water level of the Karun and Dez dam reservoirs due to the inflow hydrograph uncertainty. Journal of Water and Irrigation Management, 13(4), 855-871. https://doi.org/10.22059/jwim.2023.358580.1071
11. 11 .Zadeh, L. A. (1965). Fuzzy sets. Information and Control, 8(3), 338– https://doi.org/10.1016/S0019-9958(65)90241-X
12. Mamdani, E. H., & Assilian, S. (1975). An experiment in linguistic synthesis with a fuzzy logic controller. International Journal of Man-Machine Studies, 7(1), 1-13. https://doi.org/10.1016/S0020-7373(75)80002-2

13. Zimmermann, H. J. (2010). Fuzzy set theory. Wiley Interdisciplinary Reviews: Computational Statistics, 2(3), 317-332. https://doi.org/10.1002/wics.82
14. Bit, A., Biswal, M., & Alam, S. (1993). Fuzzy programming approach to multiobjective solid transportation problem. Fuzzy Sets and Systems, 57(2), 183-194. https://doi.org/10.1016/0165-0114(93)90158-E
15. Hanss, M., & Turrin, S. (2010). A fuzzy-based approach to comprehensive modeling and analysis of systems with epistemic uncertainties. Structural Safety, 32(6), 433-441. https://doi.org/10.1016/j.strusafe.2010.06.003
16. Valdebenito, M., Jensen, H., Beer, M., & Pérez, C. (2014). Approximation concepts for fuzzy structural analysis. In Vulnerability, uncertainty, and risk: Quantification, mitigation, and management (pp. 135-144). ASCE
17. Balu, A., & Rao, B. (2014). Efficient assessment of structural reliability in presence of random and fuzzy uncertainties. Journal of Mechanical Design, 136(5), 051008. https://doi.org/10.1115/1.4026650
18. Sieniawska, R., Zielichowski-Haber, W., & Zukowski, S. (2014). Safety estimation of the plate-girder structures with uncertain parameters from the shakedown theory point of view. In Vulnerability, uncertainty, and risk: Quantification, mitigation, and management (pp. 1283-1292). ASCE.
19. Haghighi, A., & Ayati, A. (2015). Uncertainty analysis of stability of gravity dams using the fuzzy set theory. International Journal of Optimization in Civil Engineering, 5(4), 465-478.
20. Rahimi, Y., Thaqafiyan, B., & Bani Hashemi, M. A. (2020). Risk-based optimization of flood diversion system of Karun 4 Dam under hydraulic and hydrological uncertainties. Iranian Soil and Water Research, 51(10), 2575-2591. https://doi.org/10.22059/ijswr.2020.301315.668585
21. Moradi Kia, F., Ghafouri, H. R., & Riyahi, M. M. (2022). Uncertainty analysis and risk identification of the gravity dam stability using fuzzy set theory. Journal of Hydraulic Structures, 7(4), 76-92. https://doi.org/10.22055/jhs.2022.37593.1176
22. Lin, P., Guan, J., Peng, H., & Shi, J. (2019). Horizontal cracking and crack repair analysis of a super high arch dam based on fracture toughness. Engineering Failure Analysis, 97, 72-90. https://doi.org/10.1016/j.engfailanal.2019.01.036
23. Ribeiro, P. M. V., & Léger, P. (2023). On a Benchmark Problem for Modeling and Simulation of Concrete Dams Cracking Response. Infrastructures, 8(3), 50. https://doi.org/10.3390/infrastructures8030050
24. Liu, P., Chen, J., Xu, Q., & Fan, S. (2023). Seismic stability analysis of CSG dams considering the effect of tension crack based on genetic algorithm with an improved initial population strategy. Soil Dynamics and Earthquake Engineering, 175, 108210. https://doi.org/10.1016/j.soildyn.2023.108210
25. Min, Q., Zhang, M., Li, M., He, Y., Bordas, S. P., & Zhang, H. (2024). Hydraulic fracturing simulation of concrete dam integrating intelligent crack detection and refined modeling methods. Engineering Structures, 305, 117760. https://doi.org/10.1016/j.engstruct.2024.117760
26. Zhu, F., Zhang, W., & Puzrin, A. M. (2024). The slip surface mechanism of delayed failure of the Brumadinho tailings dam in 2019. Communications Earth & Environment, 5(1), 33.
27. Xu, M., Zhou, Y., Pang, R., Xu, B., & Zhang, Y. (2024). A novel finite element limit equilibrium method and its application in instability analysis for 3-D high core rockfill dams. Structures, 63, 107066.

https://doi.org/10.1016/j.istruc.2024.107066
28. Haghpanah, M., & Wasadi, E. (2019). Investigation of types of cracking in concrete dams and their causes. 8th National Conference on Civil Engineering, Architecture and Sustainable Urban Development of Iran.
29. Sabzvari, Touraj. (2008). Stability analysis of gravity concrete dams using Cadam200 software. Journal of Water Resources Engineering Science, 1(2), 10-11
30. U.S. Army Corps of Engineers. (1995). Gravity dam design: Chapter 4 - Stability analysis (EM 1110-2-2200). U.S. Army Corps of Engineers.
31. Haghighi, A., & Ayati, A. H. (2016). Stability analysis of gravity dams under uncertainty using the fuzzy sets theory and a many-objective GA. Journal of Intelligent & Fuzzy Systems, 30, 1857-1868. https://doi.org/10.3233/IFS-151897

© 2025 by the authors. Licensee SCU, Ahvaz, Iran. This article is an open access article distributed under the terms and conditions of the Creative Commons Attribution 4.0 International (CC BY 4.0 license) (http://creativecommons.org/licenses/by/4.0/).

Investigation of the Effect of Time-Dependent Viscosity on the Penetration of Cement Grout in Rock Fractures Using a Numerical Modeling Approach

Alireza Sadooghi [1], Ali Aalianvari [*,1] ,Hamidreza Shahbazian [2]

1. Department of Mining Engineering, University of Kashan, Kashan, Iran.
2. Department of Mechanical Engineering, University of Kashan, Kashan, Iran.

***Corresponding Author:**
Ali Aalianvari,

Email: ali_aalianvari@kashanu.ac.ir
Received: 2025.06.10
Accepted: 2025.10.30
J. Hydraul. Struct., 2025; 12(3):40-53
DOI: 10.22055/jhs.2025.49928.1354

ABSTRACT

The effect of time-dependent viscosity on cement grout penetration in rock fractures, critical for enhancing the stability and impermeability of underground structures like tunnels and dams, was investigated. We developed an analytical model based on Newton's second law, assuming a frictionless horizontal fracture and modeling grout as a rheopectic Bingham fluid. Grouts with density of 1325, 1475, 1625, and 1725 kg/m³, derived from varying water-to-cement ratios, have been analyzed. Numerical simulations, conducted using Gambit for mesh generation (1.225 million 2D cells, 3.15 million 3D cells) Done, and by investigating various viscosity functions to achieve the optimal combination with maximum penetration depth, processing has been carried out in ANSYS Fluent. Results show that higher water-to-cement ratios lower viscosity, increasing washout risks, while higher density accelerates setting, reducing penetration depth. A gradual 0.01-bar injection pressure has been shown to optimize penetration by minimizing filter cake formation. Governed by Navier-Stokes equations, the Bingham model accurately describes grout rheology, with stoppage times of 1–13 minutes influenced by viscosity and density. Validated against experimental data, the models provide a robust framework for optimizing injection parameters, offering practical solutions for effective water seepage control in underground engineering.

KEYWORDS

Time-dependent viscosity, Grout penetration, Bingham fluid, Numerical modeling, Underground engineering.

1. Introduction

The growing demand for underground infrastructure, such as tunnels and dams, underscores challenges posed by groundwater seepage, which can deplete groundwater resources, cause geological instability (e.g., tunnel wall collapse or surface fractures), and result in substantial financial losses. Grouting, a technique involving the injection of a liquid mixture (grout) into rock fractures, is widely used to enhance rock mass stability and prevent water seepage [1]. This method, pioneered by Charles Berigny in 1802 for underwater structure repairs [2], relies heavily on the rheological properties of the grout, particularly its viscosity, which varies with time. The water-to-cement ratio significantly affects viscosity: a high ratio reduces viscosity, increasing the risk of grout washout, while a low ratio increases viscosity, reducing adhesion to rock surfaces.

The grout's rheological behavior aligns with the Bingham model, necessitating precise injection pressure tailored to rock characteristics and engineering requirements. Although prior studies on injection fluids, such as cement-glass and cement-polymer [3-7], have advanced grout modeling, accurately simulating grout propagation under dynamic water conditions remains challenging.This study focuses on analyzing the impact of time-dependent viscosity on grout penetration, aiming to optimize injection parameters for effective water seepage control in underground structures. This study aims to: (1) develop an analytical model for time-dependent grout flow, (2) simulate penetration using computational fluid dynamics (CFD) with varying grout densities, and (3) optimize injection parameters for seepage control. Key contributions include validated viscosity functions and practical recommendations for minimizing washout in dynamic water conditions.

2. Literature Review

2.1. Time-Dependent Viscosity of Cement Grouts

The time-dependent viscosity of cement grouts plays a pivotal role in their effectiveness when injected into fractured rock masses. Ruan [8] formulated an analytical model for grout transport in fractured media, integrating time-varying viscosity to estimate penetration length, emphasizing its critical influence on grout flow under hydraulic gradients. Sonebi [9] performed experimental studies on cement-based grouts enhanced with viscosity-modifying agents, such as diutan and welan gums combined with pulverized fly ash, showing that these additives significantly enhance grout stability and flowability, minimizing segregation under high-pressure injection. Similarly, Şahmaran et al. [10] investigated natural zeolite as a viscosity modifier, demonstrating improved rheological stability and reduced bleeding in grouts, especially in mixtures with high water-to-cement ratios. Their results indicate that natural additives can enhance grout performance in challenging geological environments.

Quinn and Karol [11,12] advanced the numerical modeling of time-dependent viscosity using OpenFOAM software, developing models that account for the rheopectic behavior of grouts. Their work included laboratory experiments to validate numerical predictions, showing that viscosity increases exponentially over time, impacting penetration depth and setting time. Li et al. [13] investigated the apparent viscosity of cement grouts across a range of water-to-cement ratios, proposing empirical models to describe time-dependent behavior. Their results indicated that lower water-to-cement ratios lead to faster viscosity increases, limiting penetration but enhancing grout stability. Assaad [14] introduced a novel real-time monitoring technique for viscosity changes and water extraction during grouting, which allowed for dynamic adjustment of injection parameters to optimize penetration. This method proved effective in reducing washout risks in dynamic water environments.

Further studies have explored the influence of external factors on grout viscosity. Gustafson et al. [15] analyzed the impact of hydraulic gradients on grout flow, emphasizing the need for adaptive viscosity models in high-flow conditions. Eftekhari et al. [16] investigated the interaction between grout viscosity and fracture aperture, finding that smaller apertures increase resistance to flow, necessitating higher injection pressures or modified grout compositions. These studies collectively underscore the complexity of modeling time-dependent viscosity and the need for integrated analytical and experimental approaches to predict grout behavior accurately. Key research gaps include the lack of 3D simulations capturing rheopectic behavior and the integration of time-dependent viscosity with realistic injection pressures, which this study addresses through validated CFD models.

2.2. Stable Grout Composition and Permeability

The composition of grout is crucial for achieving effective sealing and structural reinforcement in rock fractures. Water, as the primary constituent, significantly influences grout fluidity and

setting properties. Hanson [17] performed filter pump tests to assess how the water-to-cement ratio affects grout permeability, finding that higher ratios increase permeability, raising the risk of washout under high hydraulic gradients. Conversely, Eriksson et al. [18] utilized permeameter tests to suggest that the water-to-cement ratio has a less pronounced effect than previously thought, highlighting the importance of fracture geometry and grout additives. Eklund and Stille [19] conducted an in-depth analysis of permeability factors, pinpointing grain size, grain size distribution, superplasticizers, chemical reactions, and fracture roughness as critical factors. Their findings underscore the necessity of customizing grout formulations to suit specific geological and hydraulic conditions.

Additional studies have focused on optimizing grout composition for stability. Samiei et al [20] and Nonveiller [21] provided foundational insights into the design of cement-based grouts, emphasizing the balance between fluidity and cohesion to prevent segregation. Houlsby [22] and Bruce [23] explored the use of chemical additives to enhance grout stability, particularly in high-pressure environments. Lombardi [24] investigated the role of cohesion in cement grouting, proposing that cohesive grouts are more effective in narrow fractures due to reduced leakage. Nazari et al. [25] examined advanced grouting techniques for dam foundations, recommending cyclic pressure testing to identify stable compositions that withstand dynamic water flow. The process of determining an optimal grout mix involves several steps: (1) analyzing physical and chemical properties (e.g., adhesion, compressive strength), (2) assessing hydraulic system conditions (e.g., pressure, flow rate, temperature), (3) testing commercially available mixtures, (4) conducting laboratory experiments under varying conditions, and (5) iteratively refining the mix to achieve optimal performance. These studies collectively highlight the importance of a multidisciplinary approach to grout design, combining rheological, hydraulic, and geotechnical considerations.

2.3. Research Gaps and Current Study

Despite significant advancements, several gaps remain in the literature. Most studies focus on static or simplified fracture conditions, with limited attention to dynamic water flow and fracture roughness. Additionally, while numerical models like those by Quinn and Karol [11,12] have improved viscosity predictions, their validation in complex geological settings is limited. The interaction between time-dependent viscosity and injection pressure in three-dimensional fracture networks also requires further exploration. This study addresses these gaps by developing an analytical and numerical framework to model grout penetration, incorporating time-dependent viscosity and realistic hydraulic conditions, with validation against experimental data.

3. Methodology

An analytical model based on Newton's second law was developed, assuming a horizontal fracture with smooth, frictionless parallel surfaces. The grout was modeled as a Bingham fluid with yield stress (τ0 and plastic viscosity (μ), governed by the rheological equation:

$$\tau=\tau_0+\mu\dot{\gamma} \quad (1)$$

where τ_0 is shear stress, and $\dot{\gamma}$ is the shear strain rate (see Figure 1 for the Bingham model zones). The approximate motion of a Newtonian fluid in a fracture joint is illustrated in Figure 2, providing a baseline for comparison.

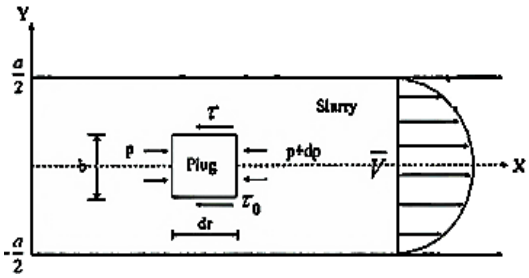


Figure 1: Bingham grout model illustrating plug and velocity gradient zones.

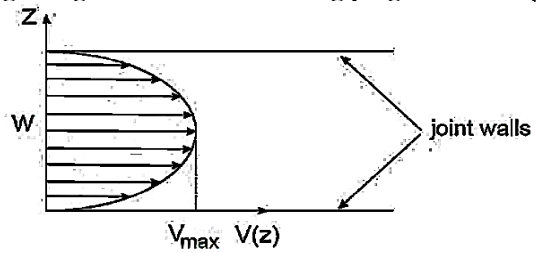


Figure 2: Approximate motion of a Newtonian fluid within a fracture joint.

Navier-Stokes equations were used to analyze fluid flow, with continuity and momentum equations solved for various conditions.

3.1. Numerical Modeling

The fracture geometry, featuring an 8-meter length, a 2 mm inlet, and a 1 mm outlet, was constructed using Gambit (Figure 3). The model was discretized with 1.225 million cells for 2D simulations and 3.15 million cells for 3D simulations, employing a square mesh with a 4.654 inflation ratio and a 0.1-micron cell size to ensure high precision. Details of the boundary conditions and meshing for both 2D and 3D models are illustrated in Figure 4a-c, including open inlet and outlet, impermeable walls, and a constant pressure differential of 0.01 bar.

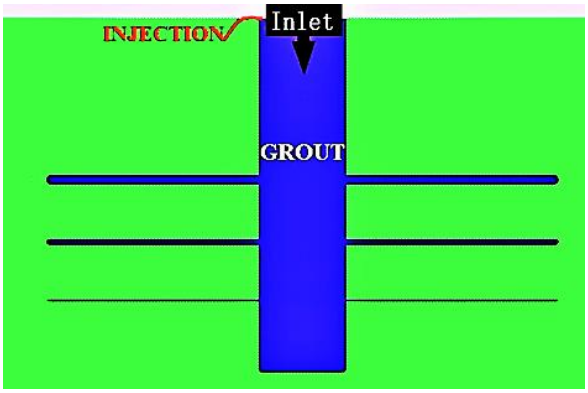


Figure 3: Initial model of a borehole with fractures and grout injection path in Gambit.

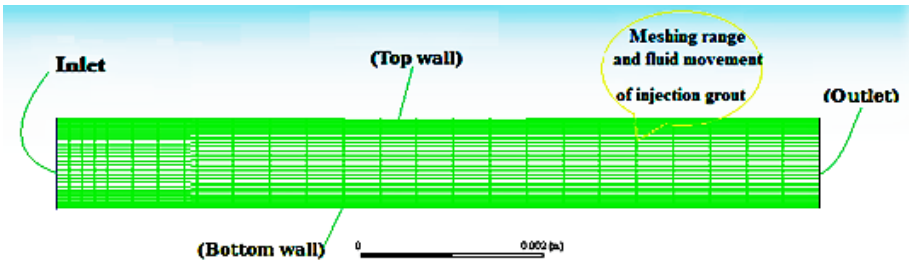


Figure 4a: Boundary conditions and specifications for the 2D model.

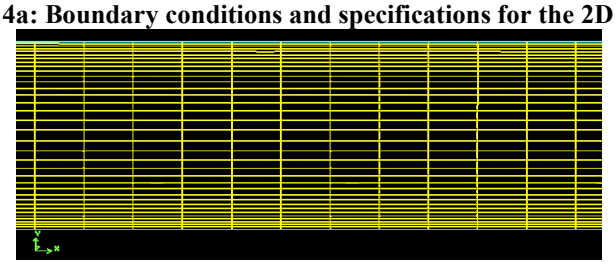


Figure 5b: Cross-section of 2D mesh for a fracture segment in Gambit.

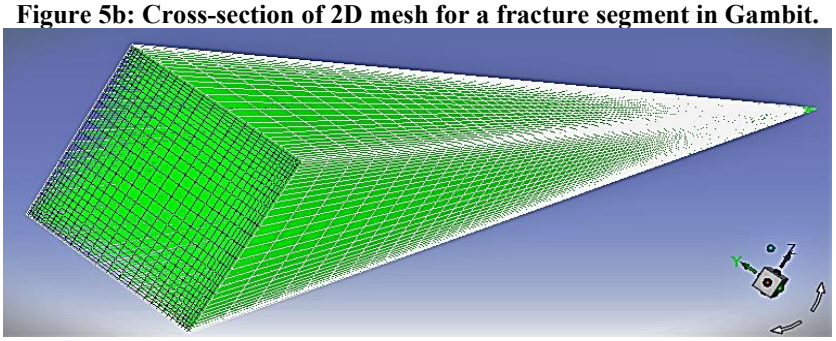


Figure 6: Cross-section of 3D mesh for a fracture segment in Gambit.

The grout, modeled as a two-phase fluid (water at 1000 kg/m³ and grout at densities of 1325, 1475, 1625, and 1725 kg/m³), was simulated using ANSYS Fluent.

The time-dependent viscosity functions (e.g.

μ_1 = exp (-16.00237+0.23127 t +0.0000758874 t2),
μ_2 = exp (-47.93616+1.03133 t -0.00477 t2),
μ_3 = exp (162.19485+6.84442 t -0.02162 t2+ 0.0000387585 t3-0.0000000248518 t4)

were derived from experimental rheological data. Tests were conducted using a rotational viscometer on grout samples with densities of 1325–1725 kg/m³. Viscosity measurements, recorded every 30 seconds over 15 minutes, were fitted to exponential polynomials using nonlinear regression in MATLAB, achieving a root-mean-square error (RMSE) of less than 0.05 Pa·s. These functions capture the rheopectic behavior, where viscosity increases over time due to cement hydration and particle interactions.

The flow was confirmed to be laminar (Reynolds number < 4000) using the equation:

$$RE=\frac{\rho VD}{\mu} \quad (2)$$

The initial properties and parameters of the fluid phase, including grout density, injection pressure, and viscosity models, are summarized in Table 1, providing a clear overview of the numerical simulation setup in Gambit and ANSYS Fluent.

In ANSYS Fluent, the Bingham rheology is implemented using the Herschel-Bulkley model with n=1, reducing to the Bingham model. The effective viscosity is defined as

$\mu_eff = (\tau_0 / \dot{\gamma}) + \mu_p$ for shear rates $\dot{\gamma} > \tau_0 / \mu_p$,

and $\mu_eff = \mu_0$ (a high constant) for $\dot{\gamma} \leq \tau_0 / \mu_p$

to avoid singularities at low shear rates. The yield stress τ_0, set to 5–20 Pa based on experimental data, is incorporated via a user-defined function (UDF) in C++ linked to the viscosity model. Time-dependent viscosity is updated at each time step using the exponential functions described above, capturing the evolving rheology during injection.

3.2. Assumptions

Key assumptions included laminar flow, spherical cement particles, negligible fracture roughness, and incompressible grout. No friction between grout and fracture walls was considered, simplifying the model to focus on viscosity and pressure effects.

The assumption of frictionless, smooth fracture walls simplifies the Navier-Stokes equations by eliminating wall shear stress terms, allowing focus on viscosity-driven flow resistance. This is justified for initial modeling in wide fractures (>1 mm), where viscous forces dominate, as supported by prior studies [15,16]. However, in narrower or rough fractures, friction could reduce penetration by 20–50%, as estimated from sensitivity analyses.

4. Results and Discussion

4.1. Viscosity and Density Effects

When cement grout is injected into rock mass fractures, the strong bonding forces between particles resist erosion due to dynamic water. The thickness of the grout deposit is significantly negatively correlated with hydrodynamic velocity. Additionally, the thickness of the grout deposit decreases with an increase in the water-to-cement ratio. An increase in the water-to-cement ratio reduces the concentration of the solid phase. Consequently, the plastic viscosity and ultimate shear force of the grout decrease. This notably reduces the contact force between the grout and the pipeline, thereby increasing the washout by moving water. Under the same hydrodynamic velocity, a reduction in pipe diameter increases the thickness of the grout deposit and can easily lead to pipe blockage. Conversely, in pipes with a larger diameter, a significant amount of deposited grout is washed away by dynamic water, intensifying the turbulent state of the dynamic water and preventing the deposition and accumulation of cement particles. The fluid processing has taken approximately five months, with the initial results and the specifications and parameters of the fluid phase presented in Tables 1 and 2.

Table 1: Initial Properties and Parameters of the Fluid Phas

First Phase (Water)				Second Phase(Grout)		
		Mixing of Two Fluids				
Density ρ(kg/m3)	Viscosity (kg/m.s)	Boundary Condition (Outlet)	Boundary Condition (Initial Velocity at Inlet) (m/s)	Density ρ(kg/m3)		Viscosity (kg/m.s)
998	0.0010	0	3.6848	1475	μ_1	15/77
998	0.0010	0	0.0001	1475	μ_2	46.91
998	0.0010	`0	0.0009	1725	μ_3	169/016
998	0.0010	0	0.0009	1475	μ_4	169/016
998	0.0010	0	0.0009	1325	μ_5	169/016
998	0.0010	0	0.0125	1475	μ_6	169/016

Table 2: Initial Processing Results of the Fluid Phase

Gravity (m/s2)	Densityρ(kg/m3)	Viscosity (kg/m.s)	Processing Time(min) (t)	Stopping PositionX (m)
0	1475	μ_1	2.16	0.48
0	1475	μ_2	2.16	0.87
0	1725	μ_3	11	0.52
0	1475	μ_4	13	0.78
0	1325	μ_5	11	0.38
0	1475	μ_6	1	0.26

Simulations revealed that increasing the water-to-cement ratio reduces grout viscosity, decreasing solid phase concentration and shear stress, which increases the risk of washout by dynamic water. Higher density (e.g., 1725 kg/m³) resulted in shorter setting times and reduced penetration, while lower density (e.g., 1325 kg/m³) extended penetration but increased washout risk. The viscosity-time relationship, depicted in Figure 7, shows an exponential increase in viscosity over time, with stopping times ranging from 2.16 to 11 minutes depending on density and viscosity. The density-time relationship (Figure 8) indicates that higher densities grouts (e.g., 1725 kg/m³) exhibit shorter stopping times due to faster setting, while lower density grouts (e.g., 1325 kg/m³) allow longer penetration. The displacement chart (Figure 9) illustrates the penetration length as a function of time, highlighting the impact of viscosity on stopping positions. The stopping position of grout due to density changes is shown in Figure 10, Finally, the stopping time and displacement chart (Figure 11) is also presented, which is thoroughly discussed In the following.

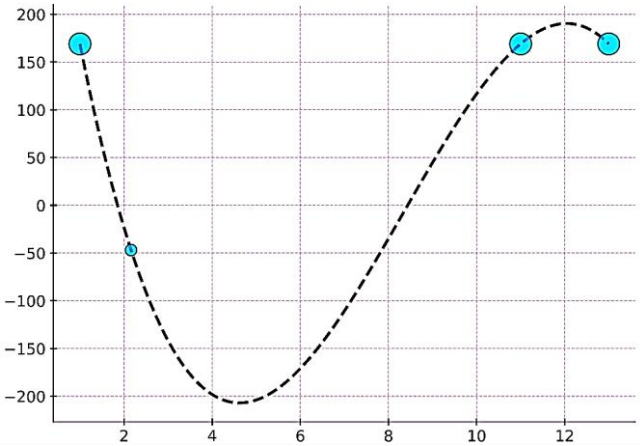


Figure 7: Viscosity-time chart showing exponential viscosity increase for different grout densities

The chart illustrates the relationship between grout stoppage time and changes in dynamic viscosity. The bubble chart plots stoppage time (T) in minutes on the horizontal axis and dynamic viscosity (μ) in kg/m·s on the vertical axis, which characterizes the grout's dynamic behavior, crucial for controlling the injection process and grout flow in rock fractures. Circular markers indicate viscosity data points, and a dashed curve shows the overall trend. The varying sizes of the bubbles represent the intensity of viscosity changes. At low stoppage times (1 and 2.16 minutes), viscosity is negative (-46.91), possibly indicating flow turbulence or localized effects. At 11 minutes, the grout exhibits more stable behavior and a denser composition. By 13 minutes, viscosity reaches a maximum positive value (169.01) and remains stable, indicating consistent grout composition under these conditions.

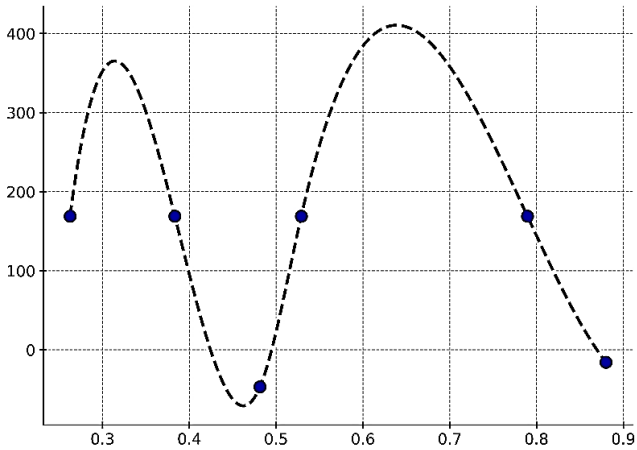


Figure 8: dynamic viscosity with position X.

The smoothed dashed curve in Figure 6 represents dynamic viscosity (μ) as a function of spatial position (X). Filled circular markers indicate measured data points, and the black dashed line shows the overall trend of changes. The horizontal axis represents spatial position in meters, and the vertical axis represents the dynamic viscosity of the fluid in kg/m·s. In this chart, data at lower positions (0.26 to 0.38 meters) show points with a viscosity of 169 kg/m·s, indicating very high resistance. Such behavior is observed when the grout composition is denser and has lower permeability, typically leading to rapid grout setting. At intermediate positions (0.48 and 0.52 meters), dynamic viscosity decreases and even reaches negative values, which may indicate complex flow behavior, turbulence, or significant changes in physical parameters. At the position of 0.87 meters, dynamic viscosity reaches its lowest value (46.91), which could indicate boundary effects or rapid fluid transfer at this position.

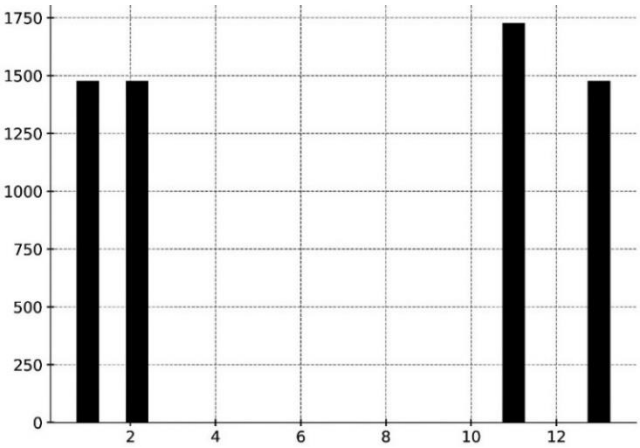


Figure 9: Density with Stopping Time.

The above chart examines the effect of different fluid densities as one of the most critical parameters influencing the stoppage threshold and grout movement within fractures, relative to processing time. Additionally, some variations and the impact of different fluid densities are influenced by processing time.

The bar chart illustrates density versus grout stoppage time within fractures, with density as a function of stoppage time. Black bars represent measured data points. The horizontal axis represents time in minutes, and the vertical axis represents grout density in kg/m³, indicating the grout's resistance to permeability and its stability.

At low stoppage times (1 and 2.16 minutes), the density is 1475 kg/m³, indicating a stable grout composition. At a stoppage time of 11 minutes, density varies significantly between its maximum and minimum values (1725 and 1325 kg/m³), suggesting notable changes due to localized effects or variations in the water-to-cement ratio. At a stoppage time of 13 minutes, the fluid density is 1475 kg/m³, indicating a more stable grout composition.

The next chart shows variations in fluid density relative to the grout's stoppage position, representing the maximum penetration length of the fluid for that grout viscosity. The chart below clearly illustrates the variations and impact of different fluid densities and their respective stoppage positions.

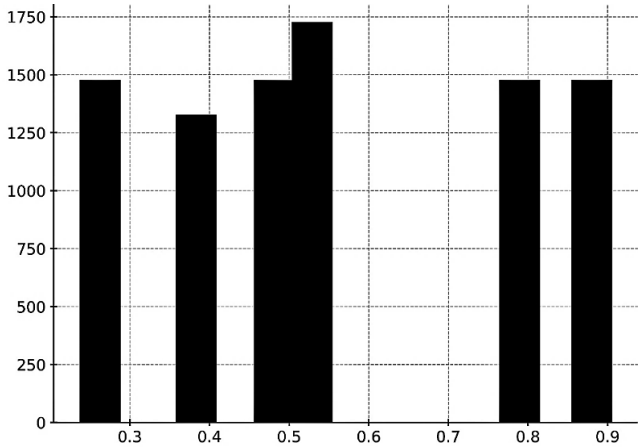


Figure 10.: Bar Plot of Density with X.

The above figure is a bar chart of density versus displacement, as a function of spatial position and grout stoppage points.

The horizontal axis of the chart represents spatial position in meters, and the vertical axis represents density in kg/m³.

The bar chart illustrates density (ρ) as a function of spatial position (X). Black bars represent measured data points, providing a clear and professional engineering visualization.

At positions 0.26, 0.38, and 0.48 meters, the grout density is 1475 kg/m³, indicating a uniform and stable composition at these positions. At position 0.52 meters, the grout density reaches its maximum value of 1725 kg/m³, suggesting a denser composition and a lower water-to-cement ratio. At position 0.38 meters, the grout density is at its lowest value of 1325 kg/m³, which may result from a high water-to-cement ratio, other influencing factors, localized effects, or a heterogeneous composition.

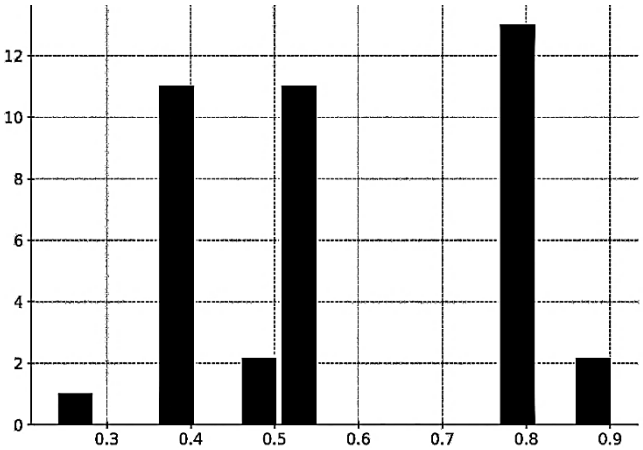


Figure 10: Stopping Time with X Position.

The figure is a bar chart of stoppage time (T) as a function of spatial position (X).

The horizontal axis represents displacement (X) in meters, and the vertical axis represents time (T) in minutes. At positions 0.26 and 0.38 meters, stoppage times of 1 and 2.16 minutes are recorded, indicating easier grout penetration. At positions 0.48 and 0.52 meters, the stoppage time increases to 11 minutes, suggesting greater resistance and fluidity compared to the previous positions. At position 0.79 meters, the longest stoppage time of 13 minutes is recorded, clearly indicating higher stability of the grout composition at this point. Additionally, at position 0.87 meters, the stoppage time decreases again to 2.16 minutes, indicating higher permeability conditions at this point.

4.2. Injection Pressure and Penetration

A constant injection pressure of 0.01 bar, applied gradually, improved grout penetration compared to sudden pressure increases, which led to filter cake formation and reduced penetration. The pressure equation used was:

$$P_g=P_{mg}+P_{hg}-P_{hgw}-(f_{cg}+f_{pg}) \quad (3)$$

where Pg is the injection pressure, and terms account for manometric pressure, hydrostatic pressure, and losses.

The following section presents a sample simulation depicting the flow of grout fluid within the borehole until it reaches the rock joints (Figure 13). Additionally, the subsequent figure illustrates the stopping point of the fluid within the joint—governed by the grout's viscosity and density—which represents the maximum penetration length for one of the grout mixture samples (Figure 14).

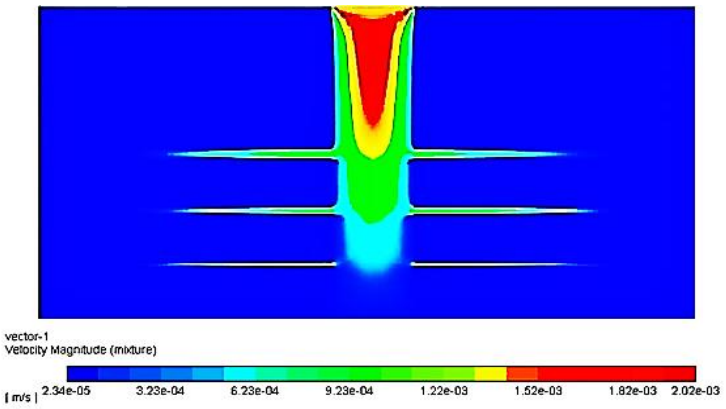


Figure 11: Fluid motion in the borehole and penetration into fractures during injection.

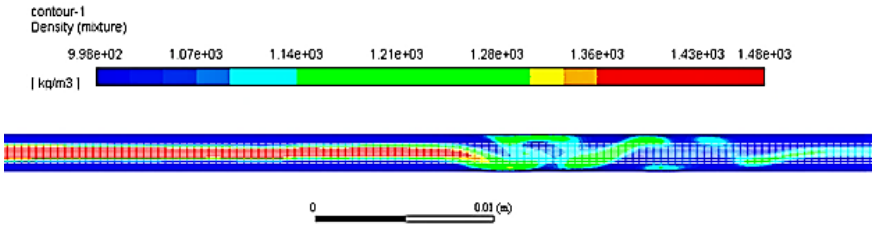


Figure 12: Stopping position of grout in the fracture due to viscosity changes.

4.3. Simulation Outcomes

The 2D and 3D models provided detailed insights into phase separation and grout behavior. The 3D model better captured phase segregation near stopping points, where viscosity peaked, leading to grout setting (Figure 14). The 3D model provided enhanced visualization of grout motion, as seen in Figures 15 (front view) and 16 (side view).

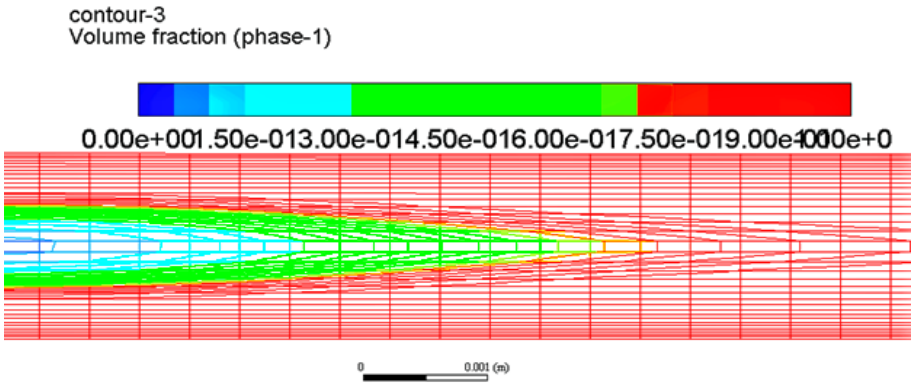


Figure 13: Phase separation of grout and water during motion near the stopping point.

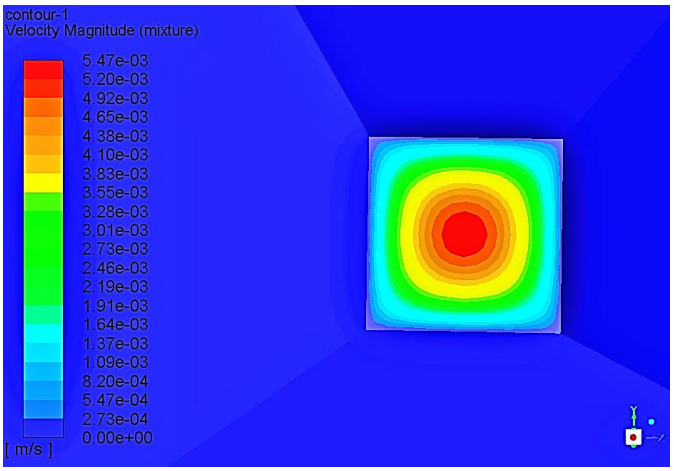


Figure 14: 3D model of grout motion in the fracture (front view).

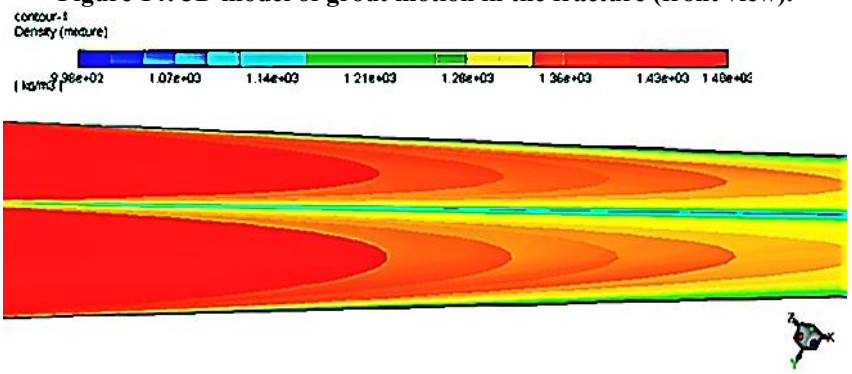


Figure 15: 3D model of grout motion in the fracture (side view).

5. Conclusion

This study comprehensively investigated the influence of time-dependent viscosity on cement grout penetration in rock fractures, demonstrating its critical role in improving the stability and impermeability of underground structures, such as tunnels and dams.

Through analytical modeling based on Newton's second law and numerical simulations using Gambit and ANSYS Fluent, grouts with density of 1325, 1475, 1625, and 1725 kg/m³ have been analyzed. It has been demonstrated that higher water-to-cement ratios reduce viscosity, increasing washout risks, while higher density accelerates setting, limiting penetration but improving stability. A gradual 0.01-bar injection pressure has been shown to optimize penetration by reducing filter cake formation, with stoppage times of 1–13 minutes governed by viscosity and density. The Bingham model, supported by Navier-Stokes equations, has been validated as an accurate descriptor of grout rheology. These findings provide a robust framework for optimizing grouting parameters, offering practical solutions for water seepage control in underground engineering. Further research is recommended to account for fracture roughness and dynamic water flow to enhance model applicability in complex geological environments.

Statements and Declarations

The authors declare that they have no conflict of interest.

Competing Interests

This research work is not supported by any funding agency.

Financial Disclosure Statement

The author(s) received no specific funding for this work.

Funding

This research did not receive any specific grant from funding agencies in the public,

commercial, or not-for-profit sectors.

Data Availability

The data presented in this study are available on request from the corresponding author

Consent for Publication

All the authors have read and agreed to the submitted version of the manuscript

References

1. Li, S., et al., Protection against water or mud inrush in tunnels by grouting: a review. Journal of Rock Mechanics and Geotechnical Engineering, 2016. 8(5): p. 753–766. https://doi: 10.1016/j.jrmge.2016.05.002.
2. Berigny, C., Historical development of grouting techniques for underwater structures. Journal of Civil Engineering History, 1802.
3. Axelsson, M., G. Gustafson, and Å. Fransson, Stop mechanism for cementitious grouts at different water-to-cement ratios. Tunnelling and Underground Space Technology, 2009. 24(4): p. 390–397.
4. Gothäll, R. and H. Stille, Fracture dilation during grouting. Tunnelling and underground space technology, 2009. 24(2): p. 126–135.
5. Rafi, J.Y. and H. Stille, Basic mechanism of elastic jacking and impact of fracture aperture change on grout spread, transmissivity and penetrability. Tunnelling and Underground Space Technology, 2015. 49: p. 174–187.
6. Mohammed, M.H., R. Pusch, and S. Knutsson, Study of cement-grout penetration into fractures under static and oscillatory conditions. Tunnelling and Underground Space Technology, 2015. 45: p. 10–19.
7. Sui, W., et al., Experimental investigation on sealing efficiency of chemical grouting in rock fracture with flowing water. Tunnelling and Underground Space Technology, 2015. 50: p. 239–249.
8. Ruan, W.J., Analytical model for grout transport in fractured media with time-dependent viscosity. Journal of Geotechnical Engineering, 2007. 133(8): p. 987–995.
9. Sonebi, M., Experimental study on cement grouts with viscosity-modifying additives. Materials and Structures, 2008. 41(2): p. 255–267. https://doi: 10.1016/j.cemconres.2006.05.016.
10. Şahmaran, M., et al., Use of natural zeolite in cement-based grouts for improved rheology. Cement and Concrete Composites, 2010. 32(6): p. 444–452. https://doi: 10.1016/j.cemconres.2008.03.007
11. Quinn, P., et al., Numerical modeling of time-dependent viscosity in cement grouts using OpenFOAM. Computers and Geotechnics, 2012. 45: p. 67–75.
12. Karol, R.H., Chemical grouting and soil stabilization. CRC Press, 2003. https://doi: 10.1201/9780203911815.
13. Li, S., et al., Apparent viscosity of cement grouts with varying water-to-cement ratios. Construction and Building Materials, 2014. 69: p. 232–239.
14. Assaad, J.J., Real-time viscosity monitoring of cement-based grouts. Journal of Materials in Civil Engineering, 2016. 28(3): p. 04015155. https://doi: 10.1016/j.conbuildmat.2014.12.024.
15. Gustafson, G., et al., Grout penetration and sealing in fractured rock. Geotechnical Engineering Journal, 2001. 134(7): p. 897–905.
16. Eftekhari, A., Aalianvari, A. and Rostami, J., 2018. Influence of TBM operational parameters on optimized penetration rate in schistose rocks, a case study: Golab tunnel Lot-1, Iran. Computers and Concrete, An International Journal, 22(2), pp.239-248.https://doi.org/10.12989/cac.2018.22.2.239
17. Hanson, B.D., Effect of water-to-cement ratio on grout permeability: Filter pump tests. Geotechnical Testing Journal, 2009. 32(4): p. 321–329.
18. Eriksson, M., et al., Permeability assessment of cement grouts using permeameter tests. Tunnelling and Underground Space Technology, 2011. 26(2): p. 245–253.
19. Eklund, D., Stille, H., Permeability of cementitious grouts in rock fractures. International Journal of Rock Mechanics and Mining Sciences, 2008. 45(4): p. 565–573.
20. Samiei, S. and Aalianvari, A., 2025. A Hybrid AHP-AI Framework for Assessing

and Mitigating Tunneling Impacts on Confined Spring Discharge. Journal of Hydraulic Structures, pp.179-189. Doi: 10.22055/jhs.2025.49054.1338
21. Nonveiller, E., Grouting: Theory and practice. Elsevier, 1989.
22. Houlsby, A.C., Construction and design of cement grouting: A guide to grouting in rock foundations. Wiley-Interscience, 1990.
23. Bruce, D.A., Specialty geotechnical construction techniques. Geo-Institute of ASCE, 2004.
24. Lombardi, G., The role of cohesion in cement grouting of rock. International Journal of Rock Mechanics and Mining Sciences, 2003. 40(3): p. 321–331.
25. Nazari, M.H., Aalianvari, A. and Tani, M.E., 2025. Contrary trends of grout consumption and water absorption at Sardasht. Scientific Reports, 15(1), p.4667. https://doi.org/10.1038/s41598-025-87884

© 2025 by the authors. Licensee SCU, Ahvaz, Iran. This article is an open access article distributed under the terms and conditions of the Creative Commons Attribution 4.0 International (CC BY 4.0 license) (http://creativecommons.org/licenses/by/4.0/).

Machine Learning and Statistical Analysis of Measured Velocities by ADV of Free Surface Vortices at Intakes

Hamid Ahani[1], Saeed Reza Khodashenas[*,1] ,Hamed Sarkardeh[2]

1. Department of Water Science and Engineering, Agriculture Faculty, Ferdowsi University of Mashhad, Mashhad, Iran.
2. Department of Civil Engineering, Hakim Sabzevari University, Sabzevar, Iran.

***Corresponding Author:**
Saeed Reza Khodashenas,

Email: khodashenas@um.ac.ir
Received: 2025.11.18
Accepted: 2026.01.01
J. Hydraul. Struct., 12(3):54-69
DOI: 10.22055/jhs.2026.50962.1367

ABSTRACT

Free surface vortices in hydraulic intakes can lead to air entrainment, vibrations, and energy loss. This study aimed to optimize an Acoustic Doppler Velocimeter (ADV) for measuring tangential velocities in vortices. The used statistical methods include calculating the median, mode, and arithmetic mean without outlier removal; and removing outliers using truncated mean, Z-Score, box plot, histogram, and a two-standard deviation range. The employed machine learning models were Isolation Forest, One-Class SVM (Support Vector Machines), and DBSCAN (Density-Based Spatial Clustering of Applications with Noise). Experiments were conducted at Fr = 0.85, 1, and 1.27. In order to determine the data acquisition duration, a long-term experiment was conducted, and based on the output graph, 30 seconds was determined as the appropriate time. The results showed that the mean and median at all Fr provided smooth and physical profiles, while the mode method produced unrealistic fluctuations due to the multimodal nature of the data. The outlier removal methods produced almost overlapping profiles with an RMS deviation of less than 1.5%, indicating the stability of these methods and the appropriate quality of the ADV data. Among the machine learning methods, the Isolation Forest algorithm provided the most accurate and stable results, and its behavior was most consistent with valid statistical methods. Comparison of the results with the Rankine model also showed that the measured velocity profile accurately reproduces the linear growth of the velocity in the core and the drop in the outer regions of the vortex. Overall, this research shows that combining ADV data with robust data processing methods specifically, trimmed mean, Z-score, and Isolation Forest significantly increases the accuracy and reliability of eddy velocity profile determination and can be used in the analysis and design of eddy control systems in reservoirs.

KEYWORDS

Free-surface vortex, ADV device, Statistical analysis, Tangential velocity, Inlet intake.

1. Introduction

Vortices are a common occurrence in both natural and industrial systems on a wide range of scales. Free-surface vortices, in particular, are often observed at the intakes of hydropower plants. Free surface vortices form at the water surface and extend down into the intake [1]. The primary factors contributing to vortex formation include changes in boundary direction, non-uniform velocity distribution, and asymmetric flow near the intake [2].

A vortex is a vector quantity, ω, that locally quantifies the rotation of a fluid particle around its center of mass. Mathematically, it is defined as the curl of the velocity vector: $\omega = \nabla \times V$. Vortex flow is typically described using a local cylindrical coordinate system (r, θ, z), where z extends downward from the free surface along the vortex central axis. The corresponding velocities are radial, tangential, and axial, denoted as V_r, V_θ and V_z [1]. Vortices formed in hydraulic intakes are categorized into two types of surface and subsurface vortices. According to the Rankine vortex model [3], surface vortices are further divided into two kinds of forced and free vortex. In a forced vortex, V_θ increases linearly with the distance from the vortex center. Conversely, in a free vortex, V_θ is inversely proportional to this distance [2]. There are two well-known classification systems for vortices that form on the water surface. Hecker [4] physically divided vortices into six types. In a different classification, Sarkardeh et al. [5] categorized them into three classes A, B and C based on their significance and risk level. Table 1 shows the relationship between these two classification systems and the physical and visual characteristics of the vortices.

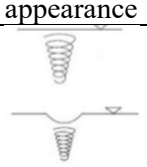
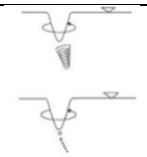
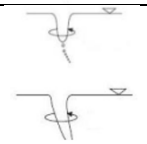
Formation of Surface vortices are an undesirable phenomenon in hydraulic intakes because they lead to air entrainment, vibration, and energy loss [2]. The vortices that form at the intake are a composite model of both forced and free vortices [3]. The strength of a vortex is calculated by its V_θ in the free vortex region, which is obtained from Equation (1) [6].

$$\Gamma = 2\pi r V_\theta \quad (1)$$

In Equation (1), r is the radial distance from the vortex center. Vortex strength (Γ) is a crucial factor for predicting vortex behavior, and it depends on the reservoir geometry, the intake Froude number (Fr), and the relative submergence (S/D) [7]. Understanding the vortex mechanism in hydraulic intakes requires a thorough investigation of the flow velocity.

To analyze a vortex, it is crucial to obtain orthogonal velocities, as vorticity is defined as the curl of the velocity, and orthogonal velocities allow for the precise calculation of local rotation. Velocity measurement methods include Particle Image Velocimetry (PIV) for 2D or 3D velocity fields, Laser Doppler Velocimetry (LDV) for local velocity, and ADV for 3D velocity. The ADV is a device that records velocity fluctuations in three perpendicular directions over a specific range and

Table 1. Vortex types and classes [5]

Vortex type	Definition [4]	Classification [5]	Physical appearance
1	Coherent surface swirl	Class C	
2	Surface dimple; coherent swirl at surface		
3	Dye core; coherent swirl through water column	Class B	
4	Vortex pulling floating trash but no air		
5	Vortex pulling air bubbles into the intake	Class A	
6	Full air core to the intake		

processes them with its software. The ADV velocity measurement is based on the Doppler principle, where it sends out sound waves at a specific frequency and receives their reflections. The frequency difference is proportional to the flow velocity. This device measures velocity at a point 5 cm below the transmitting sensor. Key parameters include the correlation factor (R^2) and the Signal-to-Noise Ratio (SNR). The correlation factor can be considered a quality parameter for the measured data and is recommended to be in the 70% to 100% range. Since the ADV velocity measurement is based on the Doppler principle, a short sound pulse with a known frequency is first sent vertically. The reflection of sound from the water is then received by three small probes, amplified by a converter, and analyzed by the device's processor card. The change in frequency between the transmitted and received pulses is a result of the water's flow velocity. To ensure proper device function, the reflected sound must be strong enough for the device to calculate the resulting frequency change. The strength of the return sound is represented by the signal-to-noise ratio. An SNR of at least 5 dB is recommended for data acquisition [8]. The ADV is used in hydraulic laboratories to measure 3D velocities, velocity profiles, and Reynolds stresses.

Early investigations on free surface vortices primarily focused on their symmetric behavior. Sarkardeh et al. [5] showed that vortex strength decreases as the intake wall becomes more vertical, while Camnasio et al. [9] linked reservoir geometry to flow patterns using ultrasonic profiling. Following this, Sarkardeh et al. [10] measured the flow field in a reservoir with a free-surface vortex using an ADV, graphically presenting their findings. With advances in experimental techniques, research shifted toward understanding the 3D and frequently asymmetric nature of vortices. PIV and high-speed particle image velocimetry (HSPIV) measurements by Suerich-Gulick et al. [1], Mulligan et al. [11], Naderi and Gaskin [12], and Naderi et al. [13] demonstrated the strong influence of approach flow on vortex asymmetry. More recent studies refined this understanding: Duinmeijer et al. [14] quantified axial flow transport in the vortex core, and Hamidi et al. [15] mapped 3D particle trajectories for different vortex classes. Alongside improved understanding of vortex mechanisms, numerous works have focused on mitigation and hydraulic control. These include circulation zone analysis near intakes [16], performance of anti-vortex plates [17], the effect of intake angle and sediment transport [18,19,20], and development of new suppression methods [21,22]. Taghizadeh et al. [23] provided a comprehensive review of the most recent vortex-formation mechanisms, highlighting the multi-factor and highly unsteady nature of intake vortices. Newer experimental studies have also expanded the understanding of vortex induced instability: Amini et al. [24] numerically examined vortex behavior under variable temperature fields; Zhang et al. [25] characterized vortex evolution and pressure fluctuations in pump sumps; Jiao et al. [26] analyzed suction vortex formation governed by clearance and inflow conditions; and Mondal et al. [27] experimentally captured air entrainment stages during free surface vortex development. Collectively, these recent findings emphasize that accurate, high-resolution velocity field measurement is crucial for understanding vortex dynamics. Given this need, the ADV has become a common tool for vortex studies. However, ADV generates large volumes of instantaneous, noisy, and highly fluctuating velocity data, which must be filtered using signal quality metrics such as SNR and R^2 before identifying a representative velocity value suitable for hydraulic interpretation. Traditional statistical filtering methods are often insufficient for fully removing outliers under strongly unsteady vortex conditions.

In parallel, recent developments show that machine learning is increasingly effective in analyzing complex hydraulic data. Roushangar et al. [28] successfully modeled energy dissipation over stepped

spillways; Ghorbani et al. [29,30] predicted discharge coefficients and suspended sediment concentration with ML models; Salmasi and Abraham [31] used hybrid ML methods to estimate inclined-gate discharge; and Salmasi et al. [32] demonstrated the superior performance of models such as RF, GEP, MARS, and M5P in predicting scour depth. These studies collectively highlight the capability of ML to extract reliable information from noisy, nonlinear hydraulic signals similar to ADV datasets recorded under vortex flow. The novelty of the present study lies in conducting, for the first time, a systematic comparison between statistical and ML based outlier removal approaches to improve ADV velocity data quality under vortex flow conditions. The objective is to determine the most reliable method for extracting representative 3D velocities, thereby enhancing the accuracy of vortex flow characterization.

2. Materials and Methods

Tests were performed in a rectangular reservoir with transparent walls, measuring 0.7 m in length, 0.6 m in width, and 0.7 m in height. A vertical intake with a 0.04 m diameter opening was used. To enable the observation of stronger vortices and minimize scaling effects, the distance from the center of the intake to the side walls was set to at least 4D (where D is the diameter of the intake pipe), as recommended by Anwar et al. [33]. To stabilize the incoming flow, two perforated plates were installed in the flow path. This flow conditioner not only eliminated water fluctuations but also ensured a uniform flow into the reservoir, allowing for the use of the maximum reservoir space. By selecting a closed-loop water circuit and using a variable-speed electric pump with adequate power, it was possible to generate strong vortices and control various flow rates at the intake and set the water surface at a fixed intake submergence (S). A flow meter was used to measure the volumetric flow rate of the water, with an accuracy of 0.01 L/s. Additionally, a scale with an accuracy of ±1 mm was installed on the reservoir wall to read the intake's submergence depth. Figure 1 shows a schematic view of the experimental setup.

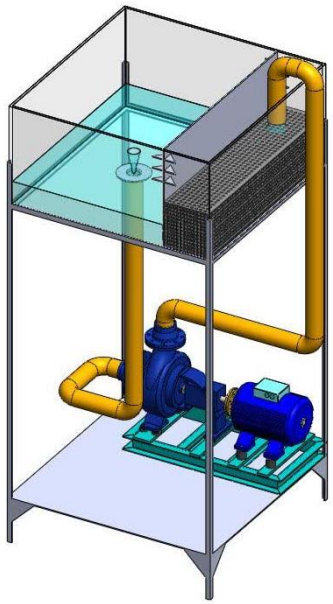


Figure 1. A Schematic view of the experimental setup

The experimental conditions were as follows: three tests were conducted with a constant relative submergence depth (S/D) of 3.25 and a constant data acquisition depth (Z) of 1.25 D, under three different Froude numbers (Fr = 0.85, 1, and 1.27). For measuring instantaneous velocities, a Nortek Vectrino ADV with four down-looking probes was used, capable of recording 3D velocity components. The device frequency was set to 25 Hz. The number of valid data points was not constant and could be reduced due to limitations such as a signal-to-noise ratio (SNR) below 5 dB or correlation coefficient (R^2, COR) below 70%. The raw data were filtered and validated using WinADV software to remove possible spikes and noise. To analyze the instantaneous velocity data obtained by the ADV and achieve reliable velocity values for flow analysis, a set of statistical and machine learning methods was applied. These analyses were divided into three categories: analysis using all data, analysis with outlier removal, and analysis using machine learning methods for outlier detection.

2.1. Statistical Analysis Using All Data

In this step, the statistical measures were calculated without removing any data. Median index which is the middle value of the data after it has been sorted in ascending order. This measure is robust against outliers and represents the center of the data distribution without being influenced by extreme values. Mode index which is the value that appears most frequently in the dataset. This measure is useful for identifying the dominant or recurring velocities in the flow and can indicate stable patterns in the instantaneous data. Arithmetic Mean (avg) index which is calculated as the sum of all data points divided by the total number of points. This is the simplest measure of central tendency but is sensitive to outliers, which can result in an over- or underestimated value in the presence of noise.

$$avg = \frac{\sum x_i}{n} \quad (2)$$

2.2. Statistical Analysis with Outlier Removal

To improve accuracy and eliminate the effect of noise or invalid data (e.g., spikes from acoustic interference or suspended particles), various methods were applied to identify and remove outliers. After their removal, the arithmetic mean was calculated from the remaining data. The following methods used were employed. Trimmed Mean (avg 8%): In this method, the data was sorted in ascending order, and the top and bottom 4% of the data were considered outliers. The arithmetic mean was then calculated from the remaining 92% of the data. This is a simple and effective method for reducing the effect of outliers without complex calculations. Z-Score: The Z-Score method identifies outliers based on their standard distance from the mean. The Z-Score for each data point x is calculated as:

$$z = \frac{x - \mu}{\sigma} \quad (3)$$

where μ is the mean of all data and σ is the standard deviation. Data points with an absolute Z-Score greater than 3 ($|Z| > 3$) were identified and removed as outliers. The arithmetic mean was then calculated from the remaining data. This method assumes a normal distribution, making it suitable for velocity data, which often follows a normal distribution. Box Plot: In a box plot, outliers are identified using the Interquartile Range (IQR). First, the first quartile (Q1, the 25th percentile) and the third quartile (Q3, the 75th percentile) are calculated, and then the IQR is determined by

$$IQR = Q3 - Q1 \quad (4)$$

Data points less than Q1 - 1.5 × IQR or

greater than Q3 + 1.5 × IQR are considered outliers. After removing these points, the arithmetic mean is calculated from the remaining data. This method is visual and non-parametric, making it useful for skewed distributions. Histogram: In a histogram, data is divided into bins, and the frequency of each bin is plotted. Outliers are typically identified at the tails of the distribution or in bins with very low frequency, as these points are far from the main distribution (e.g., a normal peak). After identifying and removing these outliers (either through visual inspection or a frequency threshold), the arithmetic mean is calculated from the remaining data. This method is effective for detecting distribution patterns. Standard Deviation Range (2 σ): The standard deviation (σ) is a measure of data dispersion around the mean and is calculated as:

$$\sigma = \frac{\sum(x_i - \mu)^2}{n} \quad (5)$$

In this method, for each data point, a range from (μ - 2σ) to (μ + 2σ) was considered. This range covers approximately 95% of a normal distribution. The arithmetic mean was then calculated only from the data within this range, eliminating the effect of outliers outside of it.

2.3. Machine Learning Methods for Outlier Detection

For more accurate outlier detection, especially in complex data with high noise, three machine learning models were applied. Each model identified the outliers, and the arithmetic mean was then calculated from the non-outlier data.

Isolation Forest: This algorithm is a decision tree-based method designed for outlier detection. It isolates data points through random partitioning and calculates the path length h(x) for each point x until it reaches a leaf node. Points that are isolated earlier (i.e., those with a lower average path length E (h(x)) are identified as outliers, as they are less connected to the main data groups. The anomaly score for each point is computed using the following formula:

$$s(x,n) = 2^{-\frac{E\,(h\,(x)\,)}{c\,(n)}} \quad (6)$$

where:

$$c\,(n) = 2H\,(n-1) - \frac{2\,(n-1)}{n} \quad (7)$$

represents the average path length in a random binary tree with n samples, and $H(i) \approx \ln(i) + 0.577$ (0.577 is the Euler-Mascheroni constant) is the harmonic number function. The symbols used in the equations are defined as follows: $s(x,n)$: Anomaly score for a point x given n samples, ranging from 0 to 1, where values close to 1 indicate outliers and values close to 0.5 suggest normal data. $h(x)$: Path length of point x, representing the number of nodes traversed in a decision tree until reaching a leaf. $E(h(x))$: Expected path length of point x, averaged over multiple trees. $c(n)$: Average path length for a random binary tree with n samples, used as a normalization factor. n: Total number of samples in the dataset. x: A data point in the dataset. i: Index variable used in the harmonic number calculation [34].

The parameter contamination (estimated outlier ratio, e.g., 0.1) is used to adjust the method's sensitivity. After removing the outliers, the mean is calculated from the remaining data. This method is suitable for large datasets and does not require a specific data distribution assumption.

One-Class SVM: This model is an unsupervised learning algorithm that learns the boundaries of normal data using the Support Vector Machine approach and identifies points outside these boundaries as outliers. The decision function for this model is defined as follows:

$$f(x) = sign\left(\sum_{i=1}^{n} \alpha_i\, k\,(x, x_i) - \rho\right) \quad (8)$$

Where $k(x, x_i)$ is the kernel function (typically the Gaussian kernel $\exp(-\Upsilon\|x - x_i\|^2)$, α_i are the Lagrange coefficients for support vectors, and ρ is the bias term

determining the decision boundary. The algorithm operates by solving the following optimization problem:

$$\min_{\omega,\xi,\rho} \frac{1}{2}\| \omega \|^2 + \frac{1}{\upsilon\, n}\sum_{i=1}^{n}\xi_i - \rho \quad (9)$$

subject to the constraint:

$$\left(\omega, \varphi(x_i)\right) \geq \rho - \xi_i, \quad \xi_i \geq 0, \quad i = 1, \ldots, n \quad (10)$$

where ω is the weight vector in the feature space, $\varphi(x_i)$ is the mapping of data points to the feature space, υ is a parameter controlling the proportion of outliers (typically between 0 and 1, e.g., 0.1), ξ_i are slack variables for points outside the boundary, and n is the total number of samples [35].

The model assumes that most data points are normal and detects outliers based on their distance from the distribution center. After removing the outliers, the arithmetic mean is calculated from the remaining data. This method is ideal for discrete, unclassified data such as velocities measured by ADV.

DBSCAN (Density-Based Spatial Clustering of Applications with Noise): This algorithm is a density-based clustering method that groups points based on proximity and a minimum number of neighbors (min_samples, e.g., 5). A point x is considered a core point if the number of points within its ε-neighborhood (e.g., ε = 1. 5) is at least min_samples, as defined by:

$$| N_\varepsilon(x) | \geq \min_samples \quad (11)$$

where:

$$N_\varepsilon(x) = \{x' \in D | \, dist(x, \acute{x}) \leq \varepsilon\} \quad (12)$$

is the set of points within the ε-neighborhood of x, and

$$dist(x, x') = \sqrt{\sum_{i=1}^{d}(x_i - x'_i)^2} \quad (13)$$

is the Euclidean distance between points x and x', with d representing the data dimensionality and x_i and x'_i the coordinates of x and x', respectively. Points that do not belong to any cluster or have low density (i.e., $N_\varepsilon(x)$ < min_samples) are identified as noise or outliers [36]. After removing these points, the mean is calculated from the data within the clusters. This method is suitable for data with irregular distributions and does not require a pre-determined number of clusters.

3. Results and Discussion

Figure 2 shows a picture of the formed vortices of Type A and B in the present experimental study.



Fr = 1.27 **Fr = 1** **Fr = 0.85**

Figure 2. Formed air-core vortex in the experimental model

To determine the optimal sampling duration, a long-term experiment of 600 seconds was conducted at a fixed point. This experiment resulted in the collection of approximately 15,000 instantaneous velocity data points. Figure 3 presents the distribution of these velocity values against their frequency of occurrence, illustrating the repetition rate of the recorded instantaneous velocities.

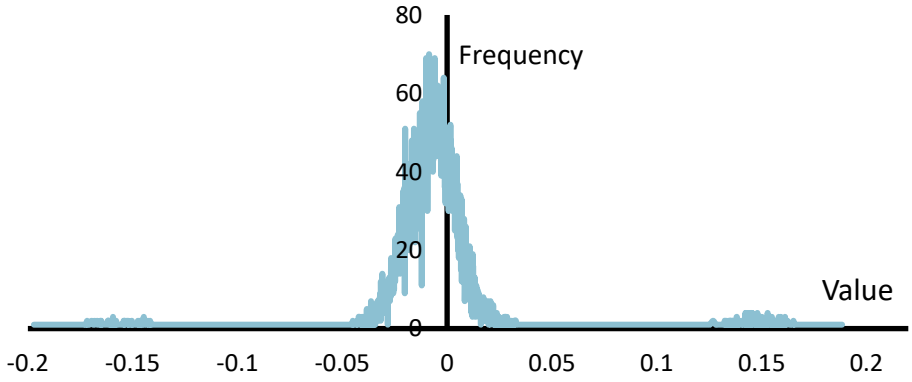


Figure 3. Distribution of instantaneous velocity values versus their frequency of occurrence

To identify the optimal sampling duration, the collected data were analyzed cumulatively over time intervals of 10, 20, 30, … up to 600 seconds. Figure 4 illustrates the variations of tangential velocity (V_θ) using different statistical methods and machine learning algorithms. The results indicate that significant fluctuations occur during the initial stage of the experiment, particularly within the first 30 seconds. However, after approximately 30 seconds, most methods exhibit a stable pattern, and the velocity variations become minimal. This trend is confirmed by the convergence of statistical approaches (mean, median, mode, and others) as well as machine learning methods (Isolation Forest, One-Class SVM, and DBSCAN). In other words, the agreement among these different approaches beyond this duration confirms the stabilization of the velocity trend. Accordingly, it can be concluded that a 30-second sampling interval is sufficient for reliable data acquisition using the Acoustic

Doppler Velocimeter (ADV). Within this duration, approximately 750 instantaneous velocity data points are collected, although the final number may be reduced due to the applied filters. This choice ensures that the collected data are statistically reliable while avoiding unnecessarily long sampling times.

Based on the analytical Rankine vortex model, vortices that form at the intake are a composite of two regions of a forced vortex (rotational) and a free vortex (irrotational). In the forced vortex region, V_θ increases linearly with the distance from the center of rotation. In contrast, in the free vortex region, the magnitude of V_θ is inversely proportional to the distance from the center. The boundary between these two regions is approximately at a distance equal to the radius of the intake from the axis of rotation [3]. Figure 5 shows the tangential velocity distribution profile based on the Rankine model.

Figures 6 to 8 show the results of statistical analyses performed on the radial cross section of the vortex obtained from the present experimental study at Fr = 0.85, 1.0 and 1.27 and with three states statistical analysis using all data, statistical analysis with outlier removal, and machine learning methods for outlier detection.

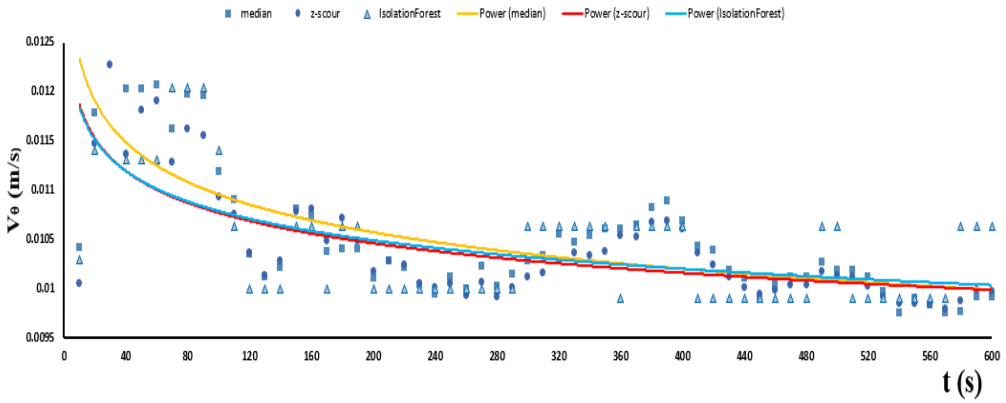


Figure 4. Statistical Analysis of Velocity Components (V_θ) Across Various Sampling Durations Using Statistical and Machine Learning Methods

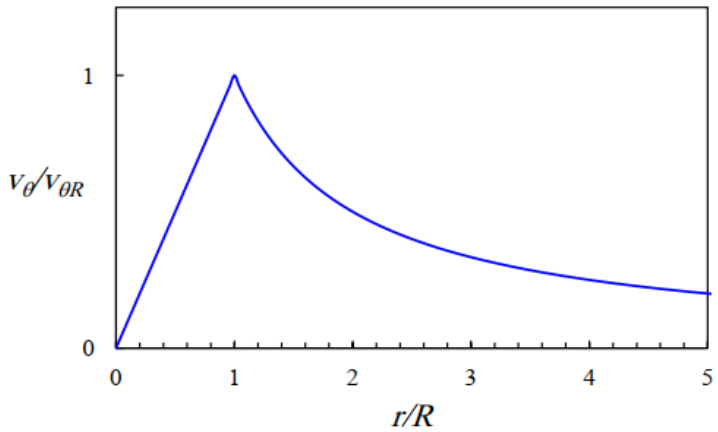


Figure 5. Tangential velocity distribution profile based on the Rankine model

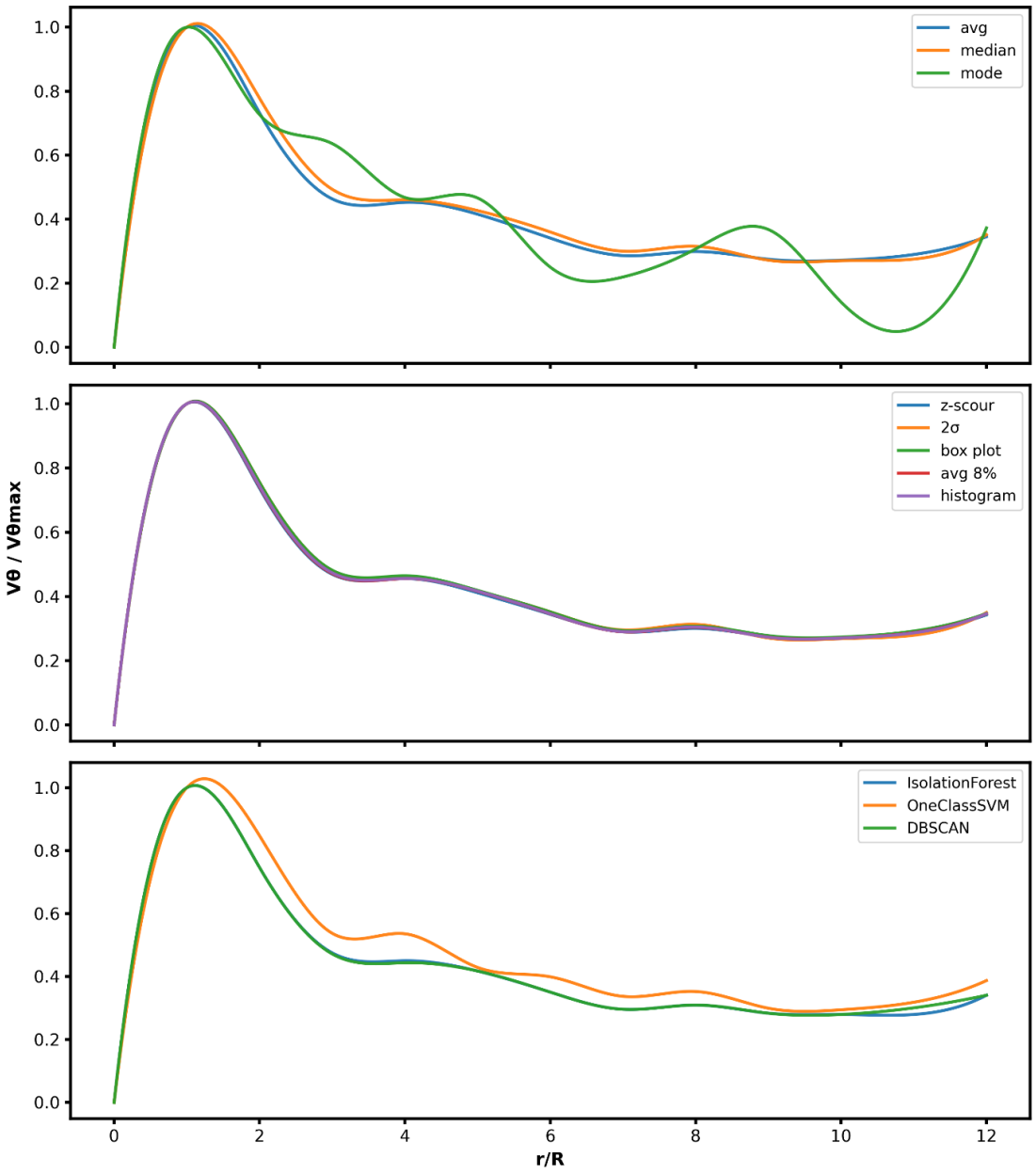


Figure 6. The statistical analyses conducted on a radial cross-section of the vortex for Fr = 0.85

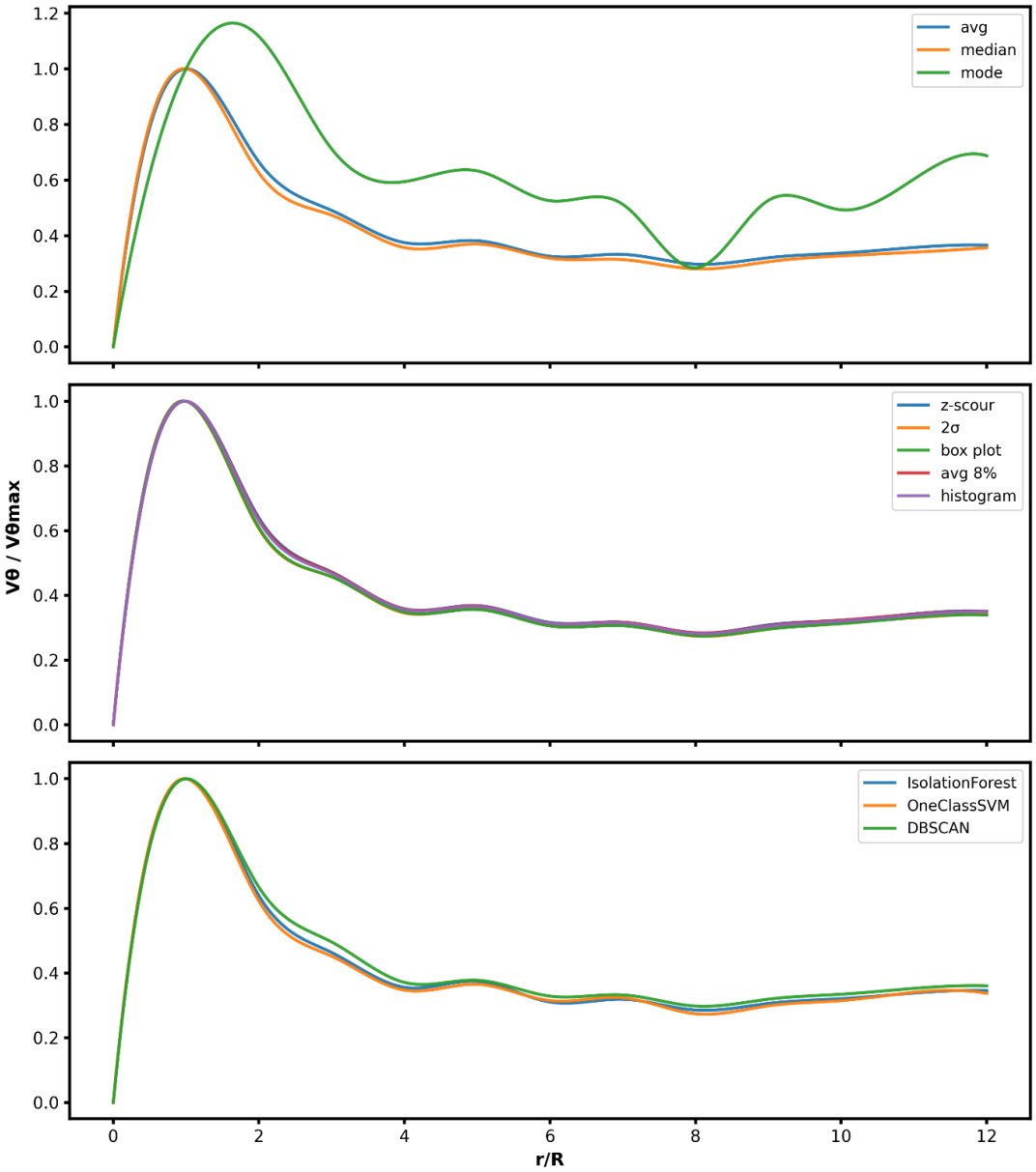


Figure 7. The statistical analyses conducted on a radial cross-section of the vortex for Fr = 1

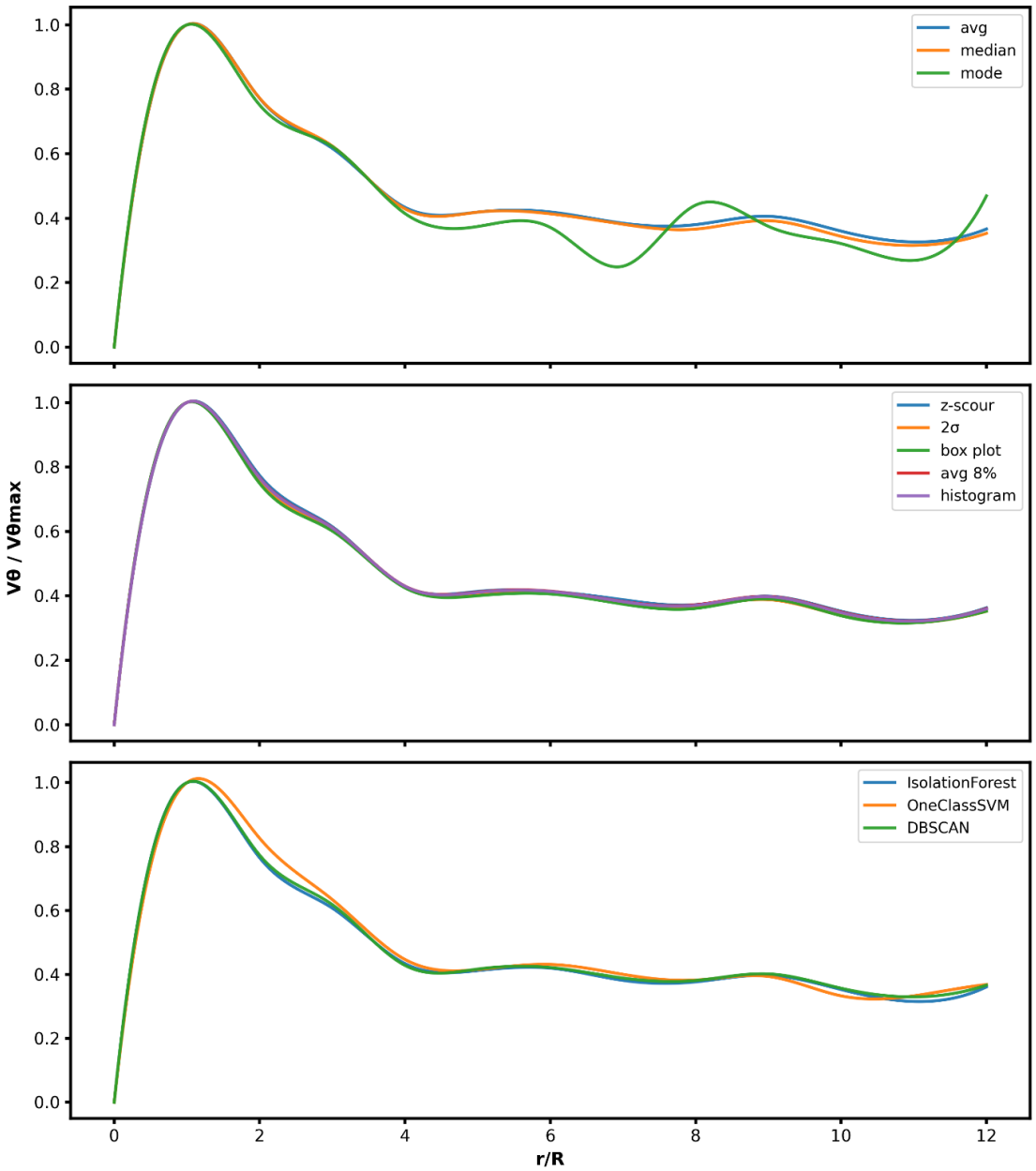


Figure 8. The statistical analyses conducted on a radial cross-section of the vortex for Fr = 1.27

The normalized tangential velocity profiles obtained for Fr = 0.85, 1, and 1.27 demonstrate that the vortex structure near the intake exhibits a stable and coherent behavior consistent with the Rankine vortex model. In all cases, the peak velocity occurs at approximately $r/R \approx 1$ with a normalized magnitude of unity. Beyond this radius, the tangential velocity decreases smoothly, reaching values of about 0.40–0.50 at $r/R = 4$ and 0.28–0.35 at $r/R = 10$. This corresponds to a reduction of nearly 55% in the intermediate region and around 70% in the far field.

In the statistical analysis without outlier removal, the mean and median produced smooth and physically consistent profiles for all Fr. Their differences remained within $0.02 - 0.03$ (approximately 2–3% of the peak value), indicating minimal skewness in the data distribution and acceptable quality of the raw ADV measurements. In contrast, the mode exhibited the poorest and most unstable behavior. For instance, oscillations of up to 15% were observed in Fr = 1 and fluctuations of 5 – 7 % appeared in Fr = 1.27. This nonphysical behavior is attributed to a fundamental limitation of the mode: when the data distribution is multimodal, the method returns only the first detected mode, resulting in artificial peaks and distorted profile shapes.

Applying outlier removal techniques including z-score, 2σ, box plot, average 8%, and histogram resulted in profiles that were nearly identical for all Fr. The differences among these methods remained within 2 – 3 %, and the RMS deviation was typically below 1.5%. This high degree of overlap indicates that the ADV data contain very limited noise and that removing outliers does not alter the fundamental shape of the velocity profile. These methods collectively produced the smoothest, most stable, and most Rankine like profiles, demonstrating that statistical outlier removal provides the most reliable framework for flow characterization across all cases.

Machine learning based outlier detection methods (Isolation Forest, DBSCAN, and One-Class SVM) also produced physically meaningful and smooth profiles, though with varying levels of agreement. Isolation Forest consistently delivered the most accurate and stable results across all Fr, with profiles closely matching those from the most reliable statistical methods. Its superiority arises from its structural mechanism: Isolation Forest isolates outliers through recursive partitioning, requiring fewer splits for points that deviate structurally from the main data cluster. Since the primary body of velocity data forms a coherent geometric trend, this method removes only genuinely anomalous points, minimizing false outlier classification. DBSCAN also performed well; however, due to its sensitivity to density based parameters, small deviations ($\leq$ 2 %) were observed, particularly at higher Fr. One-Class SVM slightly overestimated velocities in the mid radius region by about 0.02–0.03, but overall retained a physically reasonable trend.

The results also show that as the Fr increases from 0.85 to 1.27, fluctuations in the weaker methods increase, highlighting the need for more robust methods in higher-turbulence regimes.

The results of this study are remarkably similar to those of Cea et al. [37] in terms of the importance of processing ADV velocity data; however, the present study provides a more comprehensive and detailed approach. Both studies emphasize that raw ADV data, especially in turbulent and near-free-surface flows, contain significant amounts of spikes and noise, and that proper data processing has a decisive impact on the extraction of velocity profiles and turbulence parameters. In the study by Cea et al., threshold-based and phase-space filters were investigated and it was shown that the turbulence energy and frequency spectrum are strongly affected by the filtering quality.

4. Summary and Conclusions

This research aimed to optimize the Acoustic Doppler Velocimeter (ADV) for

measuring tangential velocities in free-surface vortices at hydraulic intakes. Experiments were conducted in a rectangular tank at Froude numbers of 0.85, 1, and 1.27 and the data were analyzed using statistical and machine learning methods. The results showed A comparison among the three Fr that although flow turbulence slightly increases from Fr = 0.85 to 1.27, the essential vortex structure remains stable. Both statistical and machine learning methods especially Isolation Forest were capable of reconstructing accurate and physically plausible profiles. Across all cases, the RMS deviation among reliable methods remained within 2 – 3 %, whereas the mode exhibited deviations as large as 15%, confirming its unreliability for vortex characterization. These findings demonstrate that the underlying vortex structure is robust with respect to the choice of post-processing method and that only methods with inherent statistical limitations (such as the mode) produce nonphysical results. Overall, the results indicate that statistical methods with outlier removal, along with Isolation Forest, provide the most accurate and trustworthy reconstruction of the vortex velocity profile. These methods yield smooth, noise resistant, and Rankine consistent curves and are therefore recommended for detailed hydrodynamic analysis of free surface vortices. In contrast, the mode consistently exhibited unstable behavior and should not be used for interpreting ADV measurements in similar studies. Future research could focus on fine-tuning the parameters of machine learning models for ADV data to achieve greater accuracy. These findings contribute to improving the design of hydraulic intakes and reducing the risks associated with vortex formation.

Funding Statement
This research received no external funding.

Conflict of Interest
The authors declare that they have no conflict of interest.

Author Contributions
All authors contributed to the study conception and design. Material preparation, data collection, and analysis, were performed by H.A, SR.K and H.S. The first draft of the manuscript was written by H.A and all authors commented on previous versions of the manuscript. All authors read and approved the final manuscript.

References
1. Suerich-Gulick F, Gaskin SJ, Villeneuve M, Parkinson É. Characteristics of free surface vortices at low-head hydropower intakes. Journal of Hydraulic Engineering. 2014 Mar 1;140(3):291-9. https://doi.org/10.1061/(ASCE)HY.1943-7900.0000826
2. Knauss J, editor. Swirling flow problems at intakes. Routledge; 2017 Nov 1.
3. Rankine WJ. A manual of applied mechanics. C. Griffin and Company, Limited; 1901.
4. Hecker GE, editor. Fundamentals of vortex intake flow. IAHR hydraulic structures design manual. Rotterdam: Balkema, [chapters 2 and 8]. 1987.
5. Sarkardeh H, Zarrati AR, Roshan R. Effect of intake head wall and trash rack on vortices. Journal of Hydraulic Research. 2010 Feb 1;48(1):108-12. https://doi.org/10.1080/00221680903565952
6. White F. Fluid Mechanics (5th ed.). New York, NY: McGraw-Hill. 2003.
7. Travis QB, Mays LW. Prediction of intake vortex risk by nearest neighbors modeling. Journal of Hydraulic Engineering. 2011 Jun 1;137(6):701-5. https://doi.org/10.1061/(ASCE)HY.1943-7900.0000344
8. Heravi Z, Azhdary Moghaddam M, Esmaili K, Givehchi M, Bahr Peyma A. Experimental Evaluation of Performance of the New Design of Bed Protection Models (F-jacks) in Altering the Flow Pattern around Bridge Piers. Journal of Hydraulics. 2024 Mar 20;19(1):67-86. https://doi.org/10.30482/jhyd.2023.395247.1643
9. Camnasio E, Orsi E, Schleiss AJ. Experimental study of velocity fields in rectangular shallow reservoirs. Journal of Hydraulic Research. 2011 Jun 1;49(3):352-8.

https://doi.org/10.1080/00221686.2011.574387
10. Sarkardeh H, Jabbari E, Zarrati AR, Tavakkol S. Velocity field in a reservoir in the presence of an air-core vortex. InProceedings of the Institution of Civil Engineers-Water Management 2014 Jun;167(6):356-64. Thomas Telford Ltd. https://doi.org/10.1680/wama.13.00046
11. Mulligan S, Casserly J, Sherlock R. Effects of geometry on strong free-surface vortices in subcritical approach flows. Journal of Hydraulic Engineering. 2016 Nov 1;142(11):04016051. https://doi.org/10.1061/(ASCE)HY.1943-7900.0001194
12. Naderi V, Gaskin S. A 3D study of an intake air-core vortex structure using PIV & flow visualization. In: Proc of 7th International Symposium on Hydraulic Structure. 2018: Aachen, Germany.
13. Naderi V, Farsadizadeh D, Lin C, Gaskin S. A 3D study of an air-core vortex using HSPIV and flow visualization. Arabian Journal for Science and Engineering. 2019 Oct;44(10):8573-84. https://doi.org/10.1007/s13369-019-03764-3
14. Duinmeijer A, Oldenziel G, Clemens F. Experimental study on the 3D-flow field of a free-surface vortex using stereo PIV. Journal of Hydraulic research. 2020 Jan 2;58(1):105-19. https://doi.org/10.1080/00221686.2018.1555558
15. Hamidi, S., Sarkardeh, H., Bashtani, A. Spiral Flow Measurement at Vertical Intakes Using PTV Method. Journal of Hydraulic Structures, 2024; 11(1): 41-50. doi: 10.22055/jhs.2024.47215.1304
16. Azarpira M, Sarkardeh H, Tavakkol S, Roshan R, Bakhshi H. Vortices in dam reservoir: A case study of Karun III dam. Sadhana. 2014 Oct;39(5):1201-9. https://doi.org/10.1007/s12046-014-0252-7
17. Amiri SM, Zarrati AR, Roshan R, Sarkardeh H. Surface vortex prevention at power intakes by horizontal plates. InProceedings of the institution of civil engineers-water management 2011 Apr;164(4):193-200. Thomas Telford Ltd. https://doi.org/10.1680/wama.1000009
18. Khanarmuei M, Rahimzadeh H, Sarkardeh H. Investigating the effect of intake withdrawal direction on critical submergence and strength of vortices. Modares Mechanical Engineering. 2015;14(10):35-42.
19. Khanarmuei MR, Rahimzadeh H, Kakuei AR, Sarkardeh H. Effect of vortex formation on sediment transport at dual pipe intakes. Sādhanā. 2016 Sep;41(9):1055-61. https://doi.org/10.1007/s12046-016-0531-6
20. Khanarmuei M, Rahimzadeh H, Sarkardeh H. Effect of dual intake direction on critical submergence and vortex strength. Journal of Hydraulic Research. 2019 Mar 4;57(2):272-9. https://doi.org/10.1080/00221686.2018.1459896
21. Monshizadeh M, Tahershamsi A, Rahimzadeh H, Sarkardeh H. Comparison between hydraulic and structural based anti-vortex methods at intakes. The European Physical Journal Plus. 2017 Aug 3;132(8):329. https://doi.org/10.1140/epjp/i2017-11608-4
22. Monshizadeh M, Tahershamsi A, Rahimzadeh H, Sarkardeh H. Vortex dissipation using a hydraulic-based anti-vortex device at intakes. International Journal of Civil Engineering. 2018 Sep;16(9):1137-44. https://doi.org/10.1007/s40999-017-0266-8
23. Taghizadeh A, Sarkardeh H, Azamathulla HM. Mechanisms of free surface vortex formation at water intakes (a review). Dams and Reservoirs. 2025 Sep 11. https://doi.org/10.1680/jdare.25.01007
24. Amini AA, Sarkardeh H, Jabbari E, Eidi A. Understanding vortex characteristics in hydraulic systems: a temperature-driven analysis. Modeling Earth Systems and Environment. 2024 Jun;10(3):3559-71. https://doi.org/10.1007/s40808-024-01969-6
25. Zhang B, Ma L, Cheng L, Zhu B, Qin Y. Characterization of free-surface vortex evolution and its impact on hydraulic stability of the pump sump. Experimental Thermal and Fluid Science. 2025 Jul 1;166:111466. https://doi.org/10.1016/j.expthermflusci.2025.111466
26. Jiao W, Fan H, Xi X, Shen J, Zhou L, Jia X, Wang Z, Cheng L. Study on the key influencing factors and vortex characteristics of the water jet propulsion pump underwater suction vortex. Physics of Fluids. 2025 Sep 1;37(9). https://doi.org/10.1063/5.0287735
27. Mondal RK, Rohilla L, Kumar P. Free surface vortex and associated air entrainment during liquid drainage using two outlets. Experimental Thermal and Fluid Science. 2025 Jan 1;160:111314.

https://doi.org/10.1016/j.expthermflusci.2024.111314
28. Roushangar K, Akhgar S, Salmasi F, Shiri J. Modeling energy dissipation over stepped spillways using machine learning approaches. Journal of Hydrology. 2014 Jan 16;508:254-65. https://doi.org/10.1016/j.jhydrol.2013.10.053
29. Ghorbani MA, Salmasi F, Saggi MK, Bhatia AS, Kahya E, Norouzi R. Deep learning under H2O framework: A novel approach for quantitative analysis of discharge coefficient in sluice gates. Journal of Hydroinformatics. 2020 Nov 1;22(6):1603-19. https://doi.org/10.2166/hydro.2020.003
30. Ghorbani MA, Khatibi R, Singh VP, Kahya E, Ruskeepää H, Saggi MK, Sivakumar B, Kim S, Salmasi F, Hasanpour Kashani M, Samadianfard S. Continuous monitoring of suspended sediment concentrations using image analytics and deriving inherent correlations by machine learning. Scientific reports. 2020 May 22;10(1):8589. https://doi.org/10.1038/s41598-020-64707-9
31. Salmasi F, Abraham J. Expert system for determining discharge coefficients for inclined slide gates using genetic programming. Journal of Irrigation and Drainage Engineering. 2020 Dec 1;146(12):06020013. https://doi.org/10.1061/(ASCE)IR.1943-4774.0001520
32. Salmasi F, Sihag P, Abraham J, Nouri M. Experimental investigation and prediction of free fall jet scouring using machine learning models. International Journal of Sediment Research. 2023 Jun 1;38(3):405-20. https://doi.org/10.1016/j.ijsrc.2022.11.004
33. Anwar HO, Weller JA, Amphlett MB. Similarity of free-vortex at horizontal intake. Journal of Hydraulic Research. 1978 Apr 1;16(2):95-105. https://doi.org/10.1080/00221687809499623
34. Liu FT, Ting KM, Zhou ZH. Isolation forest. In2008 eighth ieee international conference on data mining 2008 Dec 15 (pp. 413-422). IEEE. https://doi.org/10.1109/ICDM.2008.17
35. Manevitz LM, Yousef M. One-class SVMs for document classification. Journal of machine Learning research. 2001;2(Dec):139-54.
36. Bushra AA, Yi G. Comparative analysis review of pioneering DBSCAN and successive density-based clustering algorithms. IEEE Access. 2021 Jun 14;9:87918-35. https://doi.org/10.1109/ACCESS.2021.3089036
37. Cea L, Puertas J, Pena L. Velocity measurements on highly turbulent free surface flow using ADV. Experiments in fluids. 2007 Mar;42(3):333-48. https://doi.org/10.1007/s00348-006-0237-3

© 2026 by the authors. Licensee SCU, Ahvaz, Iran. This article is an open access article distributed under the terms and conditions of the Creative Commons Attribution 4.0 International (CC BY 4.0 license) (http://creativecommons.org/licenses/by/4.0/).

Development of an Efficient Multi-Reach Partitioning Approach with Linear Muskingum Method and Weighted Mean of Vectors Algorithm for Inverse Flood Routing

Maziar Rastegarfar [1], Ali Raeisi Isa-Abadi [2,*], Hamed Reza Zarif Sanayei [1]

1. Department of Civil Engineering, Shahrekord University, Shahrekord, Iran.
2. Department of Water Engineering, Shahrekord University, Shahrekord, Iran.

***Corresponding Author:**
Ali Raeisi Isa-Abadi

Email: ali_raeisi@sku.ac.ir
Received: 2025.11.26
Accepted: 2026.02.10
J. Hydraul. Struct., 12(3):70-93
DOI: 10.22055/jhs.2026.51239.1369

ABSTRACT

This study presents an inverse routing method based on the linear Muskingum model, utilizing a new and efficient optimization algorithm i.e., the weIghted meaN oF vectOrs (INFO) to determine optimal routing parameters. Additionally, the analyzed rivers are segmented into smaller intervals, then the linear Muskingum routing method is applied separately and consecutively to each interval. Furthermore, lateral flow contribution has been integrated into the calculation process to improve routing accuracy in the linear Muskingum method. It is worth noting that this study is novel in two key aspects: it is the first to apply a partitioning approach to an inverse flood routing strategy, and, more broadly, across all types of flood routing—whether inverse or direct—it marks the first instance in which the number of sub-reaches has been optimized within an inverse Muskingum flood routing framework, while simultaneously estimating routing parameters and accounting for lateral flow effects. The proposed Muskingum model is investigated on three flood events, and its performance is compared to existing methods reported in the literature. The sum of squared errors (SSQ) significantly decreases for each analyzed flood event, with best SSQ values of 167.03 for the triangular flood hydrograph, 371.55 for the Wilson data, and 128.63 for the double-peak hydrograph. Also, the Standardized Absolute Deviation (SAD) evaluation criteria, yielding best SAD values of 194.17, 70.03, and 45.83 for the respective events, along with the visual agreement of observed input hydrographs and the resulting routing hydrographs, highlight the advantages of the proposed method.

KEYWORDS
Inverse Flood routing, linear Muskingum method, INFO, optimization algorithms, Multi-reach.

1. Introduction

Flood routing is conducted in direct and inverse modes. Inverse routing determines the upstream hydrograph characteristics based on the specifications of the downstream hydrograph. It provides valuable insights into upstream inflow flood characteristics, which are crucial for estimating reconstruction and renovation costs associated with upstream flooding. Additionally, it assists in determining the appropriate volume of water to release from a regulation dam to meet downstream flow requirements. Furthermore, inverse routing can be employed to validate data from upstream hydrometric stations.

Muskingum method is based on continuity and storage equations and can be implanted using both linear and non-linear models [1]. Due to the high computational costs for calibration, the non-linear models are recommended primarily when discharge and storage equations exhibit non-linearity [2]. On the other hand, the linear Muskingum equation is not only simpler but also more cost-effective than non-linear Muskingum methods. Consequently, this approach has been extensively utilized in variety of researches.

Samani and Shamsipour [3] proposed a model using the linear Muskingum method (LMM) for flood routing in multi-branch rivers. They employed a non-linear optimization method to estimate the required parameters. Al-Humoud and Esen [4] presented two approximate methods for estimating linear Muskingum model parameters. In the first method, it was essential to calculate the slopes of both the inflow and outflow hydrographs at the intersection point, as well as the maximum storage volume within that region. In contrast, the second method required the calculation of the inflow and outflow hydrographs at only two specific points.

In order to estimate the parameters of the Muskingum method, Ayvaz and Gurarsian [5] presented a new model which can be applied to all flood routing programs Their results showed that proposed model significantly enhances the performance of the Muskingum method. Bazargan and Norouzi [6] utilized the LMM for Molasani and Ahvaz hydrometry stations located upstream and downstream of the Karun River. They demonstrated that the accuracy of this method can be improved by using variable values instead of constant parameters for X, K, and Δt, particularly at the peak of hydrograph. Norouzi and Bazargan [7] estimated the parameters of a linear model for two major floods, as opposed to just one, in eight different models. Their findings indicated that by applying the arithmetic mean values of X and K, along with the geometric mean value of Δt related to two significant floods, they attained improved accuracy in estimating the peak section of the downstream hydrograph. Omran et al. [8] employed Muskingum's graphical method along with numerical methods to conduct flood routing. The improved bat algorithm (IBA) was also used in that study to optimize the estimated values of the Muskingum model. Results indicated that all numerical methods could estimate the parameters of Muskingum's graphical method, but the IBA was the best method as it fits data with minimum errors. In a research [9], the parameters of the Muskingum model were optimized to accurately simulate hourly flood hydrographs for three rivers within the Karun watershed. The researchers assessed the model's performance using the correlation coefficient (CC), the ratio of the root-mean-square error to the standard deviation of measured data (PSR), Nash–Sutcliffe efficiency (NSE), and index of agreement (d). The findings demonstrated that the gray wolf optimization (GWO) algorithm provided superior performance in simulating floods in the study area. Salvati et al. [9] combined the nonLMM with a new lateral flow equation based on five decision variables to perform flood routing more accurate. In a research conducted by Mohsenabadi [10], a Multilinear Muskingum method was developed specifically for D-shape cross-section and compared against the Saint-Venant model. This research focused on optimizing discharge coefficients to obtain water surface profiles. Results indicated a suitable agreement between routed hydrographs and water surface profiles.

Although there have been extensive studies in the field of the Muskingum model for direct flood routing, its application for inverse flood routing remains limited. Inverse flood routing was first performed by Eli et al. [11] on the James River in Virginia using the Saint-Venant equations. They noted numerical instabilities, particularly at low discharges. Das [12] presented the inverse routing method for the

Muskingum model using Lagrange multipliers for optimizations. A study by Koussis et al. [13] , applied the Muskingum method for inverse flood routing and observed that input hydrographs were estimated with good accuracy. In another research, Hosseini Dehnoi [14] used Genetic Algorithm (GA) to define the inverse LMM in multi-branch rivers. The algorithm proved to be accurate and effective in generating artificial data rather than real data. Badfar et al.[15] developed a new model for inverse flood routing based on the Muskingum model. They used the Euler numerical and Runge-Kutta fourth order methods to solve the storage function while the Shuffled Complex Evolution (SCE) algorithm was employed for parameters optimization.

To achieve accurate results in flood routing, it is essential to estimate the Muskingum parameters optimally. Due to the complexity of these calculations, various methods, including metaheuristic optimization algorithms, have been introduced over the years. Mohan [16] applied Genetic Algorithm (GA) for estimating parameters in linear and non-linear models. Results illustrated that using GA was more appropriate than previous methods and initial assumption close to optimal solution was not required. Moghadam et al. [17] examined the application of all linear and non-linear Muskingum models using Particle Swarm Optimization (PSO) algorithm. Ultimately, the most appropriate Muskingum model was selected based on evaluation criteria comparing observed and computed discharges. Badfar et al. [18] utilized Shuffled Complex Evolution (SCE) algorithm to optimize Muskingum parameters. Their results indicated that the algorithm performs well and shows good agreement between computed and observed hydrographs in simulating floods. In another research, RezapourTabari and Emami Dehcheshmeh [19] proposed a novel structure for the non-linear Muskingum model. A combination of Particle Swarm Optimization (PSO) and Dove Swarm Optimization (DSO) metaheuristic algorithms were used for optimization of parameters. Norouzi et al. [20] utilized data from four floods in the Karun River to optimize flood routing using the PSO algorithm. In their research, the LMM parameters were separately optimized and applied to compute outflow hydrographs for each flood.

Considering the limited knowledge and studies in the literature on inverse flood routing using the Muskingum method along rivers, it is essential to conduct research in this field. Therefore, the current study develops a linear Muskingum model for multi-reach inverse routing in several flood-prone rivers. Also, given the need to obtain optimal values for effective parameters in this area, the weIghted meaN oF vectOrs (INFO) algorithm is utilized to optimize LMM parameters and determine the optimal number of ranges. INFO is a new and powerful algorithm, that has not been widely used in different fields of water engineering. It is worth mentioning; the multi-reach method constitutes a novel approach proposed in this research. Furthermore, the investigation of lateral discharge has been conducted in this study to enhance the accuracy of computational outcomes.

2. Materials and methods

2.1. Inverse flood routing approach

The current study applies the linear Muskingum method for inverse flood routing, incorporating two fundamental equations: the continuity and the linear storage equations. The continuity equation (Eq. 1) states that the variation in storage volume over time is equal to the difference between inflow and outflow. Also, the storage equation (Eq. 2) establishes a linear relationship between the storage volume and the inflow and outflow rates,

$$\frac{dS}{dt} = (1+\beta)(I-O) \quad (1)$$

$$S = K[X(1+\beta)I + (1-X)O] \quad (2)$$

where I and O represent inflow and outflow rates, respectively, S corresponds the total water storage volume, X is a dimensionless weighting factor that indicates the relative importance of inflow (I) and outflow (O) in relation to the storage volume (S). Acceptable values of X range between 0 and 0.5, as values exceeding 0.5 result in an unrealistic increase in flood peaks, while negative values are considered practically meaningless for the weighting factor [21] . K represents the storage time constant and depends on factors such as channel length and flood wave celerity. The value of K is approximately equal to the time required for the flood to pass through the river. The parameter β represents the coefficient or contribution of lateral flow with respect to the inflow, which may vary along the river, either increasing or decreasing [22].

In inverse flood routing, unlike the direct procedure, the inflow rate at the beginning of a time step is the unknown variable to be determined. Therefore, by applying Eqs. (1) and (2) over a time interval of length Δt, with indices 1 and 2 representing values at the beginning and end of the time step, respectively, the upstream discharge at the start of the time step can be computed using the following equation:

$$I_1 = C_1 O_2 + C_2 O_1 + C_3 I_2 \tag{3}$$

Where C_1, C_2, and C_3 are obtained as follows:

$$\begin{aligned} C_1 &= \frac{1}{(1+\beta)} \frac{K(1-X)+\theta\Delta t}{KX+(1-\theta)\Delta t} \\ C_2 &= -\frac{1}{(1+\beta)} \frac{K(1-X)-(1-\theta)\Delta t}{KX+(1-\theta)\Delta t} \\ C_3 &= \frac{KX-\theta\Delta t}{KX+(1-\theta)\Delta t} \end{aligned} \tag{4}$$

where θ is a parameter used to weight the average of the inflow/outflow (I/O) values at the beginning and end of each time step. Knowing the parameters K and X, the coefficients C_1, C_2, and C_3 can be computed. The value of I_1 in Eq. (3) can be determined using the outflow at the beginning and end of the time step, along with the inflow at the end of the time step. This process can then be iterated in reverse through successive time steps until the upstream hydrograph is completely calculated. It is important to emphasize that the derivation of Eqs. (3) and (4) to perform inverse flood routing while incorporating lateral discharge constitutes a key innovation presented in this study.

2.2. Multi-reach LMM in inverse flood routing

To improve the accuracy of the proposed flood routing procedure, a multi-reach version is also introduced. The term "multi-reach" refers to the division of the river reach into two or more sub-reaches (Fig. 1). Consequently, the flood routing procedure can be applied separately to each sub-reach, successively following the completion of the previous one. It should be noted that, since the proposed approach is a lumped model, the spatial location and manner in which the river reach is divided into sub-reaches are entirely unimportant. The only aspect that matters is the number of divisions. This is why the sub-reach lengths are shown as equally spaced in Fig. 1.

In general, the flood routing procedure begins from the last sub-reach (most downstream), proceeds upstream, and ends at the first sub-reach (most upstream). Using the outflow hydrograph for each sub-reach and applying Eq. (3), the corresponding inflow hydrograph can be determined. Note that, except for the last sub-reach where the outflow data is known (from the observed hydrograph at the downstream end of the river), the outflow data for the remaining sub-reaches is unknown and needs to be determined. By using the computed inflow hydrograph as the outflow hydrograph for the subsequent upstream sub-reach, this issue is effectively resolved. Thus, this iterative procedure should begin with the last sub-reach and continue until reaching the first one.

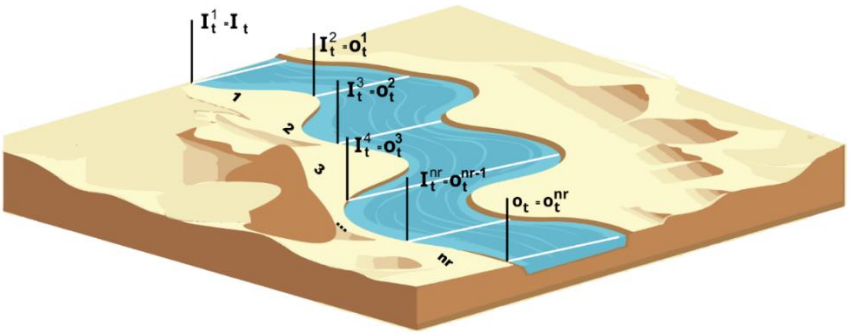


Figure 1. Multi-reach LMM in inverse routing

It should be noted that the Muskingum parameters are assumed constant in all reaches. While these parameters can be varied in every sub-reach, considering uniform parameters in the presented study reduces the number of decision variables and minimizes uncertainties associated with parameter estimation. Moreover, to enhance the accuracy of routing computations, this study introduces the calculation of the optimal number of sub-reaches for a given river as a key decision variable, marking a novel contribution to the methodology as it has not been previously utilized in the literature. Therefore, in addition to K, X, and β, the number of sub-reaches (nr) is a new parameter in the proposed Muskingum model and must be determined. The optimization technique (INFO algorithm) is utilized to calculate the optimal values of these parameters.

2.3. INFO optimization algorithm

Ahmadianfar et al. [23] introduced a novel optimization algorithm, called weighted mean of vectors, which can aid the formation of a solid structure by modifying the weighted mean method and updating the location of vectors. INFO is a population-based algorithm that computes the weighted mean of set of vectors in search space. The population includes a set of vectors illustrating possible solutions. INFO algorithm finds solutions in multiple consecutive generations. This algorithm consists of the following main phases that we address in the context of a minimization problem.

Initialization phase*:*

A population of INFO vectors can be represented as $\boldsymbol{X}^{g,l} = \{\boldsymbol{x}_1^{g,l}, \boldsymbol{x}_2^{g,l}, \cdots, \boldsymbol{x}_D^{g,l}\}$, where $g = 0,1,2,\cdots,g_{max}$ denotes the generation number, D is the dimension of the search domain, and $l = 1,2,\cdots,N_p$ corresponds to the l^{th} vector of the current population. This algorithm uses a random methodology for generating the initial population of vectors ($\boldsymbol{X}^{0,l}$). In this stage, some major control parameters called weighted mean coefficient δ and scaling coefficient s are also introduced for the INFO [23].

Rule renewal phase:

In INFO, in contrast to other methods, a mean-based renewing rule is used to generate new vectors, increasing the convergence rate. Updating the rule operator increases population diversity during the search procedure and generates new vectors using the weighted mean of vectors. The mean-based rule consists of two terms and is defined as follows [23]:

$$Mrule = \sum_{i=1}^{2} \alpha_i \times MBW_i^{g,l},\ \alpha_1 = r,\ \alpha_2 = 1 - r \quad (5)$$

where r is a random value in the range [0,0.5]; $MBW_i^{g,l}$ is obtained as follows:

$$MBW_i^{g,l} = \delta \times \frac{\sum_{j=1}^{3} w_j^i \left(x_{a_j}^i - x_{a_{j+1}}^i\right)}{\varepsilon + \sum_{j=1}^{3} w_j^i} + \varepsilon \times rnd, \quad if \quad (j+1) > 3: x_{a_{j+1}}^i = x_{a_1}^i$$
$$w_j^i = \cos\left(\left[f\left(x_{a_j}^i\right) - f\left(x_{a_{j+1}}^i\right)\right] + \pi\right) \exp\left(-\frac{f\left(x_{a_j}^i\right) - f\left(x_{a_{j+1}}^i\right)}{\omega_i}\right) \quad (6)$$

$l = 1, 2, \cdots, Np$, $g = 1,2, \cdots, g_{max}$, $i = 1,2$ and $j = 1, \cdots, 3$

where f represents the objective function (OF), $\omega_i = \max\left\{f\left(x_{a_j}^i\right)\right\}_{j=1}^{3}$. The values of $\{a_j\}_{j=1}^{3}$ } depend entirely on which term (i =1 or i =2) in Eq. (6) is being calculated. If $i = 1$, they represent three distinct numbers between 1 and Np, randomly generated to select three different vectors from the population in the g^{th} generation. Conversely, if i =2, they correspond to the best, better and worst solutions, respectively. That is, $x_{a_1}^2 = x_{bs}^{g,l}$, $x_{a_2}^2 = x_{bt}^{g,l}$, and $x_{a_3}^2 = x_{ws}^{g,l}$, where x_{bs}, x_{bt}, and x_{ws} are, respectively, the best, better, and worst solutions and $l = 1, 2, \cdots, Np$, $g = 1,2, \cdots, g_{max}$. ε is a constant value with low quantity, rnd is a random value. The δ scale coefficient is obtained using, $\delta = 4(rand - 0.5)\exp\left(\frac{-4g}{g_{max}}\right)$, where g_{max} is the maximum number of generations. Finally, the two new vectors are achieved based on

$$z_1^{g,l} = x_1^{g,l} + s \times Mrule + C_{A1}$$
$$z_2^{g,l} = x_2^{g,l} + s \times Mrule + C_{A2} \quad (7)$$

where C_{A1} and C_{A2} are the convergence acceleration terms added for updating the rule operator. $s = 4(rand - 0.5)\exp\left(\frac{-4g}{g_{max}}\right)$ is the scaling factor and notably, when the parameter s takes on large values, the current position shifts away from the weighted mean of the vectors, promoting exploration. Conversely, smaller values of s encourage the current position to converge toward the weighted mean, enhancing exploitation.

Combining phase:

By combining the two newly generated vectors ($z_1^{g,l}$and $z_2^{g,l}$) from the previous step, a new solution ($u^{g,l}$) is obtained. Two random values are generated to combine the vectors. For a given l^{th} vector, the first random value determines whether its position is updated, while the second random value dictates how $z_1^{g,l}$ and $z_2^{g,l}$ are merged to create a unique new vector solution, denoted as $u^{g,l}$ (see [23], for more details).

Local search phase:

While the last two phases focus on both exploration and exploitation of the algorithm, this phase places greater emphasis on exploitation. This objective is achieved through the use of global location (x_{best}^G) and the mean-based rule (see Eq. 5). According to this operator, a new vector can be generated in proximity to x_{best}^G by a random value between 0 and 1 [23]. Fig. 2 depicts the flowchart of the INFO and the optimization process.

2.4. Estimation of parameters and optimization procedure

The proposed inverse flood routing procedure involves estimating the parameters K, X, β and nr. To determine these parameters, an optimization process is required. For this purpose, the INFO algorithm is employed, with the sum of squared deviations (SSQ) serving as the OF:

$$SSQ = \sum_{i=1}^{N} (\hat{I}_i - I_i)^2 \quad (8)$$

Fig. 3 illustrates the integration of the INFO algorithm with the inverse flood routing procedure to determine the optimal parameters values.

2.5. Evaluation criteria

To validate the efficiency of the INFO optimization algorithm and assess the impact of the multi-reach approach applied in inverse flood routing using the LMM, some evaluation criteria are employed.

1- Accuracy of optimization method: The accuracy of the optimization method can be evaluated using the sum of absolute difference (SAD) between observed inflow ($\hat{I}_i$) and calculated inflow (I_i) at i^{th} time, These metrics are defined as follows:

$$SAD = \sum_{i=1}^{N} |\hat{I}_i - I_i| \quad (9)$$

Where N is the number of recorded data.

Lower SAD value indicates a closer agreement between the calculated results and the observed data, demonstrating reduced calculation errors.

2- Magnitude of Flood Peak: The absolute deviation between the peak values of the observed inflow ($\hat{I}_i^{peak}$) and the routed inflow (I_i^{peak}), referred to as DPO, represents a criterion for assessing the magnitude of the peak inflow.

$$DPO = |\hat{I}_i^{peak} - I_i^{peak}| \quad (10)$$

The lower the DPO value, the closer the observed and calculated values are.

3- Mean absolute relative error: The mean absolute relative error (MARE) between the observed and calculated inflows is considered as:

$$MARE = \frac{1}{N}\sum_{i=1}^{N} \frac{|\hat{I}_i - I_i|}{\hat{I}_i} \quad (11)$$

A lower MARE value indicates a reduced average relative difference between the observed and calculated inflows, which implies better model accuracy and performance.

4- Variance: The similarity in the shape and size of the hydrograph can be quantified using the variance criterion (VarexQ), which is expressed as:

$$VarexQ = \left(1 - \frac{\sum_{i=1}^{N}(\hat{I}_i - I_i)^2}{\sum_{i=1}^{N}(\hat{I}_i - \hat{I}_i^{mean})^2}\right) \times 100 \quad (12)$$

Where $\hat{I}_i^{mean}$ is the mean observed inflow.

A higher $VarexQ$ value indicates greater similarity between the observed and calculated inflow hydrographs.

5- Coefficient of determination (R^2): The R^2 value quantifies the proportion of variance in the observed inflows that is explained by the calculated inflows. A value of R^2 =1 indicates perfect agreement between the observed and calculated inflows, while R^2=0 suggests no correlation.

$$R^2 = \frac{[\sum_{i=1}^{N}(\hat{I}_i - I_i)(\hat{I}_i^{mean} - I_i^{mean})]^2}{\sqrt{\sum_{i=1}^{N}(\hat{I}_i - I_i)^2 \sum_{i=1}^{N}(\hat{I}_i^{mean} - I_i^{mean})^2}} \quad (13)$$

Where I_i^{mean} is the mean calculated inflow.

6- The Kling-Gupta (KG) Efficiency coefficient: It is a criteria particularly used to evaluate the overall performance of hydrological models by considering multiple aspects of model accuracy, including correlation, variability, and systematic errors. It is defined as:

$$KG = 1 - \sqrt{(R-1)^2 + \left(\frac{\sigma}{\hat{\sigma}} - 1\right)^2 + \left(\frac{I_i^{mean}}{\hat{I}_i^{mean}} - 1\right)^2} \quad (14)$$

Where and $\hat{\sigma}$ and σ are standard deviations of observed and calculated inflow, respectively [24].

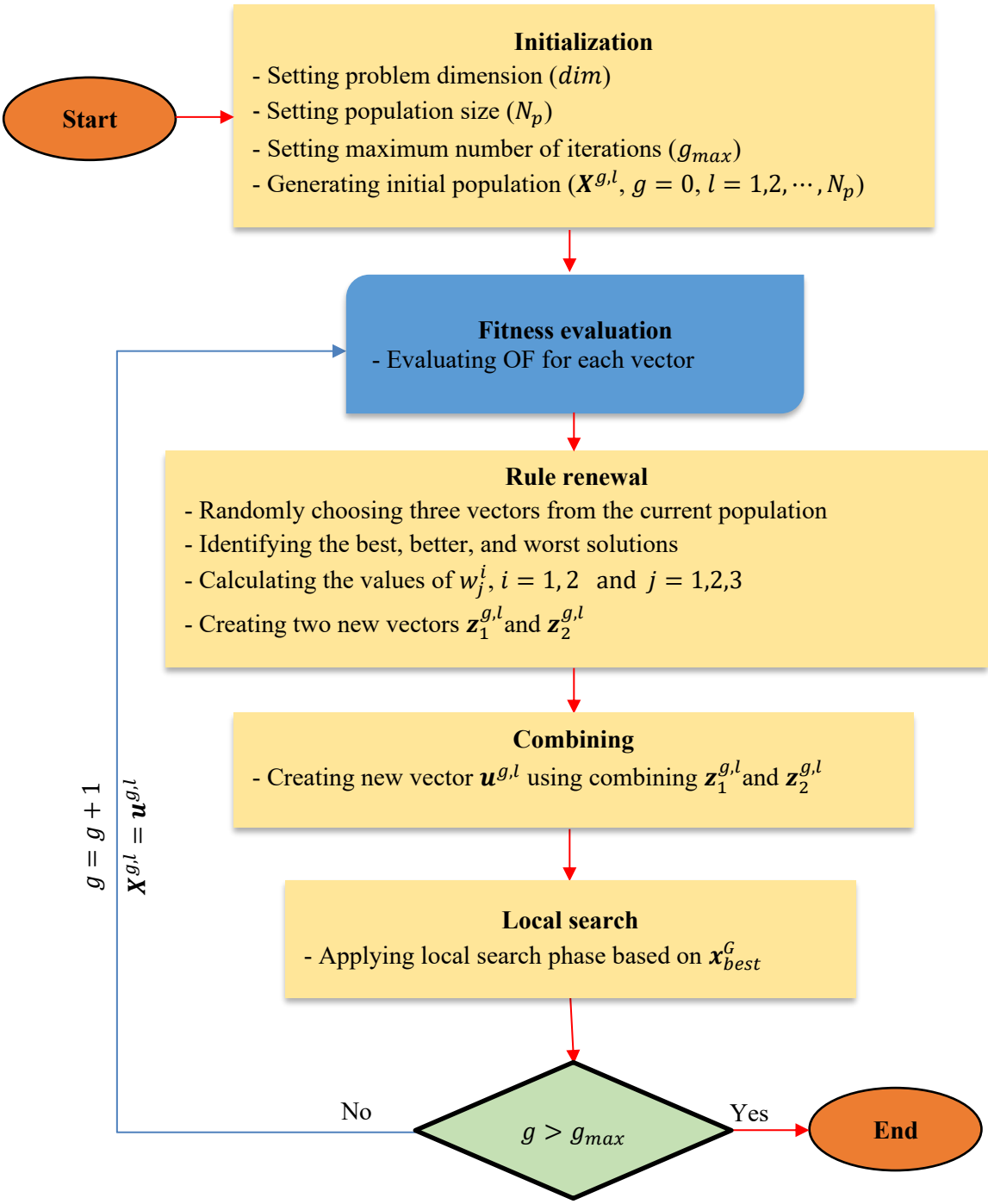


Figure 2. Flowchart of the weighted mean of vectors (INFO) algorithm

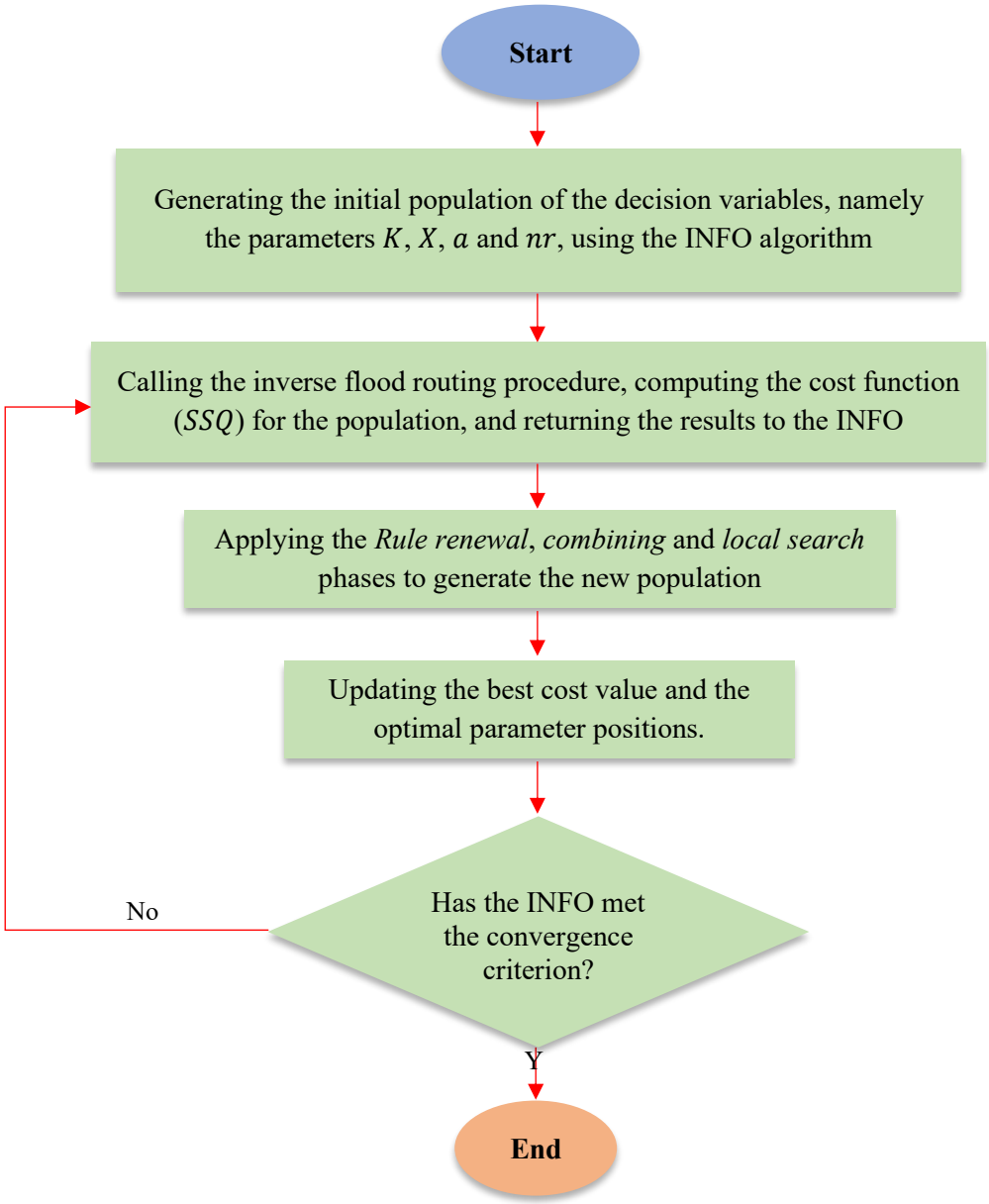


Figure 3. The process of determining the optimal parameter values through the integration of the INFO algorithm and the inverse flood routing procedure.

3. Results and discussion

The present study evaluates the performance of the proposed Muskingum method using triangular, single-peak, and double-peak flood hydrographs. The evaluation criteria computed in this research are compared with other established methods in the literature. To identify the optimal values of the decision variables in the Muskingum method and ensure rapid convergence during optimization, the following parameter ranges are considered: $0 < X < 0.5$, $0 < K < 60$, $-1 < \beta < 1$. Additionally, the parameters for the INFO algorithm employed across all experiments are specified as follows: N_p=30, dim=4, and g_{max}=2000.

According to the reported flood data, the analysis includes 43-time steps, with each time step having a duration of 3 hours (N = 43, Δt = 3).

Fig. 4 illustrates the convergence process of the INFO optimization algorithm in determining the decision variables of the triangular flood hydrograph. As shown, the algorithm begins with a randomly generated initial solution, which is inaccurate, and iteratively reduces the OF value to achieve an optimal solution.

The optimal parameter values for both the single- and multi-reach LMMs, along with the corresponding optimal value of nr, are presented in Table 1. For each number of partitions (nr), the reported Muskingum

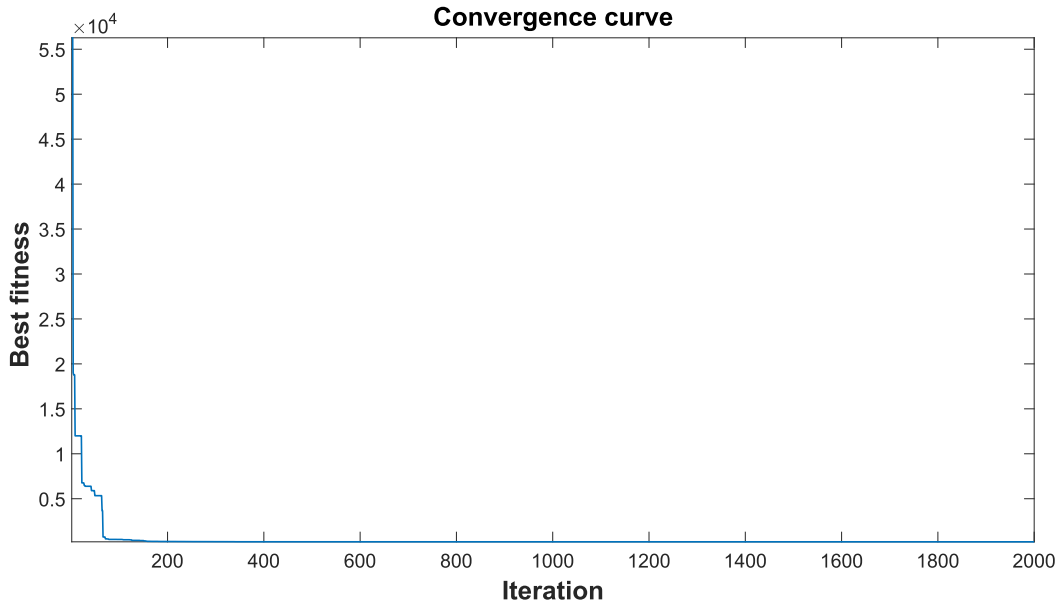


Figure 4. Convergence procedure of multi-reach Muskingum parameters by INFO algorithm for triangular flood data

3.1. Triangular flood hydrograph

A synthetic triangular inflow hydrograph within a rectangular channel with a length of 4500 m, a surface width of 60 m, a surface slope of 0.01, and a Manning coefficient of 0.035 is utilized in this study. The flood demonstrates a linear relationship between the storage volume rate and the difference between inflow and outflow, making it a suitable case for evaluating the proposed method in this study [25]. parameters (K, X, β) represent effective values for the entire multi-reach system. Table 2 presents the inverse-routed flood hydrograph at the river upstream in comparison to the observed flood data. As demonstrated, the obtained results exhibit a strong agreement with the observed data, highlighting the accuracy and reliability of the proposed method.

Saghafian et al. [25] utilized the triangular hydrograph data to validate their

suggested method. They applied the kinematic wave method with a 3-minute time step for simulating the upstream hydrograph. Similarly, Badfar et al. [15] used the triangular hydrograph data for inverse routing by LMM incorporating Euler numerical models and the fourth-order Runge-Kutta method for time discretization. To enhance the accuracy of the results, they employed the Shuffled Complex Evolution (SCE) algorithm to define the Muskingum parameters. Fig. 5 illustrates the inverse-routed inflow hydrograph using the INFO optimization algorithm, compared with the observed upstream hydrograph. The results from Saghafian et al. [25] and Badfar et al. [15] are also superimposed. As shown, the hydrograph obtained using the proposed approach is smoother and demonstrates good agreement with the observed data, whereas the inflow hydrograph calculated by Saghafian et al. [25] exhibits significant fluctuations in flow value.

To quantitatively compare the proposed method in the current study with the results of Saghafian et al. [25] and Badfar et al. [15] , evaluation criteria are presented here (see Table 3). As can be concluded, the results of the suggested method are more accurate than those of the two other studies. The SSQ, SAD, and DPO are the common evaluation criteria used across all studies. These three metrics consistently demonstrate that the proposed approach outperforms previous methods without exception. Specifically, the SSQ value shows significant improvement—by 64% and 31% compared to the studies of Saghafian et al. [25] and Badfar et al. [15] , respectively. This indicates the effectiveness and strength of INFO in minimizing the SSQ, highlighting its applicability and benefits in achieving optimal solutions in flood routing problems.

Table 1- Optimal parameter values of single- and multi-reach LMM for the triangular flood data

Method	X	K(h)	β	nr
Single-reach	0.1993	3.1794	0.0033	-
Multi-reach	0.18	5	-0.52	4

Table 2-The results of the suggested inverse flood routing procedure for the triangular hydrograph

	Observed hydrograph		Routed hydrograph
Time (hr)	Inflow (m^3/s)	Outflow (m^3/s)	Inflow (m^3/s)
0	54	54	54.19
3	54	54	54.40
6	54	54	54.83
9	54	54	55.69
12	57	54.05	57.15
15	60	54.25	59.36
18	63	54.68	62.53
21	69	55.51	66.67
24	75	56.88	71.77
27	81	58.92	77.70
30	87	61.74	84.21
33	93	65.35	91.11
36	99	69.71	98.20
39	105	74.72	105.34
42	111	80.28	112.39
45	117	86.24	119.30
48	123	92.49	126.02
51	129	98.92	132.46
54	135	105.47	138.42
57	141	112.06	143.55
60	147	118.67	147.02
63	153	125.27	147.68
66	147	131.29	145.39
69	141	135.97	140.81
72	135	138.8	134.90
75	129	139.66	128.45
78	123	138.75	121.91
81	117	136.41	115.54
84	111	133	109.41
87	105	128.86	103.48
90	99	124.21	97.77
93	93	119.26	92.20
96	87	114.11	86.78
99	81	108.86	81.48
102	75	103.55	76.37
105	69	98.23	71.51
108	63	92.92	67.01
111	60	87.71	62.82
114	57	82.69	58.77
117	54	77.96	53.94
120	54	73.61	53.51
123	54	69.73	53.99
126	54	66.37	54.00

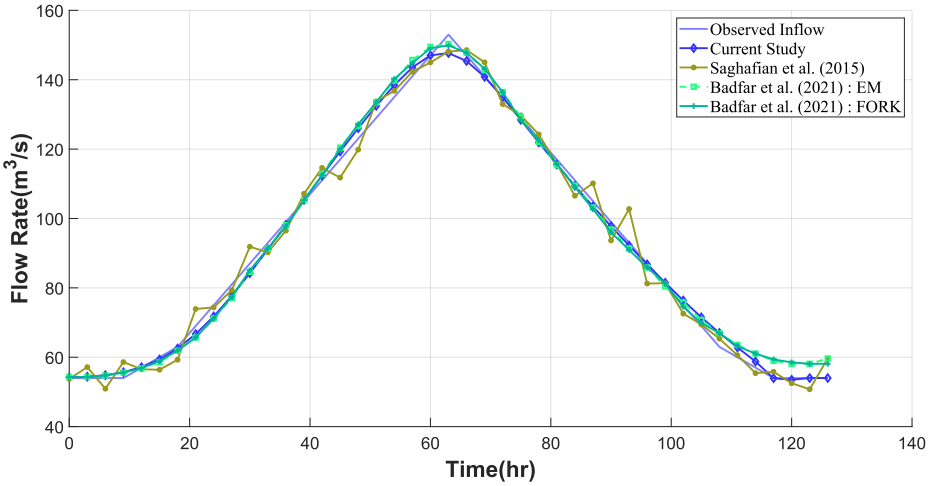


Figure 5. The routed inflow hydrograph in comparison with those of Saghafian et al. [25] and Badfar et al. [15] for the triangular flood data

Table 3. Muskingum methods evaluation criteria for the triangular flood data

Criterion	Badfar et al. [15]		Saghafian et al. [25]	Current Study			
	EM	*FORK*		$nr = 1$	$nr = 2$	$nr^* = 4$	$nr = 6$
SSQ	280	280	534.0943	194.1718	186.6469	**167.0303**	271.3878
SAD	89	89	864	73.7901	71.7206	64.3682	86.0992
$MARE$	-	-	-	0.0203	0.0197	0.0169	0.0255
DPO	3.0	3.0	8.9	4.6214	4.88	5.3158	6.2463
$VarexQ$	-	-	-	99.5685	99.5852	99.6288	99.3669
R^2	-	-	-	0.9957	0.9959	0.9963	0.9940
KG	-	-	-	0.9963	0.9964	0.9965	0.9958

* Optimal

It should be noted that increasing the number of sub-reaches does not necessarily lead to improved accuracy. Therefore, the results for the optimal number of sub-reaches are also compared with those obtained from non-optimal subdivisions and the undivided (single-reach) case, as shown in Table 3 and Fig. 6. As detailed, the most accurate solutions correspond to the optimal number of sub-reaches (i.e., *nr* = 4). Interestingly, the worst results are not associated with the undivided case (*nr* = 1), but rather with the scenario involving the highest number of subdivisions (*nr* = 6). This outcome highlights the effectiveness of the proposed optimal dividing approach. Figure 6 further supports this conclusion, as the optimized multi-reach scenario shows a closer alignment with the observed flood data compared to the other methods.

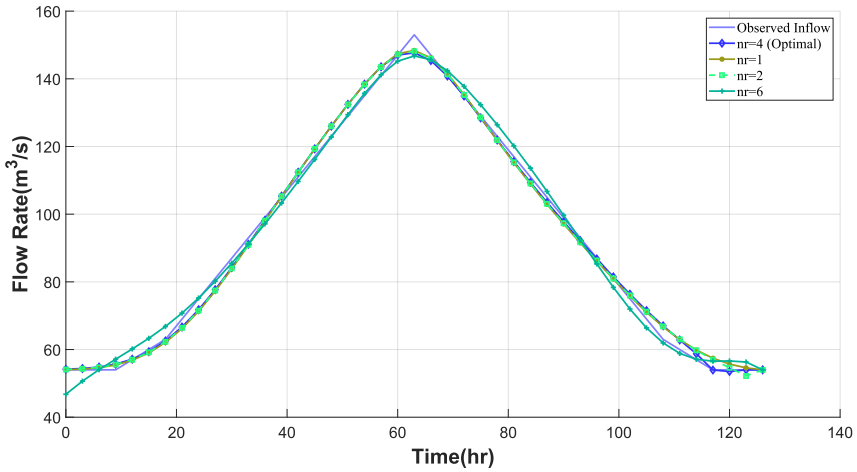


Figure 6. Comparison of routed inflow hydrographs for optimal and non-optimal sub-reach configurations, based on triangular flood data

3.2. Wilson flood data

Wilson flood represents one of the most important datasets, with extensive applications in the evaluation of flood routing models. It has been employed as a benchmark problem in many researches [26]. The dataset consists of 21 time steps (N=21), with each time step representing a 6-hour interval (Δt =6 hr).

The routing procedure was configured and executed for this flood event, and the multi-reach LMM parameters were subsequently obtained using the INFO. Fig. 7 indicates the INFO convergence process for the single-peak Wilson hydrograph data. The algorithm begins with an initial random solution and iteratively reduces the objective function (OF) value until it reaches the optimal solution.

Table 4 presents the optimized parameters obtained for both the single-reach and multi-reach cases, along with the corresponding optimal value of nr. Table 5 demonstrates the inverse-routed flood results compared to the observed upstream flood data. As shown, the obtained routing results exhibit a good agreement with the recorded flood values, highlighting the accuracy and reliability of the proposed method.

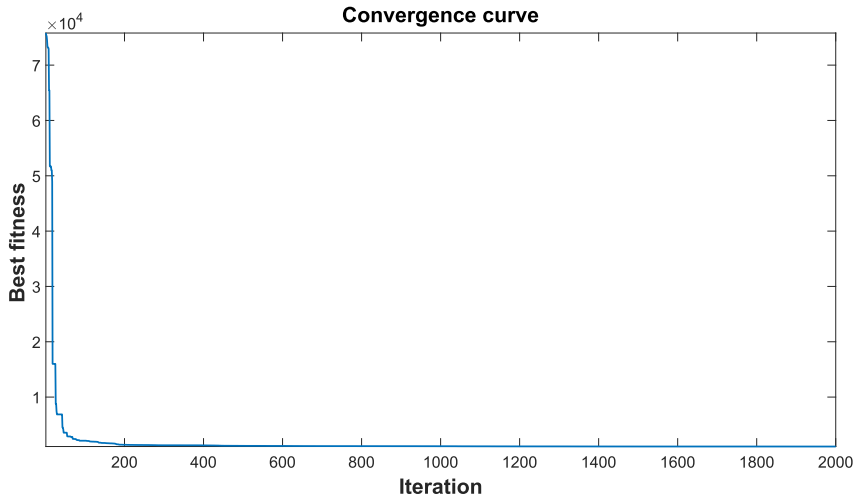


Figure 7. Convergence procedure of multi-reach Muskingum parameters by INFO algorithm for single-peak flood data (Wilson data)

Table 4. Optimal parameter values of single- and multi-reach LMM for the single-peak flood data (Wilson data)

Method	X	K (h)	β	nr
Single-reach	0.2403	15.7065	-0.023	-
Multi-reach	0.3542	23.84	-0.0042	9

Table 5. The results of the suggested inverse flood routing procedure for the single-peak hydrograph

	Observed hydrograph		Routed hydrograph
Time (hr)	Inflow (m^3/s)	Outflow (m^3/s)	Inflow (m^3/s)
0	22	22	23.70
6	23	21	14.74
12	35	21	44.17
18	71	26	75.86
24	103	34	97.27
30	111	44	106.53
36	109	55	105.89
42	100	66	98.58
48	86	75	87.60
54	71	82	75.18
60	59	85	62.85
66	47	84	51.54
72	39	80	41.70
78	32	73	23.51
84	28	64	26.98
90	24	54	22.02
96	22	44	18.51
102	21	36	16.33
108	20	30	15.44
114	19	25	15.81
120	19	22	17.55
126	18	19	18.00

Das [12] utilized this data for inverse flood routing by applying linear and non-linear Muskingum methods and minimized the difference between observed and calculated inflows. The inverse-routed flood hydrograph for the Wilson data, derived using the proposed method, was compared with the observed hydrograph and the results reported by Das [12] and Badfar et al. [15] (see Figure 8). As shown, the results closely match the observed data in terms of both peak value and timing of occurrence, whereas the results reported by Das [12] and Badfar et al. [15] show a lower peak value and a delayed peak time compared to the observed data.

Table 6 also compares the evaluation criteria of the suggested method with those of Das [12] and Badfar et al. [15] . The results indicate that the proposed method produced more accurate and reliable outcomes compared to the alternatives. Specifically, the SSQ value achieved by the INFO was reduced by 37% in undivided case compared to the models used in the study by Das [12] . Also, comparison the values of SAD and DPO criteria with those of Das [12] and Badfar et al. [15] , again shows the superiority of the proposed approach.

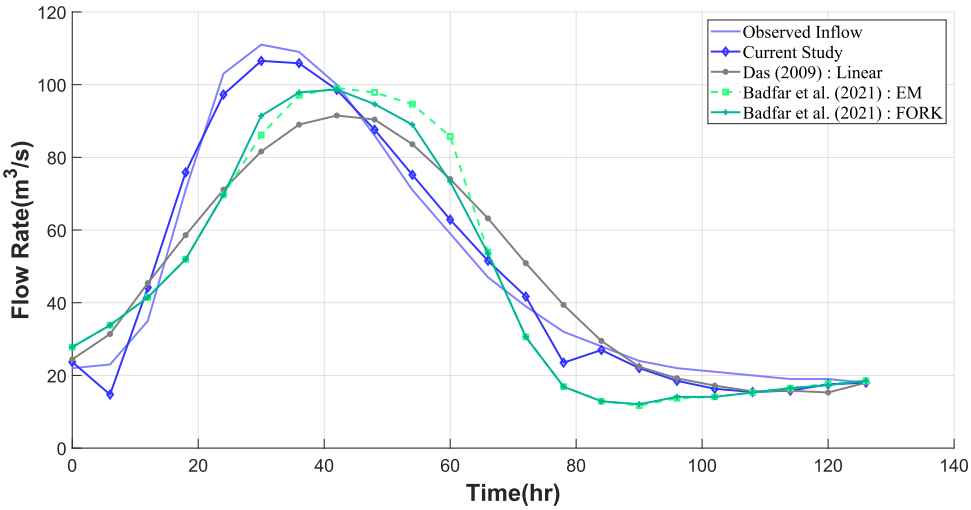


Figure 8. The routed inflow hydrograph in comparison with those of Das [12] and Badfar et al. [15] for the single-peak flood data (Wilson data)

Table 6. Muskingum methods evaluation criteria for the single-peak flood data (Wilson data)

Criterion	Badfar et al. [15]		Das [12]	Current Study			
	EM	*FORK*		*nr=1*	$nr = 7$	$nr^* = 9$	$nr = 11$
SSQ	2311	2237	3624	2301.947	1137.8618	**371.5487**	592.4724
SAD	190	184	212	180.0253	116.3485	70.0253	87.4099
$MARE$	-	-	-	0.414	0.1337	0.0908	0.1078
DPO	12.5	12.4	19.5	11.62	7.3719	0.96	1.2429
$VarexQ$	-	-	-	90.2348	95.1730	98.4238	97.4866
R^2	-	-	-	0.9043	0.9517	0.9843	0.9749
KG	-	-	-	0.9483	0.9706	0.9818	0.9793

Table 6 presents a comparison of the results based on single and multiple reach subdivisions. As shown, the optimal number of subdivisions for the Wilson data was found to be 9, leading to a reduction in the SSQ value by more than threefold compared to the undivided (single-reach) case. Moreover, the SSQ for this configuration is over 1.5 times lower than that for the 11-subdivision case. Figure 9 illustrates the flood routing results for the single-peak flood data, comparing the accuracy of the single-reach, non-optimal multi-reach, and optimal multi-reach (nr = 9) configurations. As shown, the routed flood in the optimized multi-reach configuration demonstrates a closer agreement with the observed flood compared to the other cases. This observation is further supported by the data in Table 6, where the SSQ and SAD values for the optimized multi-reach state are lower than those corresponding to the non-optimal number of subdivisions.

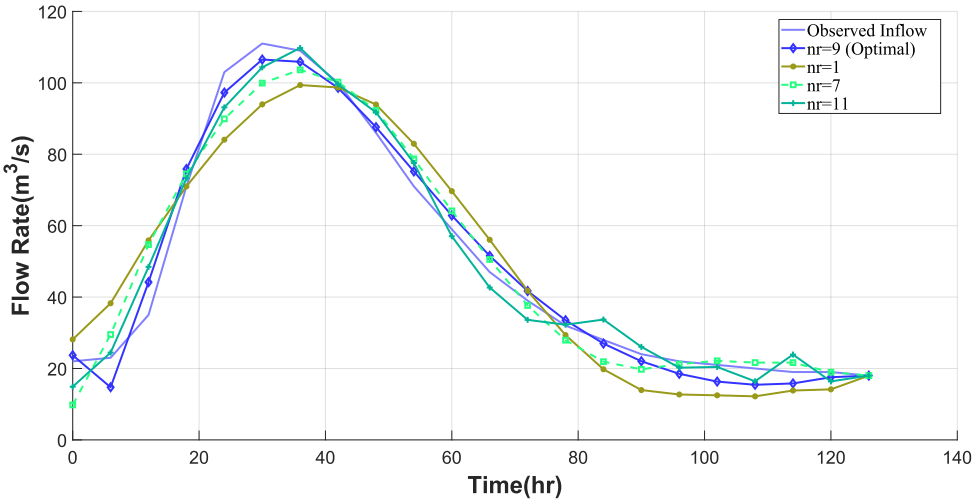


Figure 9. Comparison of routed inflow hydrographs for optimal and non-optimal sub-reach configurations, based on single-peak flood data (Wilson data)

3.3. Double-peak hydrograph

Saghafian et al. [25] investigated a double-peak hydrograph within a rectangular channel that measured 4,500 meters in length, had a top width of 50 meters, a bed slope of 0.01, and a Manning roughness coefficient of 0.025. This flood demonstrated a linear relation between storage volume and weighted flow [15]. In the reported data for this flood, the number of time steps is 25, and the length of each time step is 3 hours (N=25, $\Delta t = 3$).

Fig. 10 illustrates the convergence process of the INFO optimization algorithm for determining decision variables in multi-reach case for the double-peak hydrograph. As observed the algorithm initiates with a random starting solution and progressively minimizes the target function value, ultimately reaching an optimal solution. The parameters obtained from the optimization process in both single- and multi- reach cases, as well as the optimal value of nr are given in Table 7. Table 8 compares the inverse-routed inflow hydrograph with the observed one. As shown, there is strong agreement between the routed and recorded flood data, indicating a high level of accuracy in the proposed inverse flood routing process.

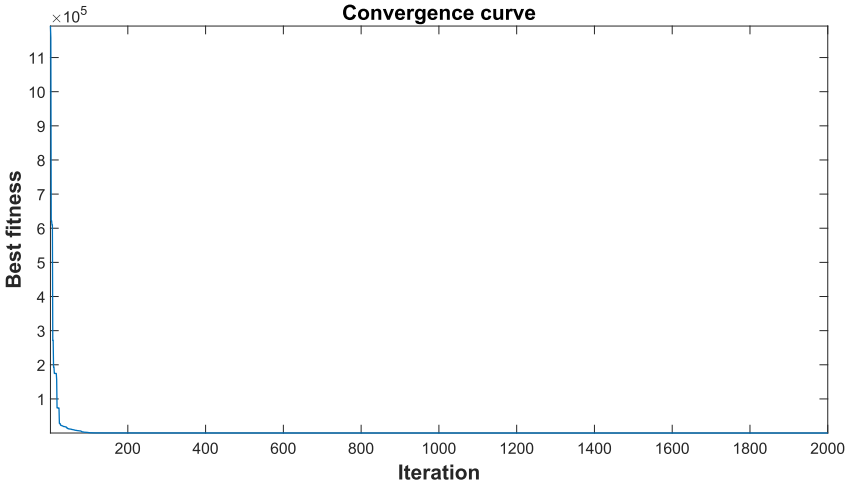


Figure 10. Convergence procedure of multi-reach Muskingum parameters by INFO algorithm for double peak flood data

Table 7. Optimal parameter values of single- and multi-reach LMM for the double-peak hydrograph

Method	X	K(h)	β	nr
Single-reach	0.1862	11.7351	0.034	-
Multi-reach	0.351	2.054	-0.0063	5

Table 8. The results of the suggested inverse flood routing procedure for the double-peak hydrograph

	Observed hydrograph		Routed hydrograph
Time (hr)	Inflow (m^3/s)	Outflow (m^3/s)	Inflow (m^3/s)
0	150	150	149.16
3	150	150	150.65
6	163.33	150.64	164.46
9	191.67	153.56	193.19
12	235	161.4	231.50
15	268.33	176.01	267.37
18	285.67	196.57	288.42
21	287	219.3	288.56
24	272.33	238.97	270.80
27	250	251.4	244.93
30	220	254.68	224.76
33	216.67	251.04	217.54
36	223.33	244.61	223.40
39	240	239.35	236.95
42	251.33	237.37	251.29
45	258	238.79	260.14
48	260	242.43	258.18
51	243.33	245.58	245.70
54	225	245.79	226.30
57	205	241.9	204.11
60	185	233.98	182.71
63	166.67	222.92	164.97
66	150	209.83	153.79
69	150	196.51	148.76
72	150	184.49	150.00

Saghafian et al. [25] employed the double-peak flood hydrograph data to validate their proposed method. They applied the kinematic wave method to simulate the upstream hydrograph, utilizing a time interval of three minutes. Figure 11 illustrates the inverse-routed flood hydrograph in comparison with the observed hydrograph and the results reported by Saghafian et al. [25]. As observed, the hydrograph presented by Saghafian et al. [25] exhibits several fluctuations, while the hydrograph generated using the proposed approach closely aligns with the observed hydrograph, particularly in terms of both the

magnitude and timing of the two observed peaks. In addition, the rising and recession limbs of both peaks in the routed hydrograph align closely with those of the observed hydrograph. The results are also compared with those of Badfar et al. [15] in Fig. 11, where double-peak flood data were used for inverse flood routing using the linear Muskingum method. As illustrated, the calculated inflow hydrograph demonstrates a closer match to the observed hydrograph than the one presented by Badfar et al. [15].

Further details of these comparisons, along with the evaluation criteria, are provided in Table 9. The results presented in this table show that the proposed methodology in this research provides more accurate and reliable outcomes compared with the other evaluated methods. Overall, it can be noted that the kinematic wave method by Saghafian et al. [25] exhibited the lowest level of accuracy, whereas the suggested method achieved the highest accuracy. The proposed model in the present study also exhibits improved performance in terms of the SSQ and SAD criteria when compared to the models of Saghafian et al. [25] and Badfar et al. [15]. Notably, the SSQ value was reduced by approximately 40% relative to the findings of Saghafian et al. [25] , and by about 15% compared to the results reported by Badfar et al. [15].

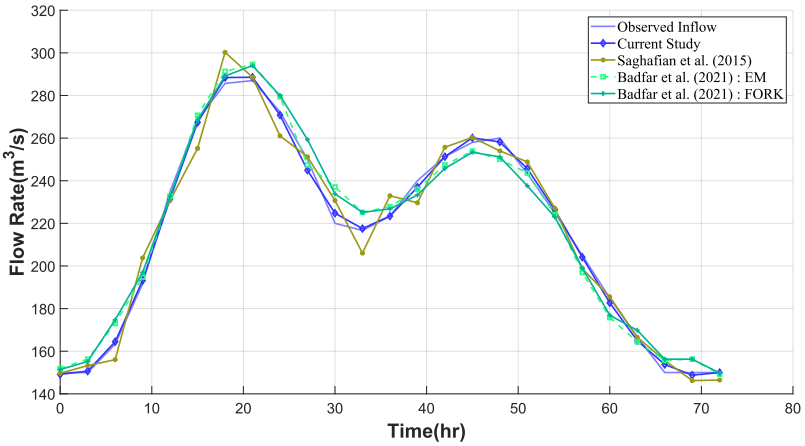


Figure 11. The routed inflow hydrograph in comparison with those of Saghafian et al. [25] and Badfar et al. [15] for the double-peak flood data

Table 9. Muskingum methods evaluation criteria for the double-peak flood data

Criterion	Badfar et al. [15]		Saghafian et al. [25]	Current Study			
	EM	*FORK*		$nr = 1$	$nr = 3$	$nr^* = 5$	$nr = 7$
SSQ	967	967	1368	823.463	310.5111	**128.6247**	642.3044
SAD	124	124	858	118.8228	72.6080	45.8292	98.5738
$MARE$	-	-	-	0.0216	0.0133	0.0086	0.0202
DPO	7.6	7.6	45.6	4.9376	5.7623	1.566	1.7782
$VarexQ$	-	-	-	98.4287	99.4075	99.7545	98.7744
R^2	-	-	-	0.9844	0.9942	0.9975	0.9878
KG	-	-	-	0.9881	0.9905	0.9909	0.9891

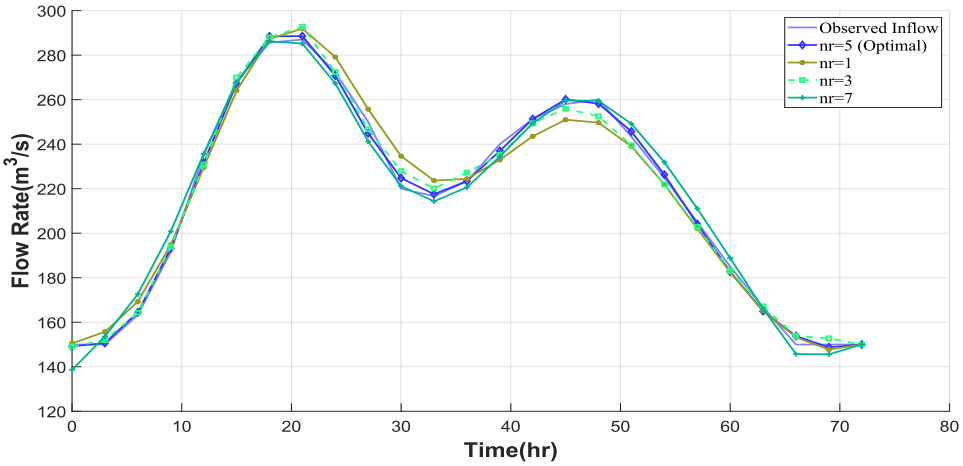


Figure 12- Comparison of routed inflow hydrographs for optimal and non-optimal sub-reach configurations, based on double-peak flood data

Figure 12 presents the results of flood routing using the single-reach LMM, along with the optimized and unoptimized multi-reach LMM, applied to the double-peak flood data. As shown, the routed hydrograph in the optimized multi-reach case aligns more closely with the observed flood compared to the other configurations. This observation is further supported by the SSQ and other evaluation criteria values presented in Table 9. As described, a significant reduction in the SSQ value was observed when $nr = 5$, the identified optimal number of sub-reaches.

3.4. Additional insights

This section examines the impact of the number of subdivisions on model performance across different examples. Figure 13 presents the variation of the SSQ value relative to the optimal configuration for the triangular flood hydrograph, Wilson flood data, and the double-peak flood hydrograph, as a function of the number of subdivisions. Among these, the triangular flood hydrograph exhibits the smallest increase in SSQ when the number of subdivisions deviates from the optimal value, compared to the other two cases.

For the triangular flood hydrograph, the response to changes in the number of sub-reaches is notably asymmetric (Figure 13). When the number of sub-reaches is below the optimal value, the SSQ increases moderately—by up to 16% for $nr = 1$. In contrast, exceeding the optimal number leads to a substantial rise, with the SSQ increasing by as much as 233% at $nr = 8$. This highlights two key insights: first, increasing the number of sub-reaches does not necessarily improve model accuracy, contrary to common assumptions; and second, the model exhibits lower sensitivity to the number of subdivisions when fewer sub-reaches are used.

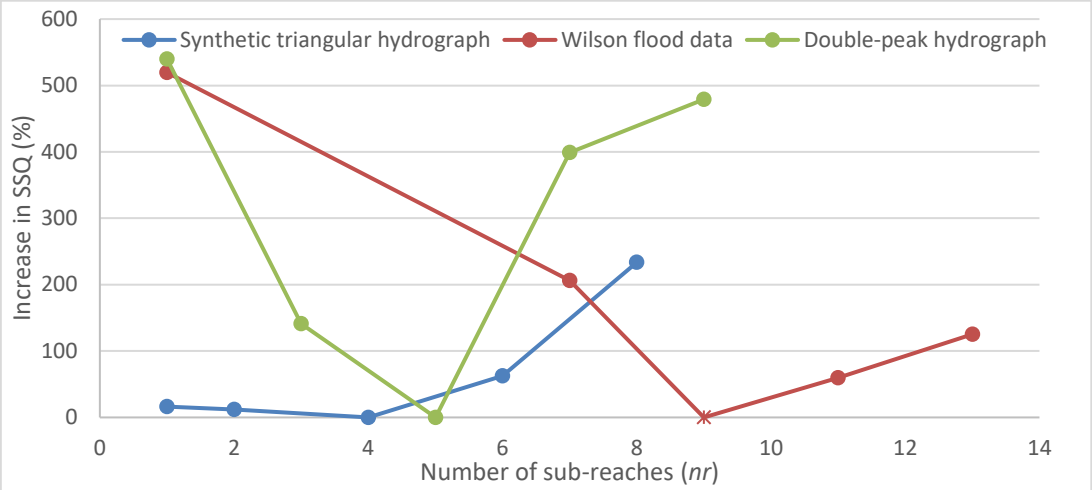


Figure 13. Percentage of increase in SSQ relative to optimal nr with varying the number of subdivisions in the three flood hydrograph cases

For the Wilson flood data, the variation in SSQ is also asymmetric; however, the increase in SSQ is more pronounced when the number of sub-reaches is less than the optimal value, compared to when it is greater than the optimal. Specifically, the SSQ increases by up to 520% for suboptimal subdivisions and by approximately 125% for over optimal subdivisions. This indicates that applying a single-reach LMM to the Wilson flood data results in significant inaccuracy relative to the optimal number of sub-reaches, and overall, this flood case is highly sensitive to the chosen subdivision level.

In the case of the double-peak flood data, the SSQ variations are nearly symmetric, with increases reaching up to 500%. This demonstrates that the double-peak flood is also highly sensitive to the number of sub-reaches selected for the proposed multi-reach LMM flood routing procedure.

4. Conclusion

In this study, a multi-reach Linear Muskingum Model (LMM) was employed for inverse flood routing, aiming to reconstruct the upstream inflow hydrograph based on downstream flow data. To estimate the parameters of the multi-reach LMM, the weighted mean of vectors (INFO) algorithm—a powerful meta-heuristic optimization technique—was utilized. Two strategies were adopted to enhance routing accuracy: (1) the contribution of lateral flow along the river was incorporated, and (2) the number of sub-reaches was treated as a decision variable and estimated alongside other model parameters.

The proposed multi-reach LMM integrated with INFO was tested using three distinct flood hydrographs: a triangular flood hydrograph, the Wilson flood data, and a double-peak flood hydrograph. The results were compared with those from previous studies. Even in the single-reach case, the proposed approach demonstrated higher accuracy across the three flood scenarios. When the number of sub-reaches was also optimized, the improvement became more significant; for example, in the double-peak case, the SSQ value was reduced by more than six times compared to the single-reach (no subdivision) state. Other evaluation metrics consistently confirmed the superior performance and robustness of the proposed method. Additionally, the analysis showed that the double-peak flood hydrograph is the most sensitive to the number of sub-reaches, whereas the triangular flood is the least sensitive. In conclusion, the developed multi-reach LMM with INFO proves to be an effective and reliable tool for inverse

flood routing. Future work could explore its application using a nonlinear Muskingum model to further enhance modeling capabilities.

Funding statement:
This research received no external funding.

Conflict of Interest:
The authors declare that they have no conflict of interest.

AI Statement:
During the preparation of this work the author used check spelling tools in order to grammar correct. After using this tool, the author reviewed and edited the content as needed and takes full responsibility for the content of the publication.

Author Contributions:
All authors contributed to the study conception and design. Material preparation, data collection, and analysis ... were performed by M. R., A. R., and H. Z. The first draft of the manuscript was written by M. R., A. R., and H. Z. The author reads and approved the final manuscript.

References
1. Suerich-Gulick F, Gaskin SJ, Villeneuve M, Parkinson É. Characteristics of free surface vortices at low-head hydropower intakes. Journal of Hydraulic Engineering. 2014 Mar 1;140(3):291-9. https://doi.org/10.1061/(ASCE)HY.1943-7900.0000826
2. Knauss J, editor. Swirling flow problems at intakes. Routledge; 2017 Nov 1.
3. Rankine WJ. A manual of applied mechanics. C. Griffin and Company, Limited; 1901.
4. Hecker GE, editor. Fundamentals of vortex intake flow. IAHR hydraulic structures design manual. Rotterdam: Balkema, [chapters 2 and 8]. 1987.
5. Sarkardeh H, Zarrati AR, Roshan R. Effect of intake head wall and trash rack on vortices. Journal of Hydraulic Research. 2010 Feb 1;48(1):108-12. https://doi.org/10.1080/00221680903565952
6. White F. Fluid Mechanics (5th ed.). New York, NY: McGraw-Hill. 2003.
7. Travis QB, Mays LW. Prediction of intake vortex risk by nearest neighbors modeling. Journal of Hydraulic Engineering. 2011 Jun 1;137(6):701-5. https://doi.org/10.1061/(ASCE)HY.1943-7900.0000344
8. Heravi Z, Azhdary Moghaddam M, Esmaili K, Givehchi M, Bahr Peyma A. Experimental Evaluation of Performance of the New Design of Bed Protection Models (F-jacks) in Altering the Flow Pattern around Bridge Piers. Journal of Hydraulics. 2024 Mar 20;19(1):67-86. https://doi.org/10.30482/jhyd.2023.395247.1643
9. Camnasio E, Orsi E, Schleiss AJ. Experimental study of velocity fields in rectangular shallow reservoirs. Journal of Hydraulic Research. 2011 Jun 1;49(3):352-8. https://doi.org/10.1080/00221686.2011.574387
10. Sarkardeh H, Jabbari E, Zarrati AR, Tavakkol S. Velocity field in a reservoir in the presence of an air-core vortex. InProceedings of the Institution of Civil Engineers-Water Management 2014 Jun;167(6):356-64. Thomas Telford Ltd. https://doi.org/10.1680/wama.13.00046
11. Mulligan S, Casserly J, Sherlock R. Effects of geometry on strong free-surface vortices in subcritical approach flows. Journal of Hydraulic Engineering. 2016 Nov 1;142(11):04016051. https://doi.org/10.1061/(ASCE)HY.1943-7900.0001194
12. Naderi V, Gaskin S. A 3D study of an intake air-core vortex structure using PIV & flow visualization. In: Proc of 7th International Symposium on Hydraulic Structure. 2018: Aachen, Germany.
13. Naderi V, Farsadizadeh D, Lin C, Gaskin S. A 3D study of an air-core vortex using HSPIV and flow visualization. Arabian Journal for Science and Engineering. 2019 Oct;44(10):8573-84. https://doi.org/10.1007/s13369-019-03764-3
14. Duinmeijer A, Oldenziel G, Clemens F. Experimental study on the 3D-flow field of a free-surface vortex using stereo PIV. Journal of Hydraulic research. 2020 Jan 2;58(1):105-19. https://doi.org/10.1080/00221686.2018.1555558
15. Hamidi, S., Sarkardeh, H., Bashtani, A. Spiral Flow Measurement at Vertical Intakes Using PTV Method. Journal of Hydraulic Structures, 2024; 11(1): 41-50. doi: 10.22055/jhs.2024.47215.1304

16. Azarpira M, Sarkardeh H, Tavakkol S, Roshan R, Bakhshi H. Vortices in dam reservoir: A case study of Karun III dam. Sadhana. 2014 Oct;39(5):1201-9. https://doi.org/10.1007/s12046-014-0252-7
17. Amiri SM, Zarrati AR, Roshan R, Sarkardeh H. Surface vortex prevention at power intakes by horizontal plates. InProceedings of the institution of civil engineers-water management 2011 Apr;164(4):193-200. Thomas Telford Ltd. https://doi.org/10.1680/wama.1000009
18. Khanarmuei M, Rahimzadeh H, Sarkardeh H. Investigating the effect of intake withdrawal direction on critical submergence and strength of vortices. Modares Mechanical Engineering. 2015;14(10):35-42.
19. Khanarmuei MR, Rahimzadeh H, Kakuei AR, Sarkardeh H. Effect of vortex formation on sediment transport at dual pipe intakes. Sādhanā. 2016 Sep;41(9):1055-61. https://doi.org/10.1007/s12046-016-0531-6
20. Khanarmuei M, Rahimzadeh H, Sarkardeh H. Effect of dual intake direction on critical submergence and vortex strength. Journal of Hydraulic Research. 2019 Mar 4;57(2):272-9. https://doi.org/10.1080/00221686.2018.1459896
21. Monshizadeh M, Tahershamsi A, Rahimzadeh H, Sarkardeh H. Comparison between hydraulic and structural based anti-vortex methods at intakes. The European Physical Journal Plus. 2017 Aug 3;132(8):329. https://doi.org/10.1140/epjp/i2017-11608-4
22. Monshizadeh M, Tahershamsi A, Rahimzadeh H, Sarkardeh H. Vortex dissipation using a hydraulic-based anti-vortex device at intakes. International Journal of Civil Engineering. 2018 Sep;16(9):1137-44. https://doi.org/10.1007/s40999-017-0266-8
23. Taghizadeh A, Sarkardeh H, Azamathulla HM. Mechanisms of free surface vortex formation at water intakes (a review). Dams and Reservoirs. 2025 Sep 11. https://doi.org/10.1680/jdare.25.01007
24. Amini AA, Sarkardeh H, Jabbari E, Eidi A. Understanding vortex characteristics in hydraulic systems: a temperature-driven analysis. Modeling Earth Systems and Environment. 2024 Jun;10(3):3559-71. https://doi.org/10.1007/s40808-024-01969-6
25. Zhang B, Ma L, Cheng L, Zhu B, Qin Y. Characterization of free-surface vortex evolution and its impact on hydraulic stability of the pump sump. Experimental Thermal and Fluid Science. 2025 Jul 1;166:111466. https://doi.org/10.1016/j.expthermflusci.2025.111466
26. Jiao W, Fan H, Xi X, Shen J, Zhou L, Jia X, Wang Z, Cheng L. Study on the key influencing factors and vortex characteristics of the water jet propulsion pump underwater suction vortex. Physics of Fluids. 2025 Sep 1;37(9). https://doi.org/10.1063/5.0287735
27. Mondal RK, Rohilla L, Kumar P. Free surface vortex and associated air entrainment during liquid drainage using two outlets. Experimental Thermal and Fluid Science. 2025 Jan 1;160:111314. https://doi.org/10.1016/j.expthermflusci.2024.111314
28. Roushangar K, Akhgar S, Salmasi F, Shiri J. Modeling energy dissipation over stepped spillways using machine learning approaches. Journal of Hydrology. 2014 Jan 16;508:254-65. https://doi.org/10.1016/j.jhydrol.2013.10.053
29. Ghorbani MA, Salmasi F, Saggi MK, Bhatia AS, Kahya E, Norouzi R. Deep learning under H2O framework: A novel approach for quantitative analysis of discharge coefficient in sluice gates. Journal of Hydroinformatics. 2020 Nov 1;22(6):1603-19. https://doi.org/10.2166/hydro.2020.003
30. Ghorbani MA, Khatibi R, Singh VP, Kahya E, Ruskeepää H, Saggi MK, Sivakumar B, Kim S, Salmasi F, Hasanpour Kashani M, Samadianfard S. Continuous monitoring of suspended sediment concentrations using image analytics and deriving inherent correlations by machine learning. Scientific reports. 2020 May 22;10(1):8589. https://doi.org/10.1038/s41598-020-64707-9
31. Salmasi F, Abraham J. Expert system for determining discharge coefficients for inclined slide gates using genetic programming. Journal of Irrigation and Drainage Engineering. 2020 Dec 1;146(12):06020013. https://doi.org/10.1061/(ASCE)IR.1943-4774.0001520
32. Salmasi F, Sihag P, Abraham J, Nouri M. Experimental investigation and prediction of free fall jet scouring using machine learning models. International Journal of Sediment Research. 2023 Jun 1;38(3):405-20. https://doi.org/10.1016/j.ijsrc.2022.11.004

33. Anwar HO, Weller JA, Amphlett MB. Similarity of free-vortex at horizontal intake. Journal of Hydraulic Research. 1978 Apr 1;16(2):95-105. https://doi.org/10.1080/00221687809499623
34. Liu FT, Ting KM, Zhou ZH. Isolation forest. In2008 eighth ieee international conference on data mining 2008 Dec 15 (pp. 413-422). IEEE. https://doi.org/10.1109/ICDM.2008.17
35. Manevitz LM, Yousef M. One-class SVMs for document classification. Journal of machine Learning research. 2001;2(Dec):139-54.
36. Bushra AA, Yi G. Comparative analysis review of pioneering DBSCAN and successive density-based clustering algorithms. IEEE Access. 2021 Jun 14;9:87918-35. https://doi.org/10.1109/ACCESS.2021.3089036
37. Cea L, Puertas J, Pena L. Velocity measurements on highly turbulent free surface flow using ADV. Experiments in fluids. 2007 Mar;42(3):333-48. https://doi.org/10.1007/s00348-006-0237-3

© 2025 by the authors. Licensee SCU, Ahvaz, Iran. This article is an open access article distributed under the terms and conditions of the Creative Commons Attribution 4.0 International (CC BY 4.0 license) (http://creativecommons.org/licenses/by/4.0/).

Appendix A. Derivation of the Inverse Muskingum Routing Equation with Lateral Flow

Discretizing Eq. (1) over a time interval Δt using a weighted scheme gives:

$$\frac{S_2 - S_1}{\Delta t} = (1+\beta)[(1-\theta)I_1 + \theta I_2] - [(1-\theta)O_1 + \theta O_2] \tag{A1}$$

The storage values at the beginning and end of the time step are obtained from Eq. (2):

$$S_2 = K[X(1+\beta)I_2 + (1-X)O_2] \tag{A2}$$
$$S_1 = K[X(1+\beta)I_1 + (1-X)O_1] \tag{A3}$$

Substituting Eqs. (A2) and (A3) into Eq. (A1) and rearranging terms yields:

$$\frac{K[X(1+\beta)I_2 + (1-X)O_2] - K[X(1+\beta)I_1 + (1-X)O_1]}{\Delta t} = (1+\beta)[(1-\theta)I_1 + \theta I_2] - [(1-\theta)O_1 + \theta O_2] \tag{A4}$$

Solving for the unknown upstream inflow I_1 results in the inverse routing equation:

$$I_1 = C_1 O_2 + C_2 O_1 + C_3 I_2 \tag{A5}$$

where the coefficients are defined as:

$$C_1 = \frac{1}{1+\beta}\frac{K(1-X) + \theta\Delta t}{KX + (1-\theta)\Delta t}$$
$$C_2 = \frac{-1}{1+\beta}\frac{K(1-X) - (1-\theta)\Delta t}{KX + (1-\theta)\Delta t} \tag{A6}$$
$$C_3 = \frac{KX - \theta\Delta t}{KX + (1-\theta)\Delta t}$$

This formulation enables inverse flood routing while explicitly accounting for lateral flow contributions through the parameter β.

Adverse Effects of Repeated Deep Drawdown and Re-impounding Cycles on the Clay Core of Earth Dams; a case study of the Karkheh Dam

Masoud Oulapour [*,1], Sepideh Joulanejad [1] , Arash Adib [1]

1. Deptartment of Civil Engineering, Faculty of Civil Engineering and Architecture, Shahid Chamran University of Ahvaz, Ahvaz, Iran.

***Corresponding Author:**
Masoud Oulapour,

Email: Oulapour_m@scu.ac.ir
Received: 2025.12.08
Accepted: 2026.01.29
J. Hydraul. Struct., 2025; 12(3):94-114
DOI: 10.22055/jhs.2026.51342.1370

ABSTRACT

In this study a method is proposed for investigation the effects of reservoir water-level fluctuations which results in wetting and drying cycles (WDC) in parts of the dam body. The WDC adversely affect the mechanical behavior of material in those parts, especially in semi-arid climatic areas, such as Iran. The degradation pattern of tested specimens is used for updating the material behaviour in numerical simulations of the Karkheh earth dam, located south-west of Iran. First the results of unconfined compressive strength (UCS) tests were simulated for calibration of the degradation pattern. Next, a sensitivity analysis was performed on the parameters affecting the UCS, which showed that cohesion is more effective than elastic modulus or friction angle. The degradation rates at each cycle were applied to the properties of dam core materials according to the WDC. The calculated vertical and horizontal displacements of the dam were compared to the recorded data, based on the reservoir level, for the period of 17 years and in two cases of either including the material degradation or ignoring that. The results showed that considering the material degradation makes a difference in deformations growing up to about 10 %. Considering the magnitude and importance of deformations, this is a significant impact. Also, a series of simulations were conducted based on maximum and minimum permissible water level assumed for the next 7 years in both cases. The results showed that ignoring the degradation can result in up to 20% under estimating of the deformations. The results emphasize the necessity of further research on the subject.

KEYWORDS

Embankment dams, Deep Drawdown, Drying-Wetting Cycles, Compressive Strength, Permeability Increase.

1. Introduction

Extensive research has been conducted on the effects of saturation and drying on compacted clay soils. The outcomes of these studies cover a wide range of factors, including the influence of the number of WDC, the quality of the soil, and the initial moisture content. Moreover, several investigations have examined the variations in soil strength parameters caused by loading and unloading cycles that occur during rapid wetting and drainage processes. However, these studies have not addressed the problem in the context of an embankment dam and its clay core. The previous research has primarily focused on the behavior of compacted clay soils—such as changes in permeability, cracking, swelling, and strength reduction—considered individually and solely as a result of WDC.

In contrast, the present study aims to analyze and model the combined effects of WDC, loading–unloading processes, and the nonlinear behavior of compacted clay soils. Salehian-Dastjerdi and Hemmat [6] concluded that the application of successive WDC on a low-plasticity clay sample leads to a reduction in shear strength and an increase in the soil's internal friction angle. de Costa et al. [7] through studies conducted on agricultural soils in the state of Ceará, Brazil, found that repeated WDC due to irrigation reduces the soil's porosity. Rogers [8], as cited in Kholghifard et al. [9], demonstrated that repeated WDC on silt soil not only increase the swelling potential but also decrease the shear strength of the soil. Wang and Wei [10] concluded that the pore structure of soil changes under WDC. The variations in micropores were found to be reversible, whereas macropore changes were irreversible. Kampala et al. [11], by adding carbide to a silt soil sample and subjecting it to WDC, found that the soil's strength behavior improved under such cyclic conditions. Goh et al. [12], using a triaxial test on soil samples subjected to WDC, reported that the soil exhibited lower strength during the wetting phase compared to the drying phase. They also noted that the most significant changes in soil strength occurred during the first cycle. Shi et al. [13] investigated the effect of wetting duration in successive WDC on soil strength behavior. Their findings indicated that longer wetting periods led to a reduction in soil strength. Naramitkornburee et al. [14], through Unconfined Compressive Strength (UCS) tests on cement-stabilized soil samples exposed to successive WDC, concluded that such cycles reduce the compressive strength of the soil. Du et al. [15] examined the compressive strength of magnesium-stabilized soil samples under WDC and found that successive cycles lead to a decrease in compressive strength, with the reduction being directly proportional to the number of WDC.

Naini et al. [16] studied the bearing capacity and UCS of a low-plasticity clay subjected to repeated wetting and drying. Their results revealed that the cycles cause a decrease in both parameters, and that the bearing capacity and compressive strength are lower during the wetting phase than during drying. Wang and Hu [17] examined the effect of rapid WDC on soil aggregate stability. Based on their findings, rapid cycles reduced aggregate diameter and consequently decreased aggregate stability. Sayem et al. [18] investigated the strength behavior of soils subjected to successive WDC using consolidated drained (CD) triaxial tests. Their results showed that both cohesion and internal friction angle decreased with cycling, and that from the fourth cycle onward, the reduction in

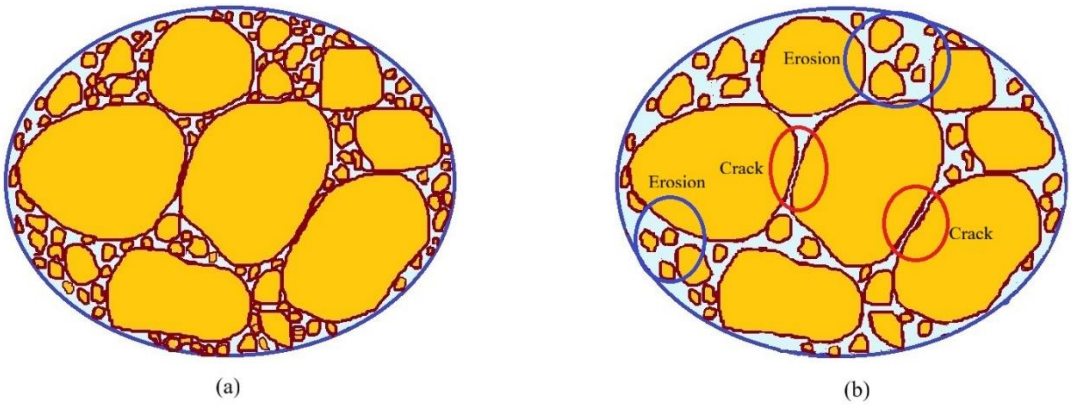


Figure. 1 Configuration of a compacted soil: (a) after compaction; (b) after WDC.

strength became nearly constant, indicating a stabilized behavior. Tang et al. [19] assessed soil strength under repeated wetting and drying using cone penetration tests and found that an increase in the number of cycles caused a reduction in soil strength, with the largest reduction occurring during the first cycle. Wang et al. [20] investigated a low-plasticity clay subjected to WDC and found that soil strength increased during drying, while the internal friction angle decreased. Akcanca and Aytekin [21] reported that lime addition to bentonite clay reduces its hydraulic conductivity. Gallage et al. [22] examined the influence of repeated wetting and drying on soil hydraulic conductivity and found that conductivity during drying was greater than during wetting. De Camillis et al. [23] also investigated the effect of repeated wetting and drying on soil hydraulic conductivity and found a significant increase in hydraulic conductivity with the number of cycles. Rosone et al. [24], based on lab tests on samples extracted from an in-situ embankment, found the mutual connection between hydraulic behavior (WDC and suction) and mechanical behavior such as strength, stiffness, and volumetric strains. Liu et al. [25], by applying WDC to a low-plasticity clay, concluded that successive cycles reduce shear strength while increasing the hydraulic conductivity of the clay. Luo et al. [26] indicated that with the increasing number of WDC, the relationships between shear stress and shear displacement have a tendency of transiting from strain-hardening to strain-softening type, and the greater number of WDC, the more significant signs of strain-softening. Also, that the shear strength parameters decreased first and then fluctuated slightly and irregularly near a certain value with the increase in the number of WDC. Ma et al. [27] investigated compacted low-plasticity clay subjected to controlled hydraulic WDC and observed that cyclic moisture fluctuations weakened water retention capacity, caused irreversible swelling–shrinkage deformation, and reduced the small-strain shear modulus by up to 35%. The soil progressively transitioned from a dense to a looser state, implying potential long-term instability of compacted embankments. Similarly, Cuisinier and Masrouri [28] examined lime- and cement-stabilized silty soils exposed to up to twelve WDC using both oven-drying and controlled-humidity protocols. Their results showed that repeated cycles caused marked reductions in UCS and increases in hydraulic conductivity, with degradation more severe under high-temperature drying due to leaching and microstructural damage. Cement treatment offered greater durability than lime, but both displayed substantial performance loss after several cycles. Complementarily, Sabatino et al. [29] reported that lightweight cemented soils also suffer stiffness and strength degradation after WDC, particularly under high relative humidity, as suction variations induce cement bond destruction. The amplitude of suction change and porosity level governed the extent of mechanical weakening. Collectively, these studies demonstrate that WDC trigger cumulative degradation of strength, stiffness, and hydraulic properties in compacted or cemented clayey soils, underscoring the necessity to incorporate environmental cyclic effects in the long-term design and durability assessment of geotechnical infrastructures. Estabragh et al. [30] studied swelling-shrinkage behavior of a compacted expansive soil (mixture of bentonite and kaolin) under WDC. It was concluded that the initial water content and compaction level significantly influence the volumetric behavior. Also, soils on the dry side of the optimum moisture content exhibit higher swelling potential. Cyclic wetting and drying significantly alter soil fabric through microstructural evolution, aggregate rearrangement, and pore network modification. Repeated shrink–swell processes induce crack formation, dissolution of interparticle bonds, and redistribution of fine particles, leading to changes in void ratio and pore size

distribution [31] [32] [33] [34]. Researchers have developed advanced constitutive models to better simulate the complex behavior of compacted clayey soils under cyclic wetting and drying [27, 35]. These models incorporate factors like suction (matric potential), void ratio, and stress history to predict the volume change and mechanical behavior of the soil. Periodic changes in the reservoir water level produce fluctuating hydraulic loadings on the soils imposes hydraulic loadings on slopes. In recent years, the effect of hydraulic fluctuation on suffusion has been emphasized. Prasomsri and Takahashi [36], Deng et al. [37], Wang et al. [38], Fu et al. [39] conducted different suffusion tests under various hydraulic fluctuations. The experimental results showed that hydraulic fluctuations could significantly promote the erosion process of internally unstable soil by increasing the fine particle eroded mass and hydraulic conductivity. Deng et al. [40] used finite element method and a suitable constitutive model, treated the unsaturated soil as a five-constituent mixture, by which both erosion and deposition could be captured by phase transition between deposition and fluidization of fines. The fines redistribution in the slope was modeled and the erosion was quantified based on the frequency of water level fluctuation. The numerical results indicated that a higher fluctuation frequency could promote fine particle loss in the zones near the slope surface, consequently inducing greater deterioration in the slope stability.

Liu et al. [41] studied the deformations of a dam body and analyzed how water levels fluctuations caused settlement deformation of the dam body. With the rise in the reservoir water level, the longitudinal cracks on the dam crest showed opening when the reservoir water level dropped. The fluctuation of the settlement deformation shows that the upstream side was larger than the downstream side, especially during the period of abrupt change in reservoir water level. Studies have also indicated that there is a progressive development to the plastic shear strain zone within the slope as the number of water level variation cycles is increased, and the change in the seepage field is closely related to the water level variations [42,43]. Chen et al. [44] investigated the effect of the shape of landslide slip surfaces and soil permeability on slope stability during reservoir fluctuating water level changes in the Three Gorges Reservoir area using numerical methods. It was indicated that line-shaped slopes with low permeability are most prone to instability, while chair-shaped slopes with high permeability are most stable. Also, as the water level drops, the slope's safety factor decreased initially and then increases.

Finite element analyses along with physical model experiments indicated that the safety factor, when the water level drops rapidly, is generally slightly lower than the safety factor when the upstream water level rises rapidly [45,46, 47].

A brief review of the previous studies clearly displays the need for assembling these studies in the context of structural analysis of the dam body, as these studies has only been performed on the specimens. The issues like the effect of size of the dam and its boundary conditions and the severity of the climate change, such as the duration of draught and rain intensity, need to be addressed, too [48, 49]. Also, the complex micromechanics of the soil under such hydromechanical loading path is too complex to be addressed here. Therefore, this study has been confined to a macro scale analysis of a dam based on micromechanics of the specimens.

Karkheh dam is a strategic infrastructure of southwest part of the country. Its huge dimensions make it a necessity to predict any possible problem in its performance. In this study, considering the latest waves of drought period, the long-term effects of the fluctuations of water level in the reservoir of Karkheh dam on the deformations of the impervious core is studied. The degradation of the compacted core due to WDC is included in this research.

2. Materials and methods

As this research is a numerical study on previously collected data, a brief discussion on numerical method and its details are presented here. Also, the data used in this research has been partly reported in earlier studies and partly has been obtained from the government agencies. The creative method of using the collected data, based on similarity of the effect of wetting and drying process on similar materials, has been discussed here.

2.1 Finite Element Method

The softwares developed based on finite element method, such as SIGMA/W, use a partial differential equation which depends on the type of problem under study. The coupled problems involving simultaneous solution of equilibrium and flow equations are formulated based on combination of linear momentum balance (eqn. 1) and fluid mass conservation (eqn. 2):

$$\nabla \cdot \sigma + \rho g = 0 \quad with\ \sigma = \sigma' - \alpha p I \qquad (1)$$

where σ is total stress, σ' is effective stress, p is pore pressure, α is Biot's coefficient (≈1 for most soils), ρ is density, and g is gravitational acceleration.

$$\frac{\partial}{\partial t}(\alpha \nabla \cdot \mathrm{u} + \mathrm{S} \cdot p) + \nabla \cdot q = Q \qquad (2)$$

where u is the displacement, S is the storage coefficient, q is Darcy flux, and Q is an external source/sink. The Darcy's law is defined as:

$$q = -k \cdot \nabla p \qquad (3)$$

where k is hydraulic conductivity. The effective stress-strain relationship for nonlinear materials is:

$$\Delta\sigma' = D_{tan}\,\Delta\varepsilon \qquad where\ \varepsilon = {}^{1}/_{2}(\nabla u + \nabla u^{T}) \qquad (4)$$

Here, D_{tan} is the calculated based on the constitutive equation of solid structure updated at each iteration. This constitutive equation can be any complex nonlinear elastoplastic model.

In general, the basic objective in a nonlinear analysis is to find the state of equilibrium of a body corresponding to the externally applied loads. In an incremental load formulation, these loads are a function of time, and at time t the nonlinear equilibrium problem can be formulated as a solution of the equation (5):

$$\{\psi^t\} = \{R(a)^t\} - \{\mathrm{F}^t\} = 0 \qquad (5)$$

where $\{\psi\}$ is the nodal unbalanced/residual forces, {F} is the externally applied nodal forces, {R} is nodal forces equivalent to element stresses, and, a is the nodal displacements. Due to equilibrium, at each stage i the eqn. (5) can be written as equation (6):

$$[K_i]\{\Delta u_i\} = \{\Delta F_i\} - \{F_{int,i-1}\} \qquad (6)$$

where: $[K_i]$ stands for stiffness matrix for the currently active elements, $\{\Delta u_i\}$ is incremental displacements, $\{\Delta F_i\}$ is applied load increment, $\{F_{int,i-1}\}$= internal forces from previous stage. In coupled systems the equilibrium at each step can be written as:

$$\begin{bmatrix} K_{uu} & K_{up} \\ K_{pu} & K_{pp} \end{bmatrix} \begin{bmatrix} \Delta \mathrm{u} \\ \Delta p \end{bmatrix} = \begin{bmatrix} R_u \\ R_p \end{bmatrix} \qquad (7)$$

where p is the vector of nodal pore pressure and u stands for the vector of the nodal displacements. K_{uu} represents the structural stiffness, *Kup* and *Kpu* represent coupling between pore pressure and deformation, and *Kpp* contains hydraulic conductivity and storage terms. Implementation of boundary conditions and their changes are conducted at the beginning each new stage.

2.2 Staged Construction simulation method

Staged construction analysis is a specialized simulation technique used to model how a structure or system is built up over time (in

"stages"), rather than assuming the entire structure exists and is loaded all at once. This is critical for geotechnical and civil engineering problems (e.g. embankments, tunnels, dams, or buildings) where stress history and construction sequence strongly influence behavior. The core concept in this analysis is simulating the actual sequence of material placement, excavation, or load application by using activating and deactivating elements, boundaries, or loads in a time-dependent or stepwise manner. At each construction stage new elements representing added material (like a new soil layer, concrete pour, or embankment lift) are activated and removed elements representing excavated material are deactivated. In order to deactivate an element two implementation methods are common. Either the element stiffness is removed from the global stiffness matrix, or the stiffness of the element is set to a very small value. Stress redistribution is computed after each stage via residual force method. Each analysis represents a step of construction, and these analyses are linked in a parent–child hierarchy. This means every child analysis inherits the stresses, pore pressures, and deformations calculated in its parent stage. Each new child analysis adds or removes material and automatically begins from the mechanical and hydraulic state of the previous one.

A typical staged construction workflow in GeoStudio begins with an initial analysis that establishes the in-situ conditions of the ground. This is often done with a steady-state SEEP/W run to compute pore pressures and a corresponding SIGMA/W gravity analysis to generate the initial stress field. Once the initial state is defined, the first construction stage is created as a child analysis of the initial one. In this new analysis, the first lift of fill material or the first excavation step is activated, and the software solves for the resulting changes in stress and deformation. If the construction process includes waiting periods—such as consolidation between embankment lifts-engineers can insert a transient coupled SIGMA/W–SEEP/W analysis to simulate the dissipation of pore pressures over time.

Managing complex construction sequences is conducted via a hierarchical approach. Each stage is visually represented as a node in the Analysis Tree, making it easy to trace the modeling history or adjust earlier steps. The coupling between SIGMA/W and SEEP/W allows both undrained and time-dependent (drained) responses to be captured accurately. Time control is highly flexible—the user can define the duration of each consolidation step or allow the solver to determine when steady-state conditions are reached. This design makes GeoStudio particularly well suited for embankment construction, soft soil consolidation, or staged excavations where both mechanical and hydraulic effects are significant.

2.3 Material properties of the validation stage

Results from previous tests, such as those by Panahi et al. [50], were used to evaluate the accuracy of the method used for determining the degree of material degradation in each wetting–drying cycle. The materials of tested specimens had been collected from the borrow area of the clay-core materials used in the Shahid Yaghoubi dam [50]. Shahid Yaghoubi dam, a rockfill dam with central clay core, is located 32 km from Torbat-e-Haydarieh city, in Kasalar watershed on the Kasalar river. The arid area and drought period has caused sever fluctuations in reservoir level. The properties of the materials used in the design of the Shahid Yaghoubi dam are presented in Table (1) [50]. Also, the variations after each cycle are presented in Table (2). Figure (2) presents the variations of UCS for different initial saturation ratio (ISR) and after each cycle of wetting and drying.

Table 1. Material properties of clayey compacted specimens of shahid Yghoubi dam [50].

Gs	L.L. (%)	P.I. (%)	w_{opt} (%)	$\gamma_{d,max}$ (kN/m^3)	C (kPa)	ϕ (°)	q $_{ucs}$, (kPa)	k (m/s)
2.69	45.5	22.5	17.3	17.70	100.24	29.96	551.39	10^{-9}

Table 2. UCS of compacted clay specimens at different ISR and after different WDC [50].

WDC \ Sr (%)	UCS (kPa)					
	Dry	20	40	60	80	Saturated
0	537.9	551.1	473.6	408.4	345.9	309.8
1	530.8	542.3	458.6	396.1	330.0	291.3
2	521.2	530.8	450.7	384.6	320.3	280.7
3	500.0	513.2	426.0	360.0	289.5	250.8
4	484.2	496.5	418.1	352.1	286.0	249.0
5	475.4	488.6	419.0	347.7	280.7	242.0
6	469.2	482.4	411.9	341.5	272.80	234.9
7	463.9	476.2	405.8	334.4	267.2	227.9

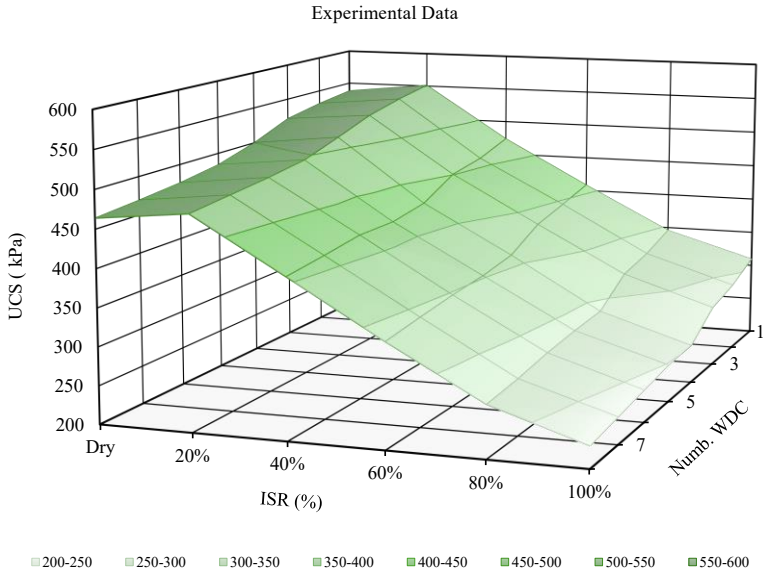


Figure 2. UCS of compacted clay specimens based on ISR and WDC.

2.4 Material properties and geometry of the Karkheh dam

The Karkheh Dam, an earth-fill embankment with a central clay core, is a major embankment dam located in Iran's Khuzestan province. This multi-purpose structure, is constructed using about 30 million cubic meters (Mm³) of different classes of soil and rock, and can store up to 7.8 billion cubic meters of water. The dam is 127 m in height, the crest width is 12 m and its length is about 3000m. The dam crest is situated at an elevation of +234.00 m above mean sea level (MSL), while the minimum foundation level is at +106.00 m MSL. The normal water level is maintained at +220.00 m MSL, and the reservoir has a total storage capacity of approximately 5,572 Mm³ at the maximum water level. The width at the base level is 1100 m. The upstream face has a slope of 1V:2.25H, while the downstream slope is 1V:2.50H. Figure (3) shows the cross section of the dam, its foundation and cut off wall. The dam's foundation is composed of

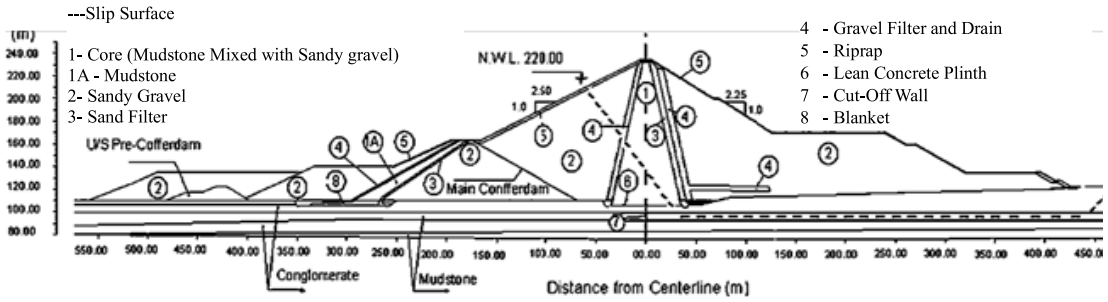


Figure 3. The configuration of the Karkheh dam

interbedded conglomerate and mudstone layers. Geotechnically, the dam site is within the highly active Zagros seismotectonic zone. The dam is underlain by thick alluvial deposits, consisted of gravel, sand and silt and sedimentary marl and limestone rock formations of the Zagros Fold Belt. The thickness of this alluvium varies between 30 to 70 meters. The water tightening measures consisted of a deep cutoff trench excavated beneath the clay core to key into the underlying impermeable marl, complemented by a triple-line grout curtain. This curtain was drilled to depths reaching 70 meters in certain sections. Sand and gravel filters, placed adjacent to the core, with a permeability of typically 10^{-4} to 10^{-5} m/s. The rockfill shells, which provide the embankment's structural stability, consist of quarried rock compacted in approximately 1-meter-thick layers. [51]

According to tectonic studies (MGCE, 1998), the nearest active feature is the Lahbary fault, located approximately 20 km from the dam and extending for 150 km. Also, the recorded available data on the water level of the Karkheh Dam, obtained from the Khuzestan Water and Power Organization, based on the water levels from 2002 to 2020 (1381–1399 in the Iranian calendar) the variations of 3-month average of water table level in the reservoir of the dam were calculated and plotted in Figure (4).

The seismological studies indicated that the peak ground horizontal accelerations of the dam site corresponding to Design Base Level (DBL) is 0.23 g, Maximum Design Earthquake (MDE) is 0.28 g, and the Maximum Credible Earthquake (MCE) is as high as 0.4 g at the top of bedrock**.** The design geotechnical properties of the materials are presented in Table (3). [51]

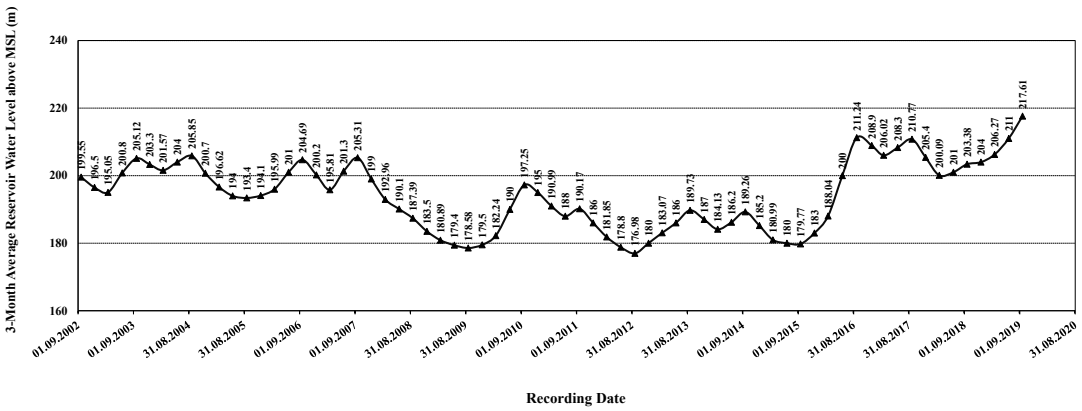


Figure 4. Variations of 3-month average of water table level in the reservoir of the dam

Table 3. Material properties and geometrical parameters used in simulations

Param.	Shell	Core	Filter	Cut off wall	Mudstone layers	Conglomerate layer (1)	Conglomerate layers (2) & (3)
γ_{dry} (kN/m^3)	20	17.4	19	21	19.5	21	21
$\gamma_{sat.}$ (kN/m^3)	22	20.2	20	22	21	23	23
Permeab. (cm/s)	10^{-4}	5×10^{-7}	10^{-3}	1×10^{-7}	5×10^{-8}	4.5×10^{-2}	1.1×10^{-3} (Cong. 2) 6.1×10^{-4}(Cong. 3)
E, (kPa)$\times10^4$	11	3.5	7	400	12	80	100
ν	0.25	0.35	0.27	0.25	0.3	0.25	0.25
C_{uu}, kPa	-	70	-	800	-	-	-
C', kPa	0	30	0	700	70	85	85
ϕ_{uu}, (°)	-	6	-	28	-	-	-
ϕ', (°)	39	20	35	33	22	39.4	39.4
ψ, (°)	10	2	8	10	5	10	10

The finite element discretization of the dam body was established through a systematic mesh convergence study. Multiple meshes with varying element densities were generated to assess their influence on the numerical accuracy and computational efficiency of the simulations. The optimal mesh was selected based on the criterion of achieving sufficient accuracy in the computed responses while minimizing the computational cost. The final discretization adopted for the analysis is presented in Figure (5).

2.4 Method of study

The objective of this study is to analyze the deformation and stability of an earth dam subjected to wetting and drying effects caused by fluctuations in the reservoir water level. The core of the dam, which is constructed from compacted clay soils, typically remains in an unsaturated condition. Therefore, understanding the behavior of these materials under environmental factors such as repeated wetting–drying cycles is essential.

In this study, first the degree of degradation of the compacted clay was determined as a function of the number of WDC based on findings from previous laboratory studies which quantified the changes in soil parameters after various WDC. These degrees of degradation were presented in the form of modification coefficients. In calibration stage the properties of tested specimens were modified by multiplying with modification coefficients and the resulted modified properties were used in numerical simulations. It worth mentioning that the micromechanics of the process is very complicated and includes some sensitive issues. However, this research is intended to check the feasibility of a linear approximation of degradation rate, via a comparison of numerical simulations with observation data. Next, the results of simulations were compared with those of experiments for validation. In sensitivity stage of simulations, the calculations are conducted using each of the main properties, while the other main properties

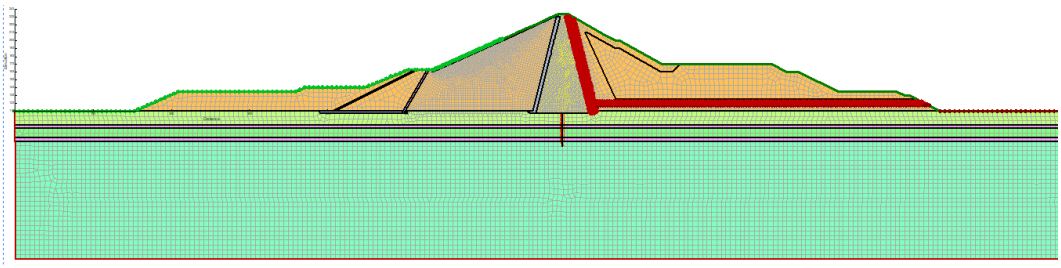


Figure 5. Discretization of the dam body employed in the finite element simulations

are constant. Also, in Karkheh dam simulations, the main design properties of the core of the Karkheh dam, were modified using the modification factors validated in calibration stage and according to the number of cycles each zone of the core experiences. The material properties in these zones were then manually updated in the Staged Construction mode of GeoStudio to reflect these effects accurately.

However, it is important to note that under laboratory conditions, the WDC are performed in a strictly controlled and systematic manner, whereas in large-scale structures such as earth dams, the field conditions are much more complex. In the problem in hand, the changes of water level in reservoir applies load variations, which results in stress changes and deformations. Also, the variations of material properties due to changes in saturation ratio or water content, contribute to changes of deformations, even under constant load. Therefore, at each water level, first the seepage analyses were carried out to identify the zones of the dam core which undergo wetting and subsequent drying due to water-level fluctuations.

3. Results and Discussions

This research is comprised of the following steps: a) numerical simulation of the results of laboratory tests on soil specimens: This step is aimed at calibration and validation of the assumed trend of degradation in material properties, b) sensitivity analyses to show which soil property is more effective, c) numerical analysis of the Karkheh dam: conducted based on the available data of reservoir water level and modified material properties in order to estimate the effect of WDC on the deformations of the dam.

3.1 Calibration simulations

The main objective of this stage of simulations is to validate the method of estimation of the degree of degradation of material properties of the core of a typical embankment dam after each cycle of wetting and drying. This is achieved based on the degree of agreement between experimental and simulation results of the UCS of tested specimens prepared with different ISR and after each cycle of wetting and drying.

Based on the Table (2), the percent of loss of UCS after each cycle of wetting and drying was calculated as presented in Table (4). This percentage was averaged over the specimens with different ISR, as presented in Table (4). Also, according to the tests results provided by Panahi et al. [48], after seven cycles, the cohesion and elastic modulus of specimens decrease by 80% and 11%, respectively. But, the internal friction angle and hydraulic conductivity of the specimens increase by 2.7% and 58%, correspondingly. Combining these figures with Table (4), a set of modification factors were calculated for these parameters, as presented in Table (5).

The simulation steps, including wetting, drying and loading steps, are displayed in Figure (6). Also, the loading step and outputs of computations are depicted in Figure (7).

Table 4. The percent of degradation of compacted clay specimens at different ISR and after different WDC.

	Loss of UCS after WDC, (%)						Average Loss after each WDC for all specimens, (%)
Sr (%) / WDC	Dry	20	40	60	80	Saturated	
0	0	0	0	0	0	0	0
1	9.52	11.76	22.08	16.67	20.22	22.58	17.14
2	13.10	15.29	11.69	15.48	12.36	12.90	13.47
3	28.57	23.53	36.36	33.33	39.33	36.56	32.95
4	21.43	22.35	11.69	10.71	4.49	2.15	12.14
5	11.90	10.59	-1.30	5.95	6.74	8.60	7.08
6	8.33	8.24	10.39	8.33	10.11	8.60	9.00
7	7.14	8.24	9.09	9.52	6.74	8.60	8.22

Table 5. The modified properties of compacted clay specimens used in numerical simulation of each W-D cycle.

WDC	Cohesion, (kPa)	Friction Angle, (^{0})	Permeability (m/s*10^{-7})	Modulus of Elasticity (MPa)
0	100.2	29.96	2.00	30000
1	86.5	30.1	2.20	29332
2	75.7	30.2	2.36	28806
3	49.3	30.5	2.74	27521
4	39.5	30.6	2.88	27048
5	33.9	30.7	2.96	26772
6	26.6	30.8	3.06	26421
7	20.1	30.9	3.16	26100

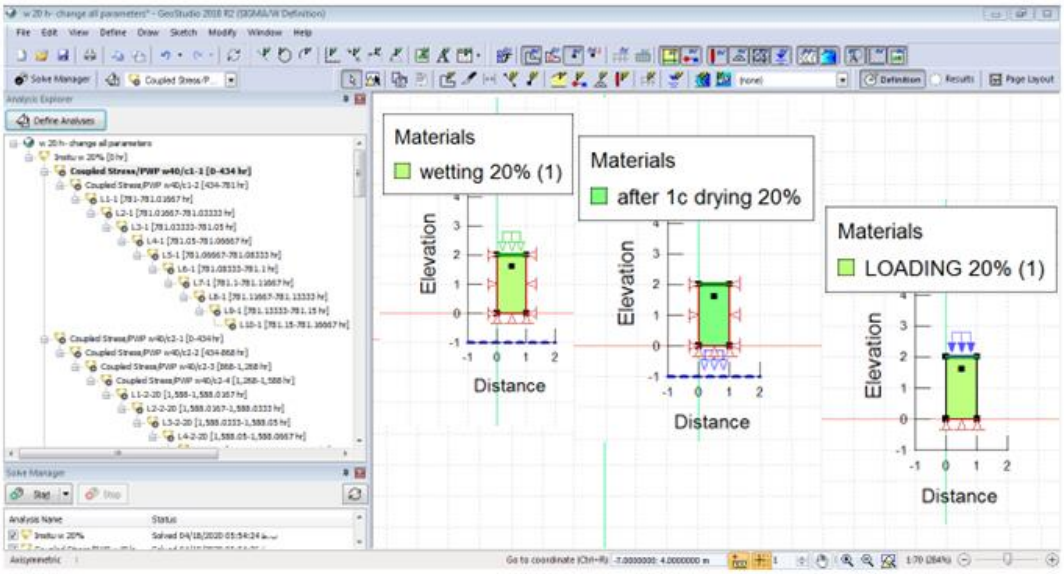


Figure 6. An artificial combined display of the steps of simulation of each test.

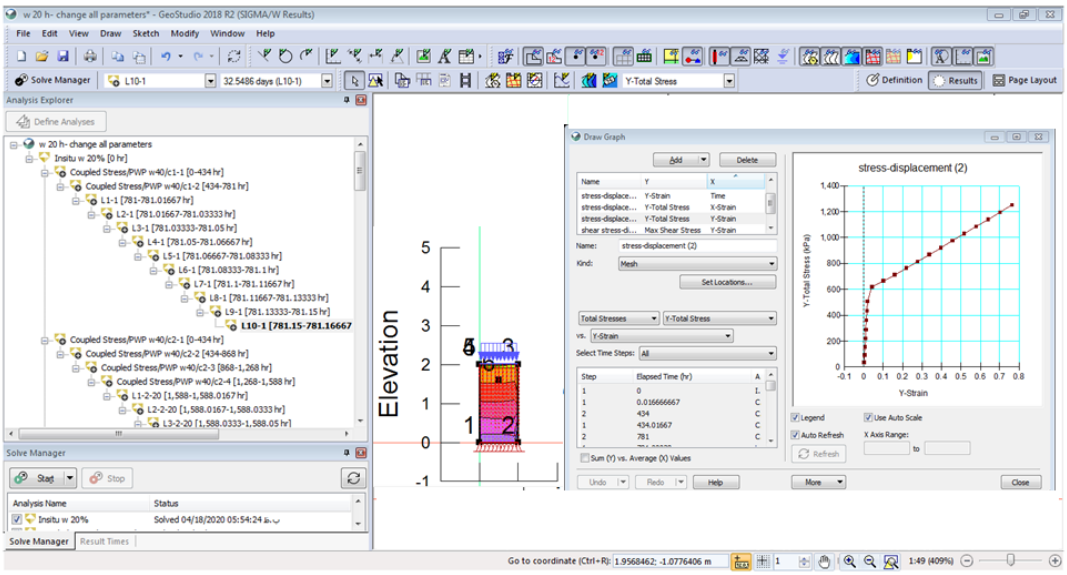


Figure 7. An artificial combined display of the output of software.

After determining the degree of changes of each material property following each number of WDC, numerical simulation of UCS tests was performed, and the method used to apply the effect of WDC was validated. In these simulations, the specimens were numerically subjected to designated WDC, and at the final drying stage, the moisture content was retained at the target level. Then the specimens were subjected to unconfined compression loading in ten steps taking a total of 10 minutes long. The results of simulated tests were compared with the physical test in Figure (8). The results show a maximum difference of about 17% and an average of 10%. The discrepancy between test results and simulation results can be attributed to two main points: a) the errors in selection of suitable values for parameters of main properties, such as friction angle and modulus of elasticity, b) the simulations are based on continuum mechanics, which assumes that the material is stable in high levels of strain such as 15%, which is used as the criterion of failure according to ASTM D2166. While during the experimental tests the specimens may fail physically and reach failure earlier and at lower strains such as 10%. As a result, the test would terminate sooner, and a lower compressive strength would be recorded for the samples compared to the software simulation.

3.2 Sensitivity Analysis

The purpose of this stage was to examine the sensitivity of the UCS of the specimens to the changes in each of the design parameters including cohesion, internal friction angle, hydraulic conductivity, and elastic modulus. Therefore, in this stage, each of the parameters were varied individually, while other parameters where kept constant at their initial value. The simulation process has followed the same procedure as in the validation analysis, and the soil initial parameters pertain to Shahid Yaghoubi dam. However, the degradation pattern for each property was assumed to be the same format as tested in validation stage. The results are presented in Figure (9).

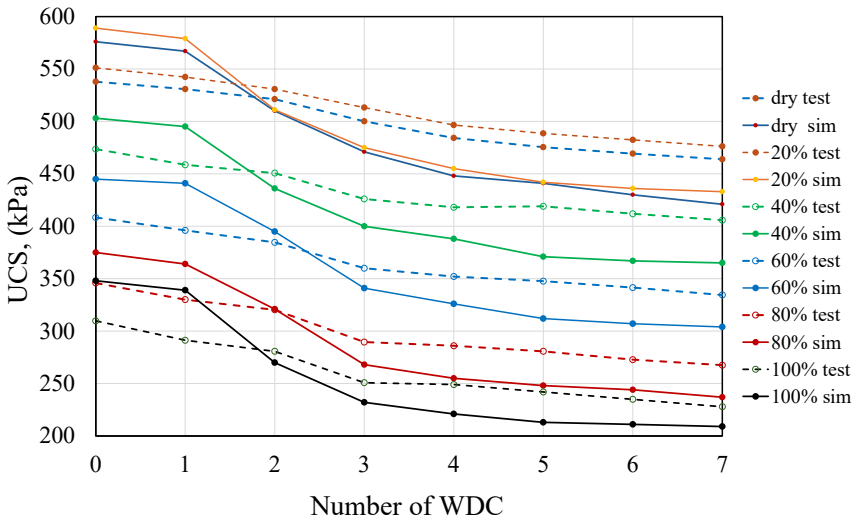


Figure 8. Comparison of the physical and simulated tests results.

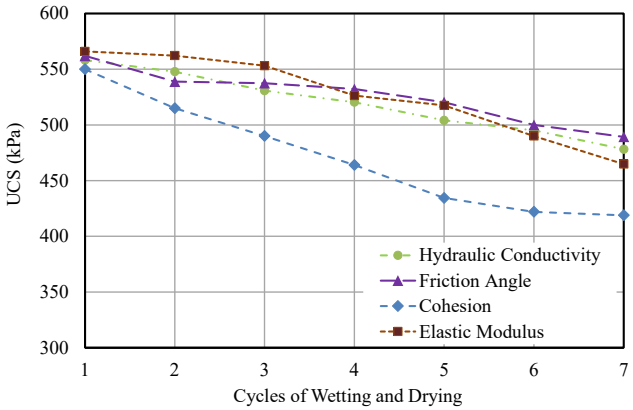


Figure 9. Effect of different material properties on UCS.

Figure (9) shows that during the first to third WDC, the reduction in the elastic modulus has the least effect on decreasing the strength of the samples. In the fourth to seventh cycles, the smallest reduction in strength corresponds to changes applied to the soil's internal friction angle. In general, it can be stated that applying changes to the parameters of elastic modulus, hydraulic conductivity, and internal friction angle results in UCS reductions of similar magnitude. However, changes in soil cohesion have a significantly greater negative effect on UCS, imposing a much larger reduction compared to the other parameters.

3.3 Karkhekh simulations

In order to show the effect of incorporating the degradations of material properties in numerical simulations, as compared to the design material properties, the numerical modeling was conducted in three stages. First, the Karkheh Dam was re-analyzed while incorporating the modifications factors calculated and validated earlier, to the properties of core of the dam in zones subjected to WDC. The objective was to estimate the resulting extra deformations, stress re-distributions. Next, the deformations of dam body during the next seven WDC, considering maximum and minimum permissible reservoir levels, 230.7 m and 178 m respectively, were predicted. In order to present the displacements values, five points along the central axis of the dam and at various elevations from the crest down to levels near the foundation were selected (Figure 10). The coordinates of the selected points are presented in Table (6). Finally, the stability of upstream slope was studied.

Table 6. Coordinates of the selected points

Point	1	2	3	4	6
X-coor.	700.7	700.2	700.7	701.2	702.4
Y-coor.	237	200	178.6	157.4	120

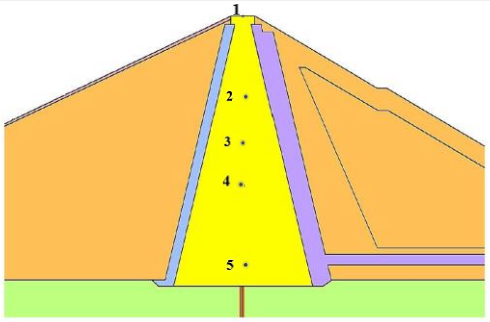


Figure 10. Location of selected points for graphs.

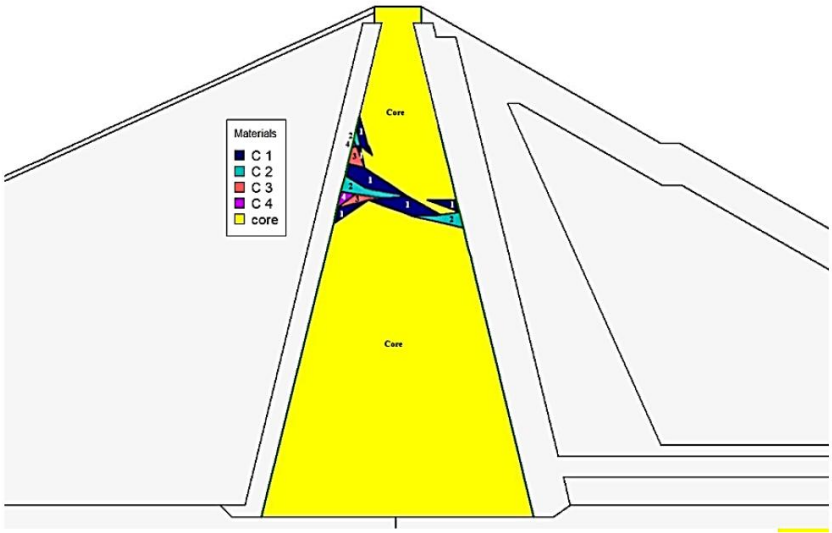


Figure 11. Location of areas which experienced repeated WDC and the number of cycles.

Based on the seepage analysis and considering the water table fluctuations during the period of study (2002 to 2020), some areas of the core of the dam have gone under the wetting-drying cycles. Figure (11) shows the number of WDC each part has undergone. The number is included in the legend of the area. The areas labeled as "core" include areas either stayed above the phreatic line or stayed saturated during the period of study. However, these after each cycle of wetting and drying the properties of the area has first been modified and then the changes were used in calculations of the next step.

3.3.1 Displacements in the period of 2002 to 2020

Vertical displacements

As one of the primary objectives of this research was to investigate the effect of WDC on the degradations in the soil properties of the affected zones and the resulting deformations induced within the dam body, the vertical displacement profiles are first presented. The results obtained from analyses for both cases of incorporating or ignoring the degradations in the core material properties following the WDC, are first presented in Figure (12) for a period of 18 years, from 2002 to 2020.

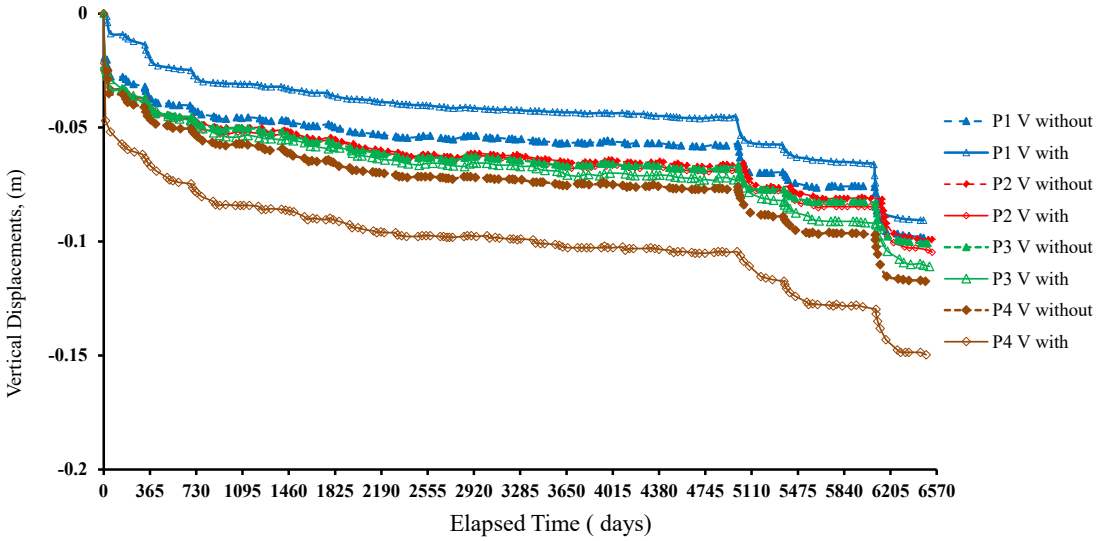


Figure 12. Vertical displacements of selected points under repeated WDC in a period of 18 years, from 2002 to 2020.

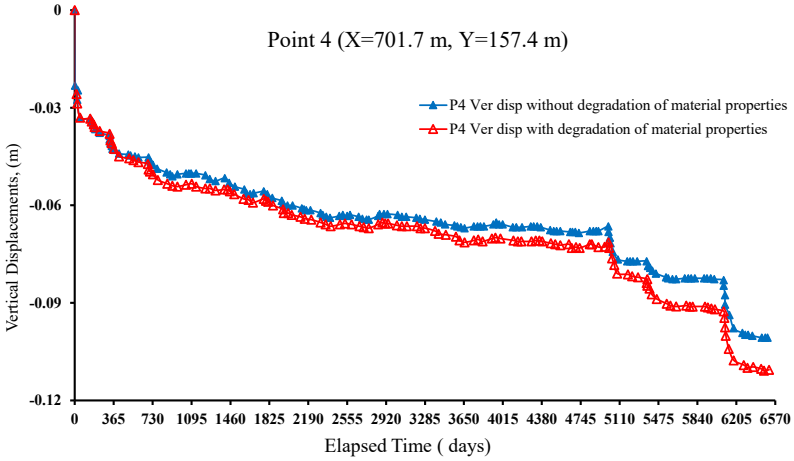


Figure 13. Comparison of calculated vertical displacements at point 4 with and without considering the core material degradation

Figure (12) shows that the horizontal displacements of all points in both conditions, with and without considering degradation of the properties of materials of the dam core after several WDC, have similar patterns and follow the same trend. As shown in Figure (12), the middle points have higher vertical displacements. Therefore, they experience the highest WDC effects. The average difference in vertical settlements between the two cases, including or ignoring the degradation of material properties, is as high as 10%. This shows the importance of the WDC process and its subsequent effects. For instance, the graphs presented in Figure (13) show this effect at the point 4 at the lower height of the dam. Comparing the graphs show a difference of 4 cm in 40 cm which is 10%.

Horizontal displacements

The horizontal deformations were also studied. Figure (14) shows the trend of variations of horizontal displacements along the vertical axis through the center of the dam for the period of 18 years, from 2002 to 2020. As expected, the upper part, including points 1 and 2, move towards upstream. While, lower part, including points 4 and 5 move towards downstream. This shows that at the lower parts the mechanical behaviour is dominant process, while in the upper parts this behaviour diminishes and the degradation effect is dominant. The middle part has the minimum absolute displacements, as it is located between the two parts which have opposite deformations.

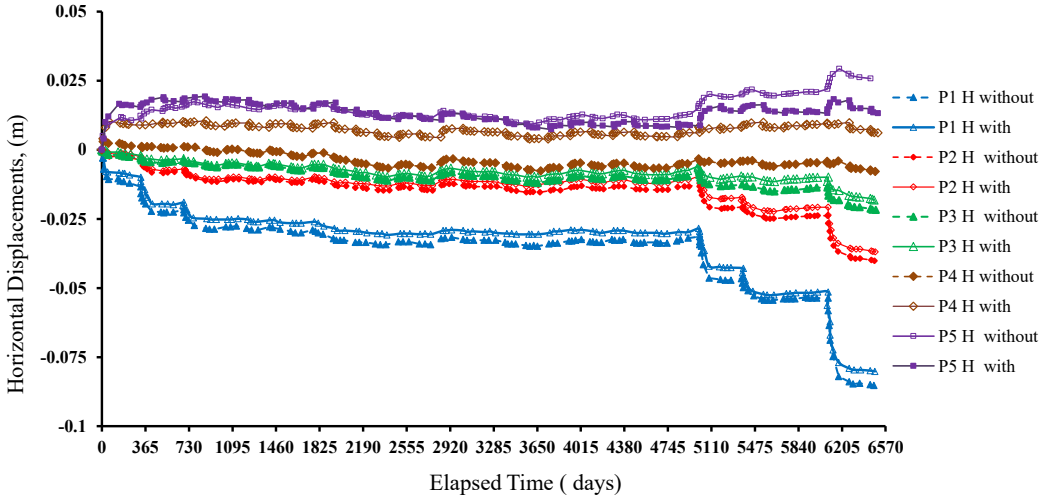


Figure 14. Horizontal displacements of selected points under repeated WDC for a period of 18 years, from 2002 to 2020.

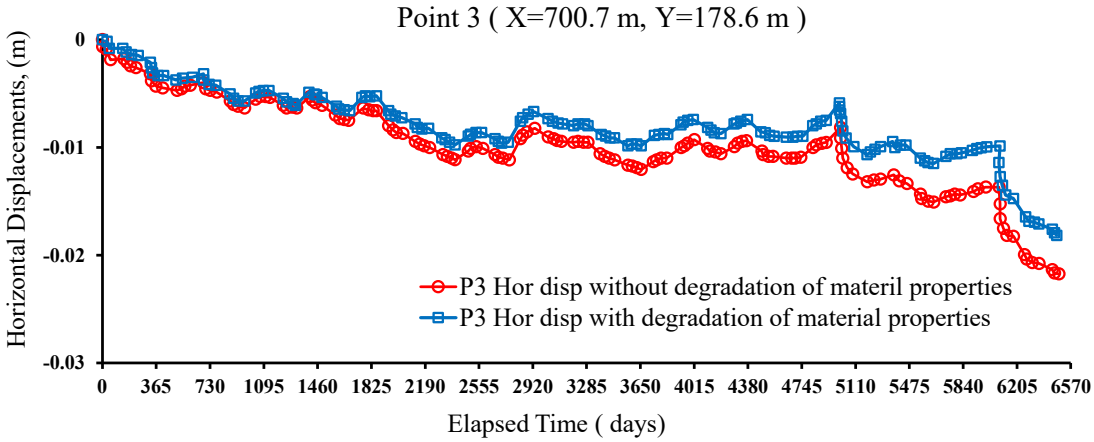


Figure (15). Comparison of calculated horizontal displacements at point 4 with and without considering the core material degradation for the period of 2002 to 2020.

This is due to the complex variations of effective stress, which governs the variations of deformations. The complexity arises from combined effects of variation of seepage pattern and variations of material properties.

The fluctuations in water level causes the small fluctuations in the displacements. This is due to changes in effective stresses due to changes of water level. For clarity, the horizontal displacements of point 3 are shown in Figure (15), seperately.

3.3.2 Prediction of vertical displacement for 2020 to 2027

A series of complementary calculations were conducted for predicting the dam behaviour in the next 7 years, considering the water level variations between the absolute minimum and maximum allowable water levels in the reservoir, 178 m and 230 m, correspondingly. The results are shown in Figure (16). These calculations, also, were conducted based on using either the original material properties or the degraded ones. In order to give a full understanding, the results are combined with the data of previous periods.

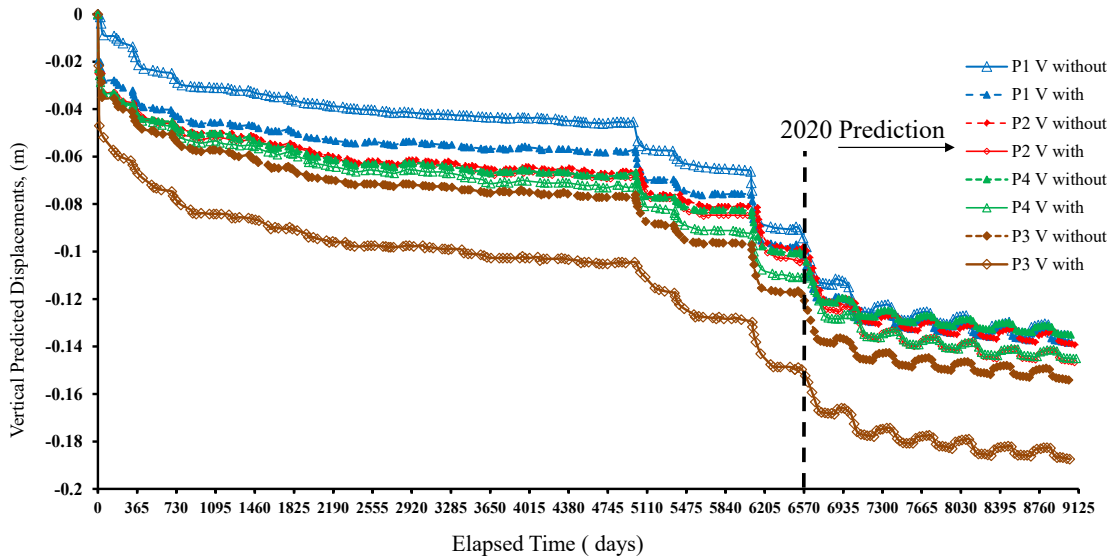


Figure 16. The predicted vertical displacements with and without considering the core material degradation for the period of 2002 to 2027.

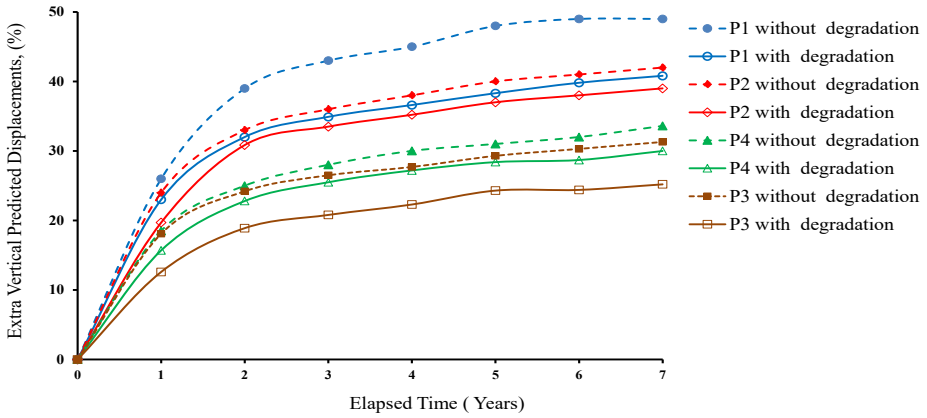


Figure 17. The percentage of increment of predicted vertical displacements with and without considering the core material degradation for the period of 2002 to 2027.

Figure (16) shows that, due to assumed sever changes in water level in the reservoir (62 m fluctuation) for the next 7 years, the vertical displacements at various points show a periodic pattern. Similar to what was described for vertical displacements, the largest displacements occurred during the time that water level was at its highest value since initial impoundment.

As stated earlier, the vertical displacements have increased at a decreasing rate. The percentage changes of the vertical displacements in each prediction step relative to the vertical displacements at the end of last step of simulation phase is presented in Figure (17) at each of the five points along the height of the dam.

4. Conclusions

This study investigated the effects of reservoir water-level fluctuations and associated WDC on the mechanical behavior, deformation patterns, and stability of the Karkheh earth dam, with particular emphasis on the long-term performance of the core material in a semi-arid climatic setting.

Coupled seepage and equilibrium time-dependent numerical analyses were conducted using GeoStudio software, and the material properties were updated manually according to the WDC each region of the dam core experiences.

By integrating laboratory testing with large-scale, and the research provided a comprehensive understanding of how cyclic environmental loading can progressively degrade key geotechnical properties of fine-grained soils within earth-dam structures.

Laboratory and numerical simulations consistently demonstrated that repeated wetting–drying cycles cause a measurable reduction in the compressive strength of the core soil. Although some discrepancies were observed between laboratory UCS values and software predictions, these differences were attributed to early failure of laboratory specimens, especially at high initial saturation ratios and at later WDC, rather than to numerical inaccuracy.

Numerical experiments further revealed that among the strength and hydraulic parameters considered, the loss of cohesion exerted the most significant adverse influence on soil strength, confirming the dominant role of bond degradation, suction reduction, and crack initiation during drying phases and crack expansion upon rewetting.

Analysis of 18 years of reservoir water-level data showed that sections of the mid-elevation core experienced between one and four wetting–drying events during dam operation.

Additional scenarios including water level in reservoir fluctuating between the maximum and minimum permissible levels for the next 7 years, indicated that large portions of the core would be subjected to WDC as a result of these fluctuations. These environmental loadings produced noticeable increases in vertical and horizontal displacements, with mid-

elevation zones exhibiting the greatest sensitivity.

Vertical settlements displayed a gradual, irreversible growth over time, approaching plastic behavior as the number of WDC increased.

Comparisons of scenarios, with and without modification of soil properties, confirmed that incorporating WDC-induced degradation leads to larger predicted deformations, demonstrating the structural implications of strength-parameter deterioration.

These findings highlight that climatic variability in semi-arid regions, through its significant influence on reservoir water levels, poses a significant long-term challenge to the integrity and stability of earth dams. Incorporating these effects into routine monitoring and design protocols is therefore essential for ensuring the sustainable and resilient performance of large earth-dam infrastructures.

However, it worths to remind that this study was performed based on assuming similarity of materials and their degradation rates of the two dams. Also, using the simplified linear model and assuming the worst-case scenario for prediction phase, were the limitations of this study. Resolving these limitations can enhance the conclusions in the next steps of this study.

Author Contributions

M O: Conceptualization, Methodology, Resources, Writing- original draft, Writing-review and editing, Visualization, Supervision, Project administration, Funding acquisition.

S J: Validation, Numerical analysis, Investigation, Resources, Data Curation.

A A: Writing-original draft, Writing-Review and editing, Visualization, Supervision, Funding acquisition.

Declaration of Interest Statement

No conflict of interest exits in the submission of this manuscript, and all of the authors are listed and have approved the enclosed manuscript for publication. On behalf of all authors, I would like to declare that the work described was original research that has neither been published previously, nor under consideration for publication elsewhere, in whole or in part.

Data Availability

The data presented in this study are available on request from the corresponding author.

Fundings

This research has been financially supported by the Ministry of Science, Research and Technology (MSRT) grant no. SCU.C1401.482.

Conflict of Interest

The authors declare that they have no conflict of interest to declare.

Statements and Declarations

All of the authors would like to declare that the work described was original research that has neither been published previously, nor under consideration for publication elsewhere, in whole or in part.

References:

1. Ri YN, Han UC, Jang UJ, Jong DY, Kim CU. Study on stability reduction characteristics of earth and rockfill dams under rapid drawdown using fully coupled seepage-stress analysis. Adv. Civ. Eng. 2022, 7954991. https://doi.org/10.1155/2022/7954991 .
2. Meng Q, Qian K, Zhong L, Gu J, Li Y, Fan K, Yan L. Numerical analysis of slope stability under reservoir water level fluctuations using a FEM-LEM-combined method. Geofluids. 2020;6683311. https://doi.org/10.1155/2020/668331.
3. Zhang J, Liu F, Yang Y, Zi Z, Ding Q, Wang G, Zhang W, Dai X, Liang Y, Liu G. Effects of dry–wet cycles on permeability and shear strength of Yuanmou red clay. Sustainability. 2025;17(19):8900. https://doi.org/10.3390/su17198900 .
4. Talebolelm A, Khodashenas SR, Akhtarpour A. Investigation on effect of wetting and drying cycles on mechanical characteristics of clay materials. Iran J Irrig Drain. 2020; 14(3):1091-1105. (In Persian).
5. Li J, Gao Y, Yang T, Zhang P, Deng W, Liu F. Effect of water on the rock strength and creep behavior of green mudstone. Geomech Geophys Geo-energ Geo-resour. 2023; 9:101. https://doi.org/10.1007/s40948-023-00638-9 .
6. Salehiyan-Dastgerdi M, Hemmat A. Estimation of shear strength parameters of a fine-grained soil under cycles of wetting and drying. In: Proceedings of the 7th National

Congress of Agricultural Machinery Engineering; 2013; Shiraz, Iran. (In Persian).
7. de Costa PA, Mota JCA, Romero RE, Freire AG, Ferreira TO. Changes in soil pore network in response to twenty-three years of irrigation in a tropical semiarid pasture from northeast Brazil. Soil Tillage Res. 2014;137:23-32. https://doi.org/10.1016/j.still.2013.11.004
8. Rogers LE, Wright SG. The effects of wetting and drying on the long-term shear strength parameters for compacted Beaumont clay. Center for Transportation Research, The University of Texas at Austin; 1986.
9. Kholghifard M, Ahmad K, Ali N, Kassim A, Kalatehjari R. Collapse/swell potential of residual laterite soil due to wetting and drying-wetting cycles. Natl Acad Sci Lett. 2014; 37(2):147-153. https://doi.org/10.1007/s40009-013-0221-4.
10. Wang G, Wei X. Modeling swelling–shrinkage behavior of compacted expansive soils during wetting–drying cycles. Can Geotech J. 2014;52(6):783-794 https://doi.org/10.1139/cgj-2014-0059.
11. Kampala A, Horpibulsuk S, Prongmanee N, Chinkulkijniwat A. Influence of wet-dry cycles on compressive strength of calcium carbide residue–fly ash stabilized clay. J Mater Civ Eng. 2013;26(4):633-643. https://doi.org/10.1061/(ASCE)MT.1943-5533.0000853.
12. Goh SG, Rahardjo H, Leong EC. Shear strength of unsaturated soils under multiple drying-wetting cycles. J Geotech Geoenviron Eng. 2013;140(2):06013001. https://10.1061/(ASCE)GT.1943-5606.0001032.
13. Shi A, Yan N, Marschner P. Cumulative respiration in two drying and rewetting cycles depends on the number and distribution of moist days. Geoderma. 2015;243:168-174. https://doi.org/10.1016/j.geoderma.2014.12.019.
14. Naramitkornburee A, Horpibulsuk S, Shen SL, Chinkulkijniwat A, Arulrajah A, Disfani MM. Durability against wetting–drying cycles of sustainable lightweight cellular cemented construction material comprising clay and fly ash wastes. Constr Build Mater. 2015;77:41-49. https://doi.org/10.1016/j.conbuildmat.2014.12.02.
15. Du YJ, Bo YL, Jin F, Liu CY. Durability of reactive magnesia-activated slag-stabilized low plasticity clay subjected to drying–wetting cycle. Eur J Environ Civ Eng. 2016;20(2):215-230. http://dx.doi.org/10.1080/19648189.2015.1030088.
16. Naeini SA, Gholampoor N, NajmosadatyYazdy SA. The effect of wetting-drying cycles and plasticity index on California bearing ratio of lime stabilized clays. J Eng Geol. 2015;9(2):2818. https://doi.org//10.18869/acadpub.jeg.9.2.2817.
17. Wang B, Hu B. Dynamics of aggregate stability under drying and wetting cycles for yellow soil in China. 2016. Agro Environ:10th Int Symp Agriculture Environ.
18. Sayem HM, Kong LW, Yin S. Effect of drying-wetting cycles on saturated shear strength of undisturbed residual soils. Am J Civil Eng. 2016;4(4):143-150. https://doi.org/10.11648/j.ajce.20160404.15.
19. Tang CS, Wang DY, Shi B, Li J. Effect of wetting–drying cycles on profile mechanical behavior of soils with different initial conditions. Catena. 2016;139:105-116. https://dx.doi.org/10.1016/j.catena.2015.12.015.
20. Wang DY, Tang CS, Cui YJ, Shi B, Li J. Effects of wetting–drying cycles on soil strength profile of a silty clay in micro-penetrometer tests. Eng Geol. 2016;206:60-70 https://dx.doi.org/10.1016/j.enggeo.2016.04.005.
21. Akcanca F, Aytekin M. Impact of wetting–drying cycles on the hydraulic conductivity of liners made of lime-stabilized sand–bentonite mixtures for sanitary landfills. Environ Earth Sci. 2014;72(1):59-66. https://doi.org/10.1007/s12665-013-2936-4.
22. Gallage C, Kodikara J, Uchimura T. Laboratory measurement of hydraulic conductivity functions of two unsaturated

sandy soils during drying and wetting processes. Soils Found. 2013;53(3):417-430. https://doi.org/10.1016/j.sandf.2013.04.004.
23. De Camillis M, Di Emidio G, Bezuijen A, Verástegui-Flores RD. Hydraulic conductivity and swelling ability of a polymer modified bentonite subjected to wet–dry cycles in seawater. Geotext Geomembranes. 2016. https://doi.org/10.1016/j.geotexmem.2016.05.007.
24. Rosone M, Ferrari A, Celauro C. On the hydro-mechanical behaviour of a lime-treated embankment during wetting and drying cycles. Geomech Energy Environ. 2018;14:48-60. https://doi.org/10.1016/j.gete.2017.11.001.
25. Liu W, Yang Q, Tang X, Yang G. Effect of drying and wetting on the shear strength of a low-plasticity clay with different initial dry densities. J Test Eval. 2015;44(4). https://doi.org/10.1520/JTE20140096.
26. Luo SL, Huang D, Peng JB, Liu F, Gao XR, Tomas R. Influencing of drying-wetting cycles on mechanical behaviors of silty clay with different initial moisture content. Geomech Eng. 2024;38(3):307-317. https://doi.org/10.12989/gae.2024.38.3.307.
27. Ma C, Li J, Jiao F, Liu Y, Feng H, Wang K, Jiang H, Jiang C, Li Y, Geng X. Physical and mechanical behaviors of compacted soils under hydraulic loading of wetting–drying cycles. Processes. 2023;11(4):1084. https://doi.org/10.3390/pr11041084.
28. Cuisinier O, Masrouri F. Impact of wetting/drying cycles on the hydromechanical behaviour of a treated soil. E3S Web Conf. 2020;195:06008. https://doi.org/10.1051/e3sconf/202019506008 .
29. Sabatino F, Cuisinier O, Russo G, Vitale E, Nicotera MV. Effects of wetting and drying cycles on the mechanical behaviour of lightweight cemented soils. E3S Web Conf. 2023;382:06008. https://doi.org/10.1051/e3sconf/202338206008 .
30. Estabragh AR, Parsaei B, Javadi AA. Laboratory investigation of the effect of cyclic wetting and drying on the behaviour of an expansive soil. Soils Found. 2015;55(2):304-314. https://www.sciencedirect.com/science/article/pii/S003808061500027X
31. Azizi A, Musso G, Jommi C. Effects of repeated hydraulic loads on microstructure and hydraulic behaviour of a compacted clayey silt. Can Geotech J. 2019. https://doi.org/10.1139/cgj-2018-0505 .
32. Dias AS, Hughes PN, Toll DG. Soil–Water Retention Curve Prediction for Compacted London Clay Subjected to Moisture Cycles. Geotechnical and Geological Engineering. 2024;42(4):2799-2814. https://doi.org/10.1007/s10706-023-02706-z.
33. Hafhouf I, Abbeche K. Impact of drying-wetting cycles on shear properties, suction, and collapse of sebkha soils. Heliyon. 2023;9:e13594. https://doi.org/10.1016/j.heliyon.2023.e13594.
34. Walker C, Heitor A, Clarke BG. Impact of drying-wetting cycles on the small strain behaviour of compacted clay. Transp Geotech. 2023;42:101063. https://doi.org/10.1016/j.trgeo.2023.101063 .
35. Oka F, Leroueil S, Tavenas F. A constitutive model for unsaturated compacted clays exhibiting cyclic wetting and drying. Soils Found. 1989;29(3):54. https://doi.org/10.3208/sandf1972.29.3_54.
36. Prasomsri J, Takahashi A. Experimental study on suffusion under multiple seepages and its impact on undrained mechanical responses of gap-graded soil. Soils Found. 2021;61(6):1660-1680. https://doi.org/10.1016/j.sandf.2021.10.003.
37. Deng Z, Wang G, Jin W. Coupling of hydraulic loading and surcharge pressure during suffusion in sandy gravels. Geotechnique Lett. 2023;13(1):75-81. https://doi.org/10.1680/jgele.22.00130.
38. Wang G, Deng ZZ, Yang J, Chen XS, Jin W. A large-scale high-pressure erosion apparatus for studying internal erosion in gravelly soils under horizontal seepage flow. Geotech Test J. 2022;45(6):1037-1053. https://doi.org/10.1520/gtj20220045 .
39. Fu J, Yang Z, Sun Q, Xie Y, Yang J. Experimental and numerical investigation of

seepage erosion in sandy cobbles under coupling hydraulic and dynamic load. Transp Geotech. 2024;49:101429. https://doi.org/10.1016/j.trgeo.2024.101429.
40. Deng Z, Wang G, Wang Z, Jin W. Modelling erosion and stability degradation of a reservoir slope under periodic water level fluctuations. Comput Geotech. 2024;166:106021. https://doi.org/10.1016/j.compgeo.2023.106021.
41. Liu D, Lin T, Gao J, Xue B, Yang J, Chen C, Zhang W, Sun W. Study on the influence of water level on earth dam reinforced by cut-off wall: a case study in Wujing Reservoir. Water. 2023;15:140. https://doi.org/10.3390/w15010140.
42. Jadid R, Montoya BM, Bennett V, Gabr MA. Effect of repeated rise and fall of water level on seepage-induced deformation and related stability analysis of Princeville levee. Eng Geol. 2020;266:105458. https://doi.org/10.1016/j.enggeo.2019.105458.
43. Liao K, Wu Y, Miao F. System reliability analysis of landslides subjected to fluctuation of reservoir water level: a case study in the Three Gorges Reservoir area, China. Bull Eng Geol Environ. 2022;81:225. https://doi.org/10.1007/s10064-021-02452-5.
44. Chen J, Zhu Y, Lv L, Huang H. Influence of morphology of sliding surface on its seepage characteristics and slope stability under fluctuations in reservoir water level. Geotech Geol Eng. 2022;40:3211-3224. https://doi.org/10.1007/s10706-022-02087-9.
45. Yang B, Yin K, Xiao T, Chen L, Du J. Annual variation of landslide stability under the effect of water level fluctuation and rainfall in the Three Gorges Reservoir, China. Environ Earth Sci. 2017;76:564. https://doi.org/10.1007/s12665-017-6929-7.
46. Yang Z, Xi W, Yang Z, Shi Z, Huang G, Guo J, Yang D. Time-lag response of landslide to reservoir water level fluctuations during the storage period: a case study of Baihetan Reservoir. Water. 2023;15:2732. https://doi.org/10.3390/w15152732.
47. Zhang Y, Zhang Z, Xue S, Wang R, Xiao M. Stability analysis of a typical landslide mass in the Three Gorges Reservoir under varying reservoir water levels. Environ Earth Sci. 2020; 79:243-254. https://doi.org/10.1007/s12665-020-08964-3.
48. Haghdoost M, Lakzian E, Norouzi R, Abraham J, Sajjadi SM, Ahadiyan J. Numerical simulation using the finite element method to investigate the effect of internal cutoff walls on seepage and hydraulic gradients in homogeneous earth dams. Model. Earth Syst. Environ. 2023; 9:3851–3864. https://doi.org/10.1007/s40808-023-01755-w.
49. Sadeghi HE, Ahadiyan J. Hydraulically Failure Mechanism of non-Cohesive Homogenous Protective Embankments by Overtopping, Irrigation Sciences and Engineering, 2018;41(1): 115-131. https://doi.org/10.1007/10.22055/jise.2018.13575. (In Persian).
50. Panahi G. The effect of wetting and drying cycles on the physical properties of soil (A case study of Shahid Yaghoubi dam). Ferdowsi University of Mashhad. 2016.
51. Mahab-e-Ghods Consulting Engineers. Karkheh dam Design- Detailed Design Phase Report, Technical Report. 1997. (In Persian)



© 2025 by the authors. Licensee SCU, Ahvaz, Iran. This article is an open access article distributed under the terms and conditions of the Creative Commons Attribution 4.0 International (CC BY 4.0 license) (http://creativecommons.org/licenses/by/4.0/).

Journal of Hydraulic Structures

Volume 12 – Issue 3 – July 2026

Contents:

01 Buckling of elliptical cylindrical shell with variable circumferential thickness under fluid lateral pressure

Davood Poorveis; Amin Khajehdezfuly; Masoud Oulapour; Hakim Tamimi

19 Uncertainty analysis for stability and cracking in a gravity dam using fuzzy set theory (Case study of Pine Flat Dam)

Zahra Ashrafi; Mehdi Komasi; Nazila Kardan

41 Investigation of the Effect of Time-Dependent Viscosity on the Penetration of Cement Grout in Rock Fractures Using a Numerical Modeling Approach

Alireza Sadooghi; Ali Aalianvari; Hamidreza Shahbazian

55 Machine Learning and Statistical Analysis of Measured Velocities by ADV of Free Surface Vortices at Intakes

Hamid Ahani; Saeed Reza Khodashenas; Hamed Sarkardeh

72 Development of an Efficient Multi-Reach Partitioning Approach with Linear Muskingum Method and Weighted Mean of Vectors Algorithm for Inverse Flood Routing

Maziar Rastegarfar; Ali Raeisi Isa-Abadi; Hamed R. Zarif Sanayei

94 Adverse Effects of Repeated Deep Drawdown and Re-impounding Cycles on the Clay Core of Earth Dams; a case study of the Karkheh Dam

Masoud Oulapour; Arash Adib; Sepideh Joulanejad

Shahid Chamran University of Ahvaz